INTERNATIONAL RESEARCH CENTER MAGTOP

DOCTORAL THESIS

Thermoelectric phenomena in topological materials

Supervisor

Dr. hab. Marcin Matusiak

Author

MSc. Md Shahin Alam

A thesis submitted in partial fulfillment of the requirements for the degree of Doctor of Philosophy to

Institute of Physics, Polish Academy of Sciences

Warsaw, June 2024

Dedicated to my paternal and maternal grandparents.

Acknowledgements

First and foremost, I would like to express my deep gratitude to my thesis supervisor, Prof. Dr. hab. Marcin Matusiak, for his invaluable guidance, inspiration, and support throughout this journey. I have been fortunate to work with Dr. hab. Marcin Matusiak on my Ph.D. since 2020. His systematic approach to generating ideas, methodological approach, analyzing data, and writing manuscripts has significantly contributed to my achievements. Moreover, he has supported me in various aspects of my life beyond physics, imparting many life lessons that I will always cherish.

I would also like to express my gratitude to my labmates and collaborators for their invaluable contributions to my research achievements. Special thanks go to my friends for their companionship, support, and encouragement throughout this journey.

Lastly, I am immensely thankful to my parents and family members for their unwavering support, love, and blessings. Without their endless encouragement and support, none of this would have been possible.

We appreciate the support of the Foundation for Polish Science through the international research agendas program co-financed by the European Union within the smart growth operational program.

Author's declaration

I confirm that the work contained in this thesis has not been submitted for consideration for any other academic award and has been completed in accordance with the rules and guidelines of the Institute of Physics, Polish Academy of Sciences. The work is the candidate's own contribution, unless otherwise indicated by a specific reference in the text. Work carried out using or collaborating with others is acknowledged as such. In the dissertation, only the author's viewpoints are given.

License Number : RNP/24/MAY/079651

SIGNED:.........................

DATE: ....

List of publications

The following articles are part of this thesis, where I contributed as the first author highlighted by bold text.

Md Shahin Alam, P.K. Tanwar, Krzysztof Dybko, Ashutosh S. Wadge, Przemysław Iwanowski, Andrzej Wiśniewski, Marcin Matusiak, *Temperature-Driven Spin-Zero Effect in* $TaAs_2$, J. Phys. Chem. Solids **170**, 110939 (2022).

Md Shahin Alam, Amar Fakhredine, Mujeeb Ahmad, P. K. Tanwar, Hung-Yu Yang, Fazel Tafti, Giuseppe Cuono, Rajibul Islam, Bahadur Singh, Artem Lynnyk, Carmine Autieri, and Marcin Matusiak, *Sign change of anomalous Hall effect and anomalous Nernst effect in the Weyl semimetal CeAlSi*, Phys. Rev. B **107**, 85102 (2023).

Md Shahin Alam, Alexandr Kazakov, Mujeeb Ahmad, Rajibul Islam, Fei Xue, Marcin Matusiak, *Quantum transport properties of the topological Dirac Semimetal* α*-Sn*, arXiv:2403.00083 (2024)[Accepted in Phys. Rev. B].

Publications other than thesis

I have also contributed to the following articles.

Pardeep Kumar Tanwar, **Md Shahin Alam**, Mujeeb Ahmad, Dariusz Kaczorowski, and Marcin Matusiak, *Severe violation of the Wiedemann-Franz law in quantum oscillations of NbP*, Phys. Rev. B **106**, L041106 (2022).

Pardeep Kumar Tanwar, Mujeeb Ahmad, **Md Shahin Alam**, Xiaohan Yao, Fazel Tafti, Marcin Matusiak, *Gravitational anomaly in the ferrimagnetic topological Weyl semimetal NdAlSi*, Phys. Rev. B **108**, L161106 (2023).

Achievements

Leonard Sosnowski Prize, Best PhD Student award, 51st International School & Conference on the Physics of Semiconductors, Jaszowiec 2023, Szczyrk, Poland.

One of the 10 most downloaded Physical Review B articles in 2023, Md Shahin Alam* et al, Sign change of anomalous Hall effect and anomalous Nernst effect in the Weyl semimetal CeAlSi, Physical Review B **107**, 085102 (2023).

List of oral and poster presentations

M. S. Alam et al., American Physical Society March Meeting (APS 2023), March 2023, “Anomalous transport properties of Weyl semimetal CeAlSi”, Las Vegas, Nevada, USA. **Poster**

M. S. Alam et al., 51st International School & Conference on the Physics of Semiconductors (Jaszowiec 2023), June 2023, “Anomalous transverse response in topological magnet CeAlSi”, Silesian Beskid Region, Poland, **Oral**

M. S. Alam et al., Joint European Magnetism Symposia Conference (JEMS 2022), July 2022, “Spin zero effect in nonmagnetic centrosymmetric dipnictides $TaAs_2$”, Warsaw, Poland. **Poster**

CERTIFICATE

This is to certify that the thesis entitled “Thermoelectric phenomena in topological materials”, submitted by Md Shahin Alam to Institute of Physics, Polish Academy of Sciences, is a record of bonafide research work under my supervision and guidance, and I consider it worthy of consideration for the award of the degree of Doctor of Philosophy of the Institute.

Supervisor

Dr. hab. Marcin Matusiak,

prof. IF PAN MagTop, Institute of Physics,

Polish Academy of Sciences Warsaw, Poland

ABSTRACT

Three-dimensional topological semimetals are a new class of quantum materials characterized by a non-trivial bulk and surface states. Electronic bands in their structure crosses at gapless points, whose vicinity is populated by unique relativistic-like quasiparticles. As a result, we observe in these materials a kaleidoscope of unusual electronic properties, and among the standard methods of revealing them are measurements of charge transport. These are meaningful and relatively easy to perform but a more in-depth analysis often requires additional experimental evidence. As such, the thermoelectric transport measurements provide an exceptional tool to probe the electronic properties of topological semimetals with high sensitivity indicated by the Mott - Jones relation. In this thesis I have focused on the three types of quantum effects observed in transport phenomena. Specifically, these are quantum oscillations (QOs), the anomalous Hall effect (AHE), the anomalous Nernst effect (ANE) and the chiral anomaly.

The key characteristics of fermions in topological semimetals can be studied by quantum oscillation measurements. Here, we present a detailed analysis of QOs in $TaAs_2$, where we observed an unusual temperature (T) evolution of the fundamental frequency β and its second harmonic 2β amplitudes. Namely, in the oscillatory Nernst signal the former disappears completely at $T \approx 25$ K, while 2β frequency is still present. We attribute this behavior to a temperature-induced spin-zero effect derived from the temperature evolution of the Landé g-factor. Subsequently, the T - dependence of the g-factor may reflect evolution of the spin-orbit coupling, which in the case of $TaAs_2$ can go hand in hand with a change a topology of the electronic system.

One important feature of Weyl fermions is the accompanying Berry curvature (BC), which acts like an effective magnetic field leading to the appearance of intrinsic AHE and ANE. In the ferromagnetic phase of Weyl semimetal CeAlSi, we detected a sign change in the anomalous Hall conductivity (AHC) from positive to negative, when the magnetic field (B) was rotated from the hard to easy axis. This sign reversal in AHC was attributed to the reconstruction of the electronic structure and a change in associated BC driven by spin reorientations. Additionally, the anomalous Nernst conductivity (ANC) was detected when B was oriented along the hard axis. Significant AHC and ANC persisted in the paramagnetic

phase of CeAlSi, and their temperature dependence can be described by the presence of the Weyl points near the Fermi level.

The evidence for the chiral anomaly in the Weyl system based solely on charge transport measurements, i.e. observation of the negative longitudinal magnetoresistance (NLMR), has sometimes been questioned due to the possible contribution of the current jetting effect. Here, we demonstrate that the pumping of chiral fermions between Weyl cones can be observed in the topological Dirac semimetal α-Sn using combined electrical and thermoelectric transport studies. The latter is expected to be robust to external artefacts. The experimental evidence of the chiral anomaly were detected in both measurements – NLMR and negative slope of the thermopower were observed at low temperatures when the magnetic field was parallel to the applied electric field (E) or the thermal gradient (∇T). Furthermore, the angular variation of resistivity and thermopower confirmed the rapid diminishing of anomalous chiral current when magnetic field was tilted away from the applied E or ∇T. We also showed that at high temperature the intervalley Weyl scattering time decreases, and as a consequence α-Sn in this range is no longer in the chiral limit.

STRESZCZENIE

Trójwymiarowe semimetale topologiczne stanowią nową klasę materiałów kwantowych charakteryzujących się obecnością nietrywialnych stanów objętościowych i powierzchniowych. W strukturze elektronowej tych związków dochodzi do przecinania się pasm w bezprzerwowych punktach, których sąsiedztwo jest obsadzone relatywistycznymi kwazicząstkami. W rezultacie obserwujemy w takich materiałach kalejdoskop niezwykłych właściwości elektronowych, zwykle badanych za pomocą pomiarów transportu ładunkowego. Otrzymane w ten sposób dane niezaprzeczalnie niosą wiele informacji i są stosunkowo łatwe do otrzymania, jednak dogłębniejsza analiza często wymaga dodatkowej eksperymentalnej ewidencji. Takową oferują badania transportu termoelektrycznego, które, jak sugeruje formuła Motta – Jonesa, są wysoce czułym narzędziem do badania właściwości elektronowych semimetali topologicznych. W niniejszej rozprawie skupiłem się na trzech rodzajach efektów kwantowych obserwowanych w zjawiskach transportowych. Są to mianowicie oscylacje kwantowe (QO), anomalny efekt Halla (AHE) i anomalny efekt Nernsta (ANE) oraz anomalia chiralna.

Podstawowe właściwości fermionów w semimetalch topologicznych można badać za pomocą pomiarów oscylacji kwantowych. W pracy przedstawiono szczegółową analizę QO w $TaAs_2$, gdzie zaobserwowaliśmy nietypową ewolucję temperaturową (T) amplitud częstotliwości fundamentalnej β i jej drugiej harmonicznej 2β. Otóż w oscylacyjnym sygnale Nernsta pierwsza z nich zanika całkowicie przy $T \approx 25$ K, podczas gdy częstotliwość 2β jest nadal obserwowana. Przypisujemy to zachowanie efektowi spin - zero indukowanemu zmianą temperatury, a będącemu skutkiem ewolucji czynnika Landégo (g). Ta z kolei może odzwierciedlać zmiany sprzężenia spin - orbita, co w przypadku $TaAs_2$ powinno wiązać się z przedefiniowaniem topologii układu elektronowego.

Ważną cechą fermionów Weyla jest towarzysząca im niezerowa krzywizna Berry'ego (BC), która działa jak efektywne pole magnetyczne prowadząc do pojawienia się niezwiązanych z rozproszeniami AHE i ANE. W fazie ferromagnetycznej semimetalu Weyla CeAlSi wykryliśmy zmianę znaku anomalnego przewodnictwa Halla (AHC) z dodatniego na ujemny, zachodzącą na skutek zmiany orientacji pola magnetycznego (B) z trudnej do łatwej osi magnetyzacji. Zmiana znaku AHC została powiązana z rekonstrukcją struktury elektronowej (i wynikającej z niej BC), która jest konsekwencją reorientacji spinów. Gdy B

było skierowane wzdłuż trudnej osi, stwierdzono także pojawianie się anomalnego przewodnictwo Nernsta (ANC). Co istotne AHC i ANC pozostały mierzalne również w fazie paramagnetycznej CeAlSi, a ich zależności temperaturowe można zamodelować zakładając obecność punktów Weyla w pobliżu poziomu Fermiego.

Ewidencja wskazująca na pojawianie się anomalii chiralnej w układzie Weyla oparta wyłącznie na pomiarach transportu ładunkowego, tj. obserwacji ujemnego magnetooporu podłużnego (NLMR), była czasami kwestionowana ze względu na możliwy wkład od tzw. efektu current – jetting. W naszej pracy pokazujemy, że pompowanie chiralnych fermionów między stożkami Weyla w topologicznym semimetalu Diraca α-Sn można zaobserwować przy użyciu połączonych badań transportu elektrycznego i termoelektrycznego. Oczekuje się przy tym, że te ostatnie powinny być odporne na artefakty eksperymentalne. Wyniki wskazujące na pojawianie się anomalii chiralnej zostały wykryte w obu pomiarach. W niskich temperaturach oraz gdy pole magnetyczne było równoległe do przyłożonego pola elektrycznego (E) albo gradientu temperatury (∇T) zaobserwowano NLMR albo ujemne nachylenie polowej zależności siły termoelektrycznej. Co więcej, kątowe zależności oporności elektrycznej i siły termoelektrycznej potwierdzają szybką degradację anomalnego prądu chiralnego, gdy pole magnetyczne było oddalane od kierunku przyłożonego E albo ∇T. Wykazaliśmy również, że w wysokiej temperaturze międzydolinowy czas rozpraszania maleje, a w konsekwencji α-Sn w tym zakresie nie znajduje się już w granicy chiralnej.

Contents

List of Figures

CHAPTER 1

INTRODUCTION

Prior to 1980, the phase transitions of materials were understood according to Landau's formalism, in which the system goes from a highly symmetric phase to a lower or broken symmetric phase [1,2]. Changes of symmetry can be described by an order parameter, which is finite for the ordered phase and vanishes in the highly symmetric phases. In the 1980s, the discovery of quantum Hall effect in 2D electron gasses led to introduction of exotic topological phases, which do not involve breaking of symmetries [3,4]. These quantum phases can be classified with a topological invariant, namely Thouless-Kohmoto-Nightingale-Nijs number (TKNN), or the Chern number (C) [3]. This topological invariant can be understood in terms Berry phase, in which a system acquired an additional phase associated with the Bloch wave functions during the cyclic adiabatic transformation [5]. Over the past sixteen years, the theoretical prediction of topological phases induced by spin-orbit interaction has been realized in real crystalline materials [6,7]. Initially gapped topological phases, also known as topological insulators (TIs) have been reported, those were protected by time reversal symmetry [8]. Subsequently, a topological crystalline insulator (TCI) phase protected by crystalline symmetry was experimentally discovered [9].

In the last decade, topological semimetals (TSMs) distinct from TIs, have attracted considerable attention due to the bulk band crossings resulting in non-trivial electronic structures [10–13]. In these materials, the valence band and the conduction band intersect at or near the Fermi level (E_F) to form isolated points or lines [11]. Such gapless band contact points were predicted very early on, but their importance due to their topological nature has only recently been realized [14]. They give rise to gapless electronic excitations associated with the topological invariant [15,16].

This chapter is structured as follows. First, I will provide a detailed overview of Dirac and Weyl semimetals. Then, I will discuss the various transport phenomena observed in topological Dirac and Weyl semimetals. Following this, I will briefly discuss the thermoelectric response in topological materials. Finally, I will present the motivation and objectives of this work.

1.1 Topological semimetals

In the past few years, the presence of low-energy fermionic excitation in TSMs has brought them to the forefront of condensed matter research [11,12]. TSMs are divided into three categories based on the dimensionality of the band crossing at or near the Fermi level in the momentum space [17]. The first group exhibit zero-dimensional (0D) band crossing, forming two or four degenerate band crossings around the E_F. Dirac and Weyl semimetals are the famous materials showing 0D band crossing. On the other hand, nodal-line semimetals belong to the second group, in which band crossing occurs along the one-dimensional (1D) line in the momentum space. In recent times, two-dimensional (2D) band crossing has been proposed in nodal-surface semimetals [18].

1.1.1 Dirac semimetals

The low energy excitations of free or nearly free quasiparticles in solids can describe by the Schrödinger equation. However, non-relativistic Schrödinger equation has certain limitations, for instance recently discovered fermionic excitations in TSMs need to be described by Dirac and Weyl equations [19]. The Dirac Hamiltonian of an electronic system can be written as [19]:

$$H_D = v_F\alpha.\boldsymbol{k} + \beta m v_F^2 = \begin{bmatrix} v_F\sigma.\boldsymbol{k} & m v_F^2 \\ -m v_F^2 & -v_F\sigma.\boldsymbol{k} \end{bmatrix} \tag{1.1}$$

Where k, σ, m and v_F are the momentum, Pauli spin, effective mass and Fermi velocity respectively. Since Eqn. 1.1 describing the Dirac fermions inside solids is analogous to high energy Dirac Hamiltonian (where v_F was replaced by the speed of light c), it follows an analogous energy – momentum relation: $E_{\pm} = \pm\sqrt{m v_F^4 + k^2 v_F^2}$. This relation immediately gives for a massive quasiparticle an energy gap $\Delta E = 2 m v_F^2$ at k = 0 (see schematic of Fig. 1.1a). Alternatively, for m = 0 we have a gapless degenerate point as shown in Fig 1.1b, which is known as the Dirac point. Materials having such points are called Dirac semimetals, and their low-energy excitations are identified as massless Dirac fermions [12]. In a sense 3D topological Dirac semimetals are counterpart of 2D graphene [6], but the Dirac states in DSMs differ from the gapless states of graphene. In the latter, the application of spin-orbit coupling (SOC) lifts the degeneracy to make it a quantum spin Hall insulator [6]. On the other hand, Dirac semimetals exhibit symmetry-protected degenerate Dirac nodes in the presence of SOC.

There were initial attempts to achieve DSMs state by fine tuning SOC in a topological insulator by modifying chemical composition [20], by applying strain [21]. However, it was later reported that there are other mechanisms leading to the realization of stable Dirac junctions in DSMs [12]. This can be achieved by (i) band inversion mechanism; (ii) symmetry enforced mechanism (iii) combination of band inversion and uniaxial rotational symmetry. These mechanisms are associated with a broad range of variations in the system's Hamiltonian parameters.

(i) In this mechanism, the degenerate Dirac point can be achieved by the presence inversion symmetry along with the fine tuning of chemical composition and strain. This type of Dirac point was observed during the phase transition between trivial insulators to the nontrivial topological insulator. Dirac semimetals induced by the band inversion mechanism were reported in $Pb_{1-x}Sn_xTe$ [9] and $(Bi_{1-x}In_x)_2Se_3$ [22]. On the other hand Dirac points in $ZrTe_5$ occurred naturally by topological phase transition without even change in chemical composition [23].

(ii) Here we have fourfold degenerate Dirac points appearing at high symmetric point of Brillouin zone. The necessary condition is the particular space group of a materials in the presence of nonsymmorphic symmetry, which means glide reflections along with screw rotations [24]. Due to such strong requirements, these kinds of Dirac electronic structure are theoretically predicted to be realized in β-BiO_2 [24] and distorted spinels [25]. These are still awaiting experimental confirmation.

(iii) In this scenario, the tuning of physical parameters, such the chemical composition or strain, etc., ensures that bands of different eigenvalues interact and create Dirac points on the opposite sites of the time-reversal invariant moment (see Fig.1.1c). The presence of uniaxial rotational symmetry preserves the Dirac points under weak perturbations, or in other words, such type of Dirac points are topologically protected. Experimental evidence of topologically protected Dirac semimetals are reported in Cd_2As_3 [26], Na_3Bi [27], α-Sn [28].

In this dissertation, out of three semimetals one of them is α-Sn, in which compressive in-plane strain leads to formation of pair of four fold degenerate Dirac points along out-of-plane wave vector [28]. We report in Ref. [29], in the presence of spin-orbit coupling, two Dirac points ($\pm k_z$) as shown in Fig. 1.1, along the highly symmetric $\Gamma \rightarrow Z$ direction, protected by four fold rotational symmetry along the z-axis.

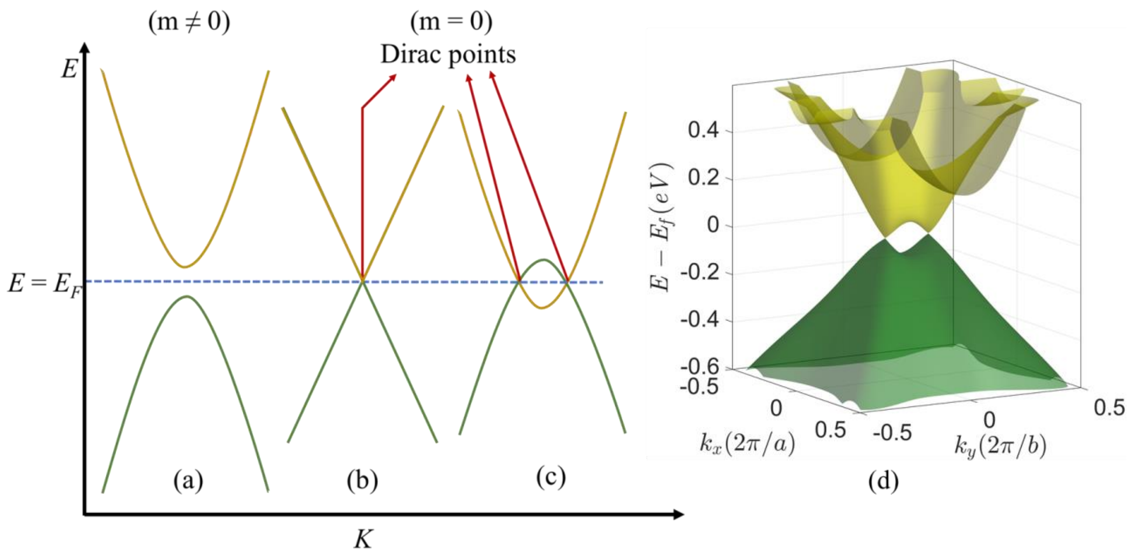

Figure 1.1. Schematic representation of electronic structure; (a) trivial insulator; (b Dirac semimetal; (c) Band inversion mechanism formed pair of Dirac points protected by uniaxial rotational symmetry. (d) Pair of Dirac points of α-Sn at $\pm k_z$ protected by four fold rotational symmetry (C_{4z}) along z axis.

1.1.2 Weyl semimetals

Let's start again with the Dirac Hamiltonian, when m = 0, equation 1.1 can be rewritten as [30]:

$$H_{\pm} = \pm v_F \sigma . \boldsymbol{k} \tag{1.2}$$

This is general form of Weyl Hamiltonian analogous to the massless relativistic Hamiltonian suggested by Hermann Weyl in 1929 [31]. Eqn. 1.2 described a pair of band touching points in the electronic structure with an energy eigen values of $E(k){=}{=}\pm v_F|k|$. In the last two decades, these band touching points have been studied in topological materials and denoted as Weyl points [12]. If they occur at or near the Fermi level the corresponding low energy excitations of these band intersection points are at or near the E_F known as Weyl fermions [12]. Those materials that exhibit this unique property is are called Weyl semimetals.

The Weyl points are distinct from Dirac points, the latter composed of two copies of Weyl points. Weyl points in the electronic structure has stable non-trivial topology described by a nonzero Chern number. The value of C associated with Fermi surface enclosing the Weyl point in the k-space can be expressed as [30]:

$$C = \frac{1}{2\pi} \oiint \Omega\,(\boldsymbol{k}) \cdot ds \tag{1.3}$$

here, Ω(k) is the Berry Curvature. For a 3D Weyl point, the Berry curvature adopts the universal form [30]:

$$\Omega_{\pm}(\boldsymbol{k}) = \pm \frac{\hat{e}_k}{2k^2} \tag{1.4}$$

where, $\hat{e}_k$ is the unit normal vector. These result in the Chern number (also known as the chiral or topological charge of Weyl points) being equal to C= ±1. The chiral charge measures the Berry flux in a singular Weyl points, analogously to the electric flux in Gauss's law of classical electrodynamics. Thus, the sign of C indicates whether the Weyl point in the k space acts as a source (C= +1) or a sink (C= –1) of Berry curvature. Since the net chiral charge over the Brillouin zone should be zero, these Weyl points always appear in pairs. The essential condition required to generate a pair of two-fold degenerate Weyl points from a fourfold degenerate Dirac point is breaking of either time reversal symmetry (TRS) or inversion symmetry (SI), as it is discussed below shown schematically in Figure 1.2a. Figure 1.2b shows schematically that the surface projection of the Weyl points are connected with a unclosed contour staring from one Weyl point and terminates at other Weyl point of opposite chirality or Chern number. This unclosed line connecting two Weyl pints is called the Fermi arc [32] and it is clearly distinct from the Fermi surface forming a close loop. Thus, detection of the Fermi arc, which can be done via a surface sensitive angle-resolved photoemission spectroscopy (ARPES) technique, provides compelling evidence for a Weyl-type electronic structure.

As mentioned, there are two ways to realize WSMs, (i) by breaking time reversal symmetry, or (ii) by breaking inversion symmetry:

(i) Time reversal breaking WSMs

Weyl points induced by breaking of TRS were first postulated in pyrochlore iridates $R_2Ir_2O_7$ (where R is a rare-earth element) [10]. The magnetic order in this compound was found to be due to the all-in/all-out configuration of the Ir (R) sites, leading to a break in the time-reversal symmetry, while the inversion symmetry is preserved. It was theoretically predicted that onsite coulomb interaction can modify the electronic ground state giving rise to the possibility of the Weyl semimetal phase to occur. Following this work, it was postulated that the Weyl phase should form in a magnetic doped superlattice structure composed of magnetic layers and topological insulator [33]. Subsequently, the search for a 3D Weyl semimetal phase in topological insulators began by incorporating magnetic impurities, for instance in HgTe, which was a well-known topological insulator. The doping of this material with Cd atoms can modify the band gap to achieve the critical band touching point, while doping of Mn can break the time reversal symmetry creating 3D Weyl phase in $Hg_{1-x-y}Cd_xMn_yTe$ [34]. Later, there were shown several examples of ferromagnetic semimetals and non-collinear antiferromagnets hosting the novel Weyl phase by breaking the TRS, such as $Co_3Sn_2S_2$ [35], Co_2MnAl [36], Mn_3Sn and Mn_3Ge [36,37] etc. Furthermore, magnetotransport studies have also suggested the existence of Wey points in the Dirac semimetals Cd_2As_3 [38], Na_3Bi [39] and α-Sn [28] in the presence of a magnetic field.

(ii) Inversion breaking WSMs

Initially, researchers were looking for the appearance of Weyl points in a tunable topological insulator $BiTl(S_{1-x}Te_x)_2$ [40] in which alternating layers can enable inversion symmetry breaking. Topological insulator based superlattice structure can also break the inversion symmetry, transforming the system to a Weyl semimetal during a topological phase transition [41]. However, these systems have not received significant attention due to the substantial experimental challenges in observing Weyl points, which can disappear with slight variation of real physical parameters such as chemical compositions. On the other hand, materials with internally broken inversion symmetry become frontal because the Weyl points in these materials are well separated and appear near the Fermi level. The compelling evidence of Fermi arc and bulk Weyl fermions was reported in TaAs, and the material was recognized as the first stoichiometric Weyl semimetal [42]. Subsequently, the Weyl fermions were also reported in systems with broken inversion symmetry, such as NbP [43], NbAs [44], TaP [45] etc. Recently, it has been demonstrated theoretically as well as experimentally that RAlPn series (Pn = Ge, Si), in which both inversion and time reversal symmetry are broken, host the Weyl nodes [46].

In addition to the type of symmetry breaking, Weyl semimetals can be divided into two groups due to the dependence of their energy dispersion near Weyl points. The electronic system of type-I WSMs obey Lorentz symmetry and contains untitled Weyl cones in which point like Fermi surface ideally only crosses through Weyl points. The type-II does not follow Lorentz symmetry and exhibits strong tilting of Weyl cones. Their Weyl points touches the electron and hole pockets on the Fermi surface [11].

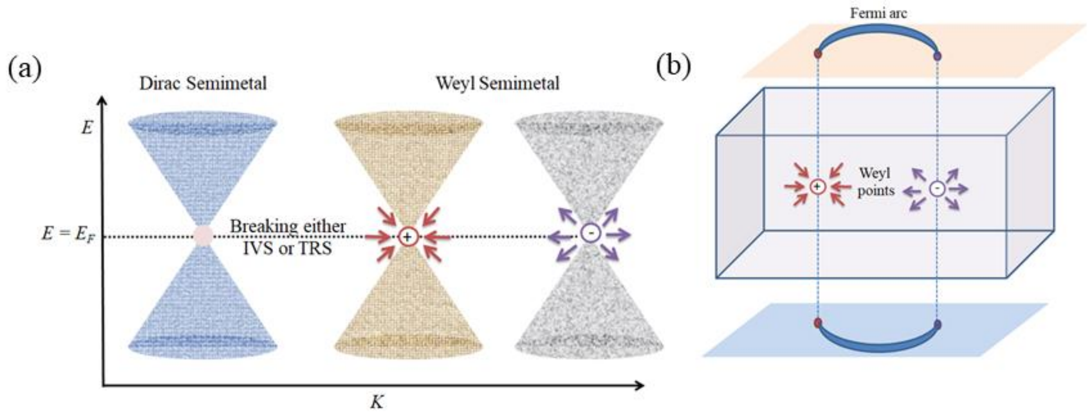

Figure 1.2. Schematic representation: (a) A four-fold Dirac point can split into pairs of two-fold Weyl points with opposite chirality when at least one symmetry, such as time reversal or inversion symmetry, is broken. (b) The surface projection of a pair of Weyl points connected through a Fermi arc.

1.2 Transport phenomena

Topological semimetals exhibit many intriguing qualities in electronic magnetotransport properties. The linear band crossings near or at the E_F of these materials give rise to remarkable transport features, including non-saturating in high magnetic field magnetoresistance and magneto-thermopower [47,48]. If the Fermi level lies close to Dirac or Weyl nodes, then small effective mass Dirac or Weyl fermions, together with their high mobility, leads to pronounced quantum oscillations. These significantly affect various transport phenomena, including electric conductivity, where they are referred to as the Shubnikov–de Haas (SdH) effect [49]. A finite Berry curvature associated with Weyl nodes can manifest itself as a phase-shift of QOs [50] and also lead also to emergence of intriguing physical phenomena, such as the intrinsic anomalous Hall effect [51] and anomalous Nernst effect [52]. Still another magnetotransport phenomenon specific to Weyl semimetals occurs when an electric field or thermal gradient is applied parallel to the magnetic field. This can the principle of chiral charge conservation between Weyl points of opposite chirality, leading to the appearance of an interesting phenomenon called chiral anomaly [53].

1.2.1 Quantum oscillations

The study of quantum oscillations is a powerful tool for investigating the electron structure of topological semimetals. This can provide information on the Fermi surface area, effective mass, mobility, Landé g-factor and Berry phase. The theoretical description of quantum oscillations was developed by L.D. Landau, who noted that electronic states of charge carriers become quantized under the influence of a magnetic field. This causes the energy bands to split into Landau levels (LLs), and as they expand with increasing magnetic field, the density of states (DOS) at E_F becomes modulated to the rhythm of LLs crossing the Fermi energy. The periodic modulations of DOS at E_F results in the appearance of quantum oscillations in physical quantities such as magnetization, resistivity, Hall resistivity, thermoelectric power, and Nernst effect etc.

Landau level quantization of 3D relativistic fermions is different from non-relativistic electrons. The latter has a parabolic energy dispersion relationship, while for the former it is linear. The energy eigenvalues for 3D non-relativistic electrons, when the magnetic field applied along z-axis can be written as,

$$\varepsilon_{n,k} = \frac{\hbar eB}{m^*}\left(n + \frac{1}{2}\right) + \frac{\hbar^2 k_z^2}{2m^*} \quad (n = 0,1,2,3,\dots) \tag{1.5}$$

where n represent the Landau levels number, ħ is reduced Planck constant and e, m^*, k_z is the charge, effective mass and wavevector of the electrons, respectively. Notably, the energy is not quantized along the motion of electrons. Whereas the energy eigenvalues for 3D relativistic fermions can be read as [54],

$$\varepsilon_{n,k} = v_F \, sgn(n)\sqrt{2e\hbar|B||n| + \hbar^2 k_z^2} \quad (n = 0,1,2,3,\dots) \tag{1.6}$$

where v_F is the Fermi velocity of relativistic fermions, $sgn(n)$ is the sign function. Analogous to the non-relativistic case, energy along relativistic fermion motion is unquantized. Landau levels for relativistic fermions are shown in Fig. 1.3. The formation of Landau tubes illustrated in Fig. 1.3b involves 3D free electrons under a magnetic field along the z-axis. Once magnetic field was applied, overlaps between LLs at energy space leading to form a mixture of Landau tubes. Consequently, an equal energy surface intersects multiple Landau cylinders, which radius is field dependent i.e. $\propto \sqrt{B}$. Aforementioned quantum oscillations occur when the Landau tube crossing the Fermi surface representing the extremal cross sectional area (S_{ex}). Thus, one can find the S_{ex} from the frequency (F) of QOs using Onsager relation, $F = \frac{2\pi e}{\hbar} S_{ex}$ [49]. The oscillations in physical quantities can be described by the Lifshitz–Kosevich theory [49]. The oscillatory signal of Gibbs thermodynamic potential ($\widetilde{\Omega}$) at zero temperature can be written as [49],

$$\widetilde{\Omega} \propto B^{\frac{5}{2}} \sum_{p=1}^{\infty} \frac{1}{p^{\frac{5}{2}}} \cos\left(2\pi p\left(\frac{F}{B} - \gamma\right) \pm \delta\right) \tag{1.7}$$

where p represent the harmonic number and $\pm\delta$ phase shift related to dimensionality of the Fermi surface. Including several damping factors, the general formula for magnetoconductivity is given by [49].

$$\frac{\Delta\sigma}{\sigma} \propto \sum_i S_{ex}^i B^{\frac{1}{2}} \sum_{p=1}^{\infty} R_T R_D R_S \cos\left(2\pi p\left(\frac{F_i}{B} - \gamma_i\right) \pm \delta\right) \tag{1.8}$$

Here γ_i is the phase factor related to band topology, $R_T, R_{D,} R_S$ are the temperature reduction, impurity damping and spin reduction factors respectively. The first correction factor R_T accounts for the temperature effect on the Fermi-Dirac distribution function. The term R_T is expressed as [49],

$$R_T = \frac{2\pi^2 p k_B T m^* / e\hbar B}{\sinh\left(2\pi^2 p k_B T m^* / e\hbar B\right)} \tag{1.9}$$

where k_B is the Boltzman constant. As the temperature increases, the thermal broadening of LLs results in drop of amplitude of QOs and its temperature dependent profile allows the effective mass m^* to be deduced. This is usually small when the Dirac/Weyl points are close to the Fermi level, while m^* increases with increasing distance between the Fermi level and the node [54]. From m^* one can also calculated the Fermi velocity of relativistic fermions, $v_F = \frac{\hbar k_F}{m^*}$, where k_F can be obtained from S_{ex}.

Returning to another damping factor of QOs, R_D. It is called the Dingle damping term and is associated with impurity quantum scattering of relativistic fermions. R_D can be expressed as [49],

$$R_D = exp\left(-2\pi^2 p k_B T m^* / e\hbar B \frac{T_D}{T}\right) \tag{1.10}$$

where T_D is the Dingle temperature. Any finite scattering will result in broadening of the LLs, which can be associated with the quantum relaxation time (τ_q), given by the relation, $\Gamma = \hbar/2\tau_q$. The T_D can be extracted from the QOs by linear fitting of logarithmic plot of amplitude of oscillations vs $1/B$. The estimated Dingle temperature yields τ_q via the relation $\tau_q = \hbar/2\pi k_B T_D$. Remarkably, τ_q can be used to calculate an important parameter related to material transport i.e. quantum mobility (μ_q) via $\mu_q = e\tau_q/m^*$. μ_q calculated in this way is always lower than that obtained from the Drude model as the classical Drude mobility is unaffected by forward scattering, whereas μ_q takes into account scattering in all directions [55].

The final damping term, R_S, is associated with spin splitting caused by the Zeeman effect, which produces a phase shift between LLs sub-bands with opposite spins. This results in a reduction of the amplitude of QOs given by [49],

$$R_S = \cos\left(\frac{p\pi}{2}\frac{gm^*}{m_e}\right) \tag{1.11}$$

where m_e is the free electron mass and g is the Landé g factor. R_S is field independent and provides an alternative way do determine g, that can also be extracted from the peak splitting in QOs. Such analysis has been presented for topological semimetal ZrSiS [56]. Furthermore, the Landé g factor can also be estimated using the spin zero effect [49]. This phenomenon is defined as the disappearance of the fundamental oscillation while its second harmonic is enhanced at a certain field orientation due to the interference of spin-split Fermi surfaces. Interestingly, we recently reported on the zero spin effect in $TaAs_2$ caused not by changes in field orientation, but in temperature [57].

Another parameter that can be extracted by studying quantum oscillations is the phase factor γ, which is of particular interest for topological materials.. This is because γ is associated with the Berry phase (ϕ_B) through the relation $\gamma = \frac{1}{2} - \frac{\phi_B}{2\pi}$ [58]. Ideally, for a linear band dispersion, $\phi_B = \pi$. It may deviate when band dispersion changes or in the presence of strong Zeeman field [54]. ϕ_B can be derived from QOs by plotting the Landau level fan diagrams.

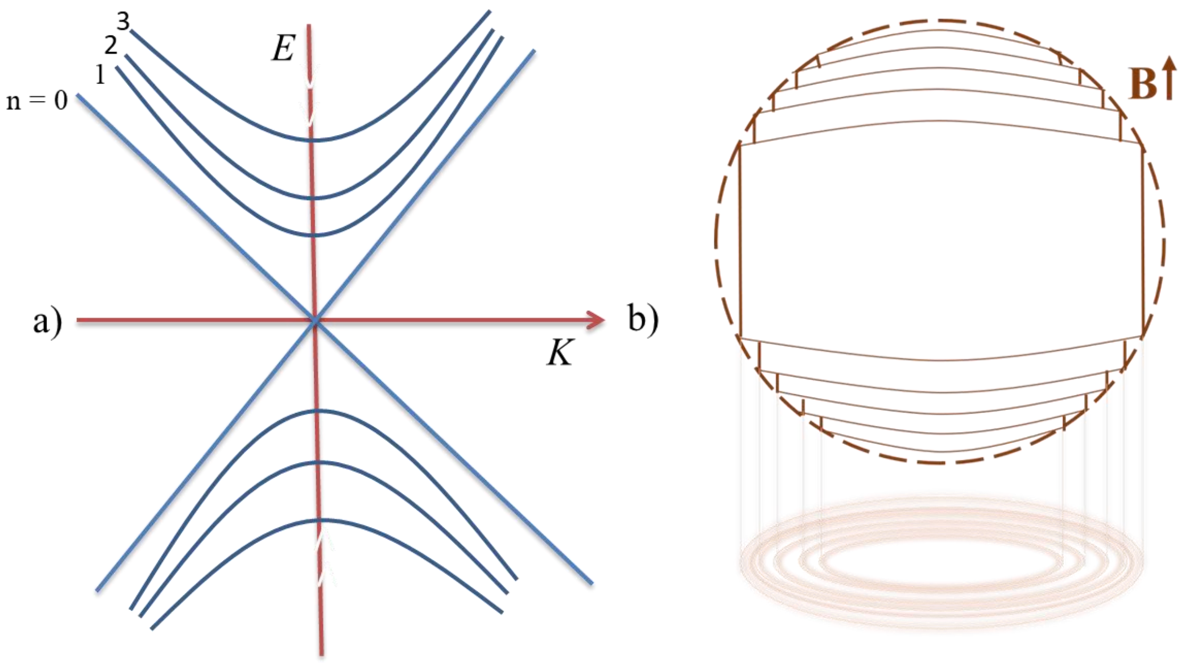

Figure 1.3. Schematic representation: (a) Relativistic Landau level spectra under applied magnetic field. (b) Cylindrical Landau tubes crossing through a 3D Fermi surface.

1.2.2 Anomalous Hall and Nernst effect

The classical Hall effect occurs in a conductor subjected to a mutually perpendicular magnetic field and current. It was discovered in 1879 and has become an invaluable tool for accurately measuring the concentration of carriers in conductors [59]. For a single band system, the Hall signal is proportional to the magnetic field, but two years after initial discovery, it was found that in Iron the response is stronger at low magnetic field [60]. This implied the presence of additional contributions to the ordinary Hall effect (OHE) from extraordinary or anomalous Hall effect, which is defined as the development of the transverse signal orthogonal to an applied electric field even without presence of external magnetic field. The thermoelectric counterpart of AHE and ANE, is also defined as the generation of transverse voltage in response to the application of thermal gradient without the involvement of a magnetic field [61]. Evidence of AHE can be experimentally distinguished from OHE, as the former steeply increases at low magnetic field and eventually saturates.

Very early it was realized that the AHE in ferromagnetic conductors is proportional to the magnetization. The empirical relation that describe the total Hall resistivity governed by OHE and AHE is given by,

$$\rho_{yx} = R_o H_z + R_s M_z \tag{1.12}$$

where H_z, M_z, R_o, R_s are the applied magnetic field, magnetization, ordinary Hall coefficient and anomalous Hall coefficient respectively. In particular, the anomalous Hall coefficient R_s is material specific, in contrast to R_o which is purely a function of the carrier concentration. It has recently turned out that R_s can be very high in topological materials [62–64]. The anomalous Hall effect can result from either (i) an intrinsic mechanism or it might originate from the (ii) extrinsic mechanism. The latter is further divided into two categories: skew scattering and side jump mechanism.

(i) Intrinsic mechanism

In 1954, Karplus and Luttinger (KL) first proposed a theory to describe the anomalous Hall conductivity in solids [65]. They showed that electrons can develop a group or anomalous velocity perpendicular to the applied electric field and this anomalous velocity, which is due to the electronic structure, generates AHE. The total anomalous velocity for ferromagnetic solids with all the bands occupied becomes nonzero, contributing to the AHE. Later, it was shown that the anomalous velocity can be understood within the Berry curvature concept [5]. The Berry curvature was dubbed as anomalous velocity of electrons as a result anomalous Hall voltage developed. The discovery of topologically non-trivial materials had a profound impact on the study of anomalous effects, since linear band crossing gives rise to a non-zero Berry curvature [51]. In the aspect under discussion, this is particularly important for Weyl semimetals, where the presence of opposite chiral Weyl points acts as source of sink of Berry curvature. When the time reversal symmetry is broken, the Berry curvature from

Weyl nodes within the pair does not cancel and can act in a manner analogous to a magnetic field. This leads to anomalous velocity perpendicular to the applied electric field even in a zero magnetic field [62].

Large intrinsic anomalous Hall and Nernst effects have been reported for several time-reversal-breaking Weyl semimetals, such as $Co_3Sn_2S_2$ [66], Co_2MnGa [63], Mn_3Sn [67], $MnGe_3$ [68], etc. It has also been shown that a large intrinsic anomalous contribution can be observed by tuning the location of Weyl points [69]. Recently, we have also reported the sign change of anomalous Hall and anomalous Nernst effects in a ferromagnetic Weyl semimetal CeAlSi [70]. In this article we show that the anomalous properties in the magnetic phase are determined by the shift of the Weyl point driven by the reconstruction of the magnetic spins, and in the paramagnetic phase the position of the Weyl point with respect to the Fermi level determines the anomalous properties.

(ii) Extrinsic mechanism

The anomalous Hall and Nernst effect also can originate from the scattering of charge carries of the magnetic impurities, namely skew scattering or side jump. The idea that the asymmetric scattering from impurities caused by the spin-orbit interaction is responsible for anomalous Hall effect was first proposed by J. Smith in 1955 [71]. The asymmetric scattering, also known as skew scattering, is illustrated in Fig. 1.4a. In this mechanism, the spin-orbit coupling of the impurity scattered the spin up and spin down electron in an asymmetric manner, which contributed to the AHE. The skew scattering obeys a specific relationship between the transverse anomalous Hall resistivity (ρ_{yx}) and the longitudinal resistivity (ρ_{xx}) i.e. $\rho_{yx} \propto \rho_{xx}$ [51].

Another type of scattering that can lead to AHE, namely side jump, was introduced by L. Berger in 1964 [72]. In this mechanism the spin up and down electrons experiences a transverse shift to the incident direction due to influence of the electric field of the impurities. The side jump mechanism is also shown schematically in Figure 1.4b. In this mechanism, ρ_{yx} follows quadratic dependences with ρ_{xx}, i.e. $\rho_{yx} \propto \rho_{xx}^2$ [51].

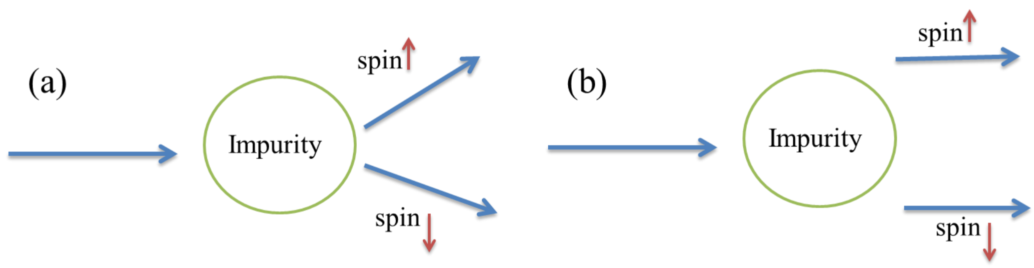

Figure 1.4. Schematic representation of (a) skew scattering; (b) side jump mechanism.

1.2.3 Chiral anomaly

The concept of a quantum anomaly, which emerged in the field of high-energy physics, describes the breakdown of classically conserved symmetries as quantum effects are turned on [73]. For instance, parity and charge conservation is violated when a pion (π^0) decays into two photons, providing the first evidence of a chiral anomaly, also known as the Adler-Bell-Jackiw anomaly [74]. Remarkably, in 1983 H.B. Nielson and M. Ninomiya predicted that the chiral anomaly should occur in relativistic Weyl fermions system when parallel electric and magnetic fields are applied [75]. After it was experimentally shown that the Weyl electronic system can be found in some semimetals, this phenomenon is extensively investigated by several research groups [32,53]. In the quantum limit, the chiral anomaly is the manifestation of pure and opposite chirality of the lowest Landau level of the Weyl cones pair. Application of parallel electric field along with the magnetic field can accelerate the chiral charges from one Weyl cone to other at lowest Landau level as illustrated in Fig. 1.5, and thus the net chirality of the individual nodes becomes unbalanced. The charge pumping rate of a Weyl node is given by [12],

$$\frac{\partial \rho_\chi}{\partial t} = -\chi \frac{e^3}{4\pi^2\hbar^2} E.B \tag{1.13}$$

where ρ_χ, χ represent charge density and chirality of Weyl fermions. Chiral charge pumping of Weyl fermions leads to an anomalous current (or a chiral conductivity), which can be detected in transport measurements as a negative longitudinal magnetoresistance. Since the chiral imbalance can be relaxed by inter-Weyl scattering (τ_i), the anomalous chiral current is proportional to $\propto E.B.\tau_i$. This means that large τ_i is necessary to observe large NLMR [12]. In the quantum limit the chiral conductivity varies linearly with the magnetic field, whereas in the classical limit it shows quadratic dependence [76]. There is a number of reports of NLMR in Dirac and Weyl semimetals that have been attributed to the presence of a chiral anomaly [23,32,38,39,39,53]. However, it is not always the case even if the negative longitudinal magnetoresistance is observed. For instance, it can be induced by current jetting effect [77] or may be related to the anomalous Hall effect [78]. Therefore, complementary experiments like measurements of the thermoelectric power, thermal conductivity, planar Hall effect and planar Nernst effect are vital to exclude artefacts and probe the intrinsic chiral behavior of Weyl fermions [53]. The investigation of the thermoelectrical coefficients provides a unique opportunity to probe the chiral anomaly free from artefact as the thermopower is measured open circuit condition without charge current flow [79]. Recently, we have also reported of the presence chiral anomaly in the topological Dirac semimetal α-Sn using electrical and thermoelectrical measurements [29].

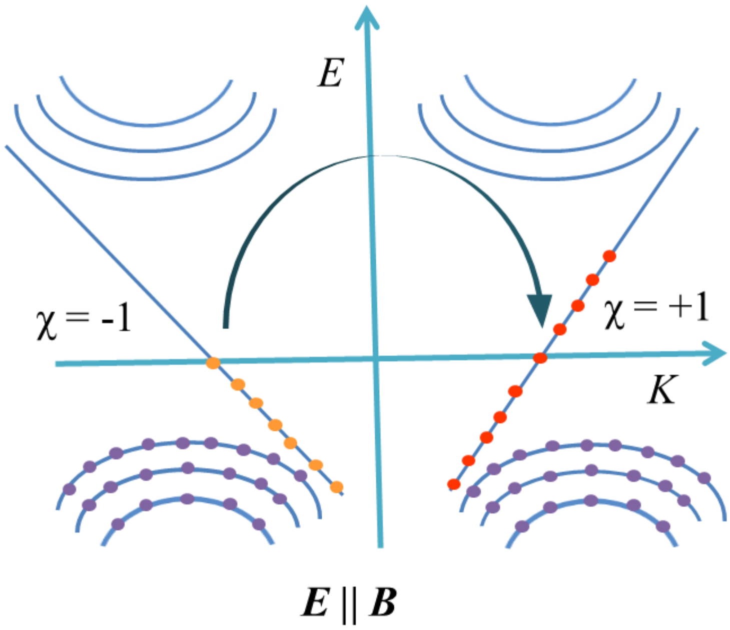

Figure 1.5. The pumping of Weyl fermions between Weyl nodes of different chirality when a parallel electric field is applied along with a magnetic field.

1.3 Thermoelectric transport coefficients

The discovery that a temperature difference between the junctions of two conductors connected in a closed loop leads to the generation of a magnetic field (due to the flow of electric current) was made by Thomas J. Seebeck in 1821 and published in 1825 [80]. It has been later realized that the basis of this phenomenon is that the flow of charged particles in a conductor is accompanied by a flow of entropy [81]:

$$j^s = Sj^e - \kappa \frac{\nabla T}{T}, \tag{1.14}$$

where j^s is the entropy flow, S the Seebeck coefficient, j^e the charge current density, κ the thermal conductivity and ∇T the thermal gradient. Generally, the total charge current in presence of the thermal gradient can be written as [82]:

$$j^e = \sigma E - \alpha \nabla T, \tag{1.15}$$

where E is the electrical field whereas α and σ denote the thermoelectrical conductivity and electrical conductivity tensors, respectively. When $j^e = 0$, Eqn. 1.13 can be rewritten as

$$\alpha\sigma^{-1} = E/\nabla T, \tag{1.16}$$

thus, $S = \alpha / \sigma$, also known as the thermoelectric power or shortly thermopower, quantifies a tendency of an electronic system to generate an electric field in response to a thermal gradient. When $\nabla T \parallel \hat{x}$ and $B \parallel \hat{z}$, S_{xx} can then be expressed as [83]:

$$S_{xx} = \frac{E_x}{\nabla T} = \frac{\alpha_{xx}\sigma_{xx} - \alpha_{xy}\sigma_{xy}}{\sigma_{xx}^2 + \sigma_{xy}^2}, \tag{1.17}$$

In the presence of a mutually perpendicular magnetic field and thermal gradient, charged particles moving in a solid will deviate from their trajectory due to the Lorentz force. As a result, a finite transverse thermoelectric response is generated, also known as the Nernst effect. This is a manifestation of transverse entropy flow caused by longitudinal current flow [84] with Nernst signal S_{xy} given by [83]:

$$S_{xy} = \frac{E_y}{\nabla T_x} = \frac{\alpha_{xy}\sigma_{xx} - \alpha_{xx}\sigma_{xy}}{\sigma_{xx}^2 + \sigma_{xy}^2} \tag{1.18}$$

The sign of the Nernst effect is not straightforward to predict as it is determined by the difference of two contributions of similar magnitude. The situation where they are equal, hence the resulting Nernst signal is zero, is called the Sondheimer cancellation [85].

The magnetic field affects thermoelectric conductivity and according to the linear Boltzmann formalism the longitudinal and transverse response in a classical system are given by [82]:

$$\alpha_{xx} = \frac{\alpha_0}{1 + \mu B^2} \tag{1.19}$$

$$\alpha_{xy} = \frac{\alpha_0 \mu B}{1 + \mu B^2} \tag{1.20}$$

where α_0 is zero field thermoelectric conductivity and μ is the mobility. It is evident from Eqns. 1.15 and 1.16 that the magnitude of the thermoelectric coefficients is controlled by the product of mobility and magnetic field similar to the electrical conductance. In the weak field limit ($\mu B \ll 1$), the transverse response is linear, whereas the longitudinal response is weakly field dependent.

Remarkably, N.F. Mott and H. Jones in 1936 provided the link between the thermoelectric conductivity and electric conductivity [86]:

$$\alpha = \frac{\pi}{3}\frac{k_B^2 T}{e}\frac{\partial\sigma}{\partial\epsilon}|_{\epsilon=\epsilon_F} \tag{1.21}$$

This expression implies that the thermoelectric conductivity is proportional to the energy derivative of electrical conductivity, which means that relatively small variation of $\sigma(\epsilon)$ around the Fermi level can manifest as a large change of α [87].

The sign of the thermopower can be positive or negative depending on the curvature of the Fermi surface, with some exemptions, such as nobel metals [82]. However, the energy dependent scattering time can affect the value of α [88]. For a multiband conductor, the total thermoelectric signal is a sum of individual band contributions S_i, weighted by the respective conductivities σ_i: $S = \frac{\sum_i S_i \sigma_i}{\sigma}$.

The magnitude of thermoelectric response is proportional to $k_B T/\varepsilon_F$, what make them useful in studies of topological semimetals where the Fermi energy is low, hence a large thermoelectric response can be expected in these materials [89] [Phys. Rev. B 99, 155123]. The magnitude of Seebeck and Nernst coefficient (ν) for a single band conductor at low temperatures is given by [82]:

$$S_{xx} = \frac{\pi^2}{2}\frac{k_B}{e}\frac{T}{T_F} \tag{1.22}$$

$$\nu = \frac{\pi^2}{3}\frac{k_B^2 T}{e\epsilon_F}\mu \tag{1.23}$$

Here, T_F represents the Fermi temperature, and e denotes the electronic charge.

In fact, many research groups have shown interest in studying the thermoelectric properties of topological semimetals, particularly in magnetic fields [32,37,52,63,83,84,89,90], because such measurements can be a sensitive tool to study the unconventional band structure of these materials. For instance, thermoelectrical quantum oscillations of different topological semimetals can help to probe the Fermi surface with better resolution than Shubnikov - de Hass oscillations [91]. Other phenomena associated with non-trivial topology, such as the chiral anomaly or the anomalous magneto-transport, have also been widely investigated using thermoelectrical transport [52,92].

In the end, it is worth mentioning that the thermoelectric phenomena can have other than diffusive origin. A relatively common one is phonon-drag thermoelectric power (S_g). The temperature gradient causes phonon currents to flow from the hot to the cold end of the sample. At low temperatures, due to the large mean free path of the phonons, they can effectively pull the charge carriers along the direction of the phonon current by momentum transfer. Thus, a net charge imbalance of the sample is generated, as a result an electric field was developed to prevent further accumulation of charge carriers, which constitute as S_g. The approximate magnitude of the phonon-drag thermoelectric power in metals is given by [88],

$$S_g = \frac{C_g}{3n_0 e}\left(\frac{\tau_p'}{\tau_p' + \tau_{pe}}\right) \tag{1.24}$$

where, C_g is lattice heat capacity, n_0 carrier concentration, τ_{pe} is the relaxation of phonon due to electron-phonon coupling and τ_p' is phonon relaxation time due to other interactions of phonon except electron-phonon. At high temperatures, S_g drastically decreases due to increasing rate of phonon-phonon scattering. Typically the maximum contribution of S_g in metals has been observed around the temperature $T \approx \theta_D/5$, where θ_D is the Debye temperature [88].

1.4 Motivation and objective of the thesis

The remarkable discovery of the topological insulator has led to extensive research into the topological aspects of electronic structure [8]. Soon afterwards, it has been realized that the nontrivial topology can occur in many other materials, including semimetals, which triggered another wave of research interest [11]. The electronic structure of topological semimetals hosts quasiparticles arising from band crossings between the valence and conduction bands. Manifestations of these low-energy electronic excitations can be found, among others, in unusual transport properties in presence of a magnetic field. In other words, by measuring the transport properties of topological semimetals one can probe the nontrivial topology of the electronic structure. These studies include investigations of quantum oscillations providing information about the Fermi surfaces; the anomalous Hall effect arising from non-zero Berry curvature; and the chiral anomaly consisting of charge pumping of Weyl fermions. It is worth noting that complementary transport measurements, such as thermoelectric ones, provide an exceptional opportunity to explore the properties of topological semimetals in more depth.

This work is motivated by the fact that measurements of thermoelectric coefficient appear to be very useful, though perhaps somewhat underrepresented, way of investigating the properties of topological semimetals. For instance, as suggested by the Mott formula, thermoelectric coefficients should be more sensitive to changes in energy dispersion at the Fermi level than their electrical counterparts. Therefore, the thermoelectric transport measurements can offer precise information about the Fermi surface in studies of quantum oscillations [91]. Another example is the anomalous Nernst effect, which is expected to be more sensitive to the non-zero Berry curvature than anomalous Hall effect, if Weyl nodes are not placed exactly on the Fermi level [93]. Furthermore, chiral current of Weyl semimetals can be detected using thermoelectric transport measurements without application of external electrical current, which makes it more robust to experimental artefacts [53].

Inspired by these facts, we decided to investigate properties of three topological semimetals using combined electrical and thermoelectric transport measurements. In a magnetic field, these materials were showing many unusual characteristics. For example, $TaAs_2$ is expected to become a Weyl semimetal when a magnetic field is applied [94], which should induce an additional phase in the electron wave functions. This, in turn, will affect quantum oscillations and can result in emergence of the spin-zero effect [95]. The ferromagnetic Weyl semimetal CeAlSi, on the other hand, has been identified as a new type of topological material, where the Weyl points arise from broken inversion symmetry. By breaking time-reversal symmetry, these points can be shifted in k-space making CeAlSi an intriguing object to study the interaction between magnetism and topology [96]. Hence, in this material we chose to look for the anomalous Hall effect and the complementary anomalous Nernst effect. In the latter, the response to the non-zero Berry curvature is different from that of the anomalous Hall effect, allowing some conclusions to be drawn about the position of the Fermi level. Finally, we have selected an elemental α-Sn in a form of a strained thin film to study the quantum anomaly, whose manifestations were found by our colleagues in electrical measurements [97]. The electronic structure of strained α-Sn thin film has a pair of Dirac cones are protected by four-fold rotational symmetry [28], but the application of magnetic field turns α-Sn into a Weyl semimetal. This makes α-Sn a suitable candidate to investigate the chiral anomaly, which, if true, should also be seen in thermoelectric transport.

CHAPTER 2

EXPERIMENTAL SECTION

Various experimental techniques can be deployed to study topological nontrivial material. In this thesis, I will focus on measurements of transport and thermoelectric properties, but in order to obtain reliable results to draw solid conclusions, high-quality samples are needed first and foremost. These samples can be grown in bulk or thin film form. We studied two bulk single crystals, namely $TaAs_2$ and CeAlSi grown by chemical vapor transport and self-flux method respectively. We also measured a single-crystalline thin film of α-Sn fabricated by molecular beam epitaxy (MBE).

This chapter will be structured as follows. First, I will give a brief description of the techniques used to grow the single crystals selected for measurements. Next, I will give a brief description of our cryostat, which is equipped with a superconducting coil capable of generating a 14.5/16 T magnetic field. Subsequently, I will introduce our self-made electrical and thermoelectric probes. Finally, I will discuss the sample preparation and the procedure of electrical and thermoelectric measurements.

2.1 Single crystal growth techniques

In order to obtain high quality samples, we collaborated with three different experimental research groups. Two of them are from Institute of Physics, Polish Academy of Sciences (IF PAN), Poland, and one from the Boston College, USA. $TaAs_2$ and α-Sn were grown by the MagTop ON6.1 group at IF PAN, while the magnetic Weyl semimetal CeAlSi was synthesized in the Tafti Lab at Boston College, USA.

2.1.1 Chemical vapour transport method

Chemical vapour transport (CVT) is a widely used method for growing high purity single crystals [98]. In the simplest of terms, this process requires reactants, a transport agent (typically elemental halogens) and a temperature gradient. A schematic description of the CVT is shown in Figure 2.1, and the principle of the process can be described as follows. Initially, a precursor is mixed with a transport agent and kept in a vacuum sealed quartz ampoule. This ampoule is then placed in an oven and subjected to a temperature gradient. Initially, the transport agent sublimates and reacts chemically with the precursor in the quartz ampoule, which converts the solid form of a precursor into a gaseous derivative. The temperature gradient forces the gaseous derivative to migrate either from the hot zone to the cold zone ($T_2 \rightarrow T_1$) or vice versa ($T_1 \rightarrow T_2$), depending on the nature of the reaction between the precursor and transport agent. Finally, crystallization takes place in the cold zone (T_1) if the reaction was endothermic, whereas while it take places in the hot zone (T_2) if the reaction was exothermic.

$TaAs_2$ single crystals were prepared by two stage CVT. Initially, polycrystalline $TaAs_2$ was synthesized using direct reaction of Tantalum foils (ZR Industrial Ltd, 99.99%) and Arsenic (PPM Pure Metals, 99.999995%) in a vacuum sealed in a quartz tube. This reaction occurs at the temperature of 990 °C and takes 19 days in a furnace. The furnace is then cooled down to room temperature and polycrystalline $TaAs_2$ is extracted from the quartz tube.

To make single crystals, polycrystalline $TaAs_2$ was first palletized and then placed inside the vacuum-sealed quartz tube along with iodine (transport agent). The temperature gradient is then applied to the quartz tube in a furnace. The source zone (T_2) was kept at 1025 °C, while the sink zone (T_1) was kept at 956 °C for 23 days. The furnace was then cooled down to room temperature at a rate of 100 °C/h and the single crystals of $TaAs_2$ can be extracted from the sink zone. For more details on the growth and characterization of $TaAs_2$, see Ref. [99].

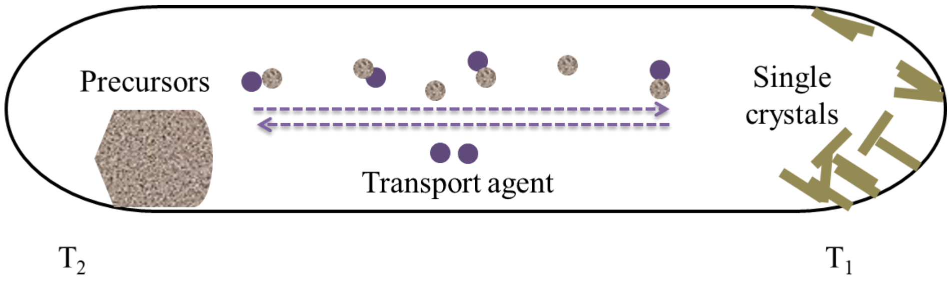

Figure 2.1. A schematic representation of chemical vapour transport method.

2.1.2 Flux method

The flux method is a long known and still very popular technique for growing single crystals, in which a low melting point solvent (flux) is used to dissolve the solute. First, a high-melting crucible filled with a solute is placed in a furnace. The oven temperature is increased to completely dissolve the solute and left for some time to obtain a homogeneous solution. The next step is to lower the temperature at a specific rate to reduce the solubility of the solute. This continues until the supersaturation point is reached, where the concentration of the solute is greater than its solubility. At this instant, small nuclei begin to grow and, with further temperature reduction, these nuclei fuse together, eventually leading to the formation of crystals. The residual flux can be removed with a solvent (e.g. by using hot dilute nitric acid for several days) or quickly decanted by centrifuge while still in the liquid phase.

Self-flux method used to grow CeAlSi single crystals is called the "self-flux method" because the flux components are the same as in the desired compound. Initially Ce, Al and Si were mixed in a weight ratio of 1:10:1 in a Canfield crucible. This crucible was then sealed and placed inside a quartz tube evacuated using a vacuum pump. Subsequently, the sealed quartz tube is place inside a furnace, heated to 1000 °C at a rate of 3 °C/h and held for 12 h. Cooling was then commenced to 700 °C at a rate of 0.1 °C/h and the held for 12 h. The residual flux was removed and then crucible was rapidly cooled to room temperature. More detailed information on the preparation of CeAlSi can be found in Ref. [96].

2.1.3 Molecular beam epitaxy

The molecular beam epitaxy (MBE) machine offers a number of capabilities that are beneficial for the growth of high-purity epitaxial layers. For example, the inner space of the system is kept at the ultra-high vacuum (UHV) to ensure efficient deposition of high purity epitaxial layers with in-situ reflection high-energy electron diffraction (RHEED) capability. The latter allows accurate monitoring of the growth process [100]. A generic diagram showing a simplified principle of the MBE machine is presented in Fig. 2.2.

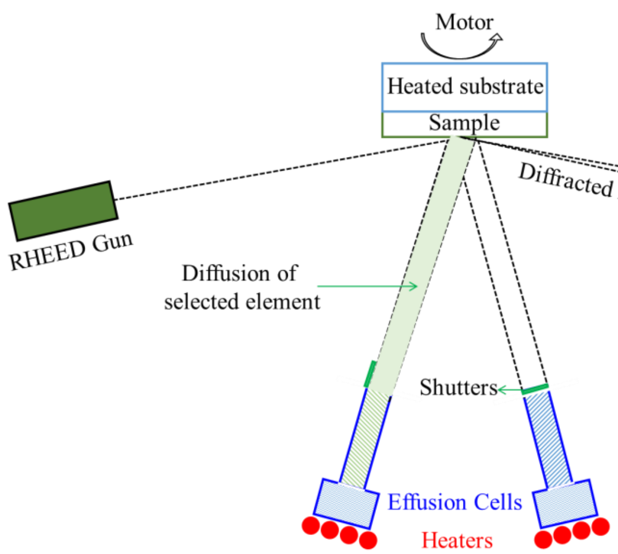

Figure 2.2. A simplified schematic representation of molecular beam epitaxy used for the growth of α-Sn thin film.

At the bottom of the UHV chamber, two or more effusion cells or Knudsen effusion cells (K-cells) are installed which comprise of crucibles in order to hold the source elements. One of the important requirements for successful layer growth is the capability to generate stable, reproducible and uniform molecular beams of elemental constituents [101]. The K-cells are directed towards the substrate to place pure element on the substrate. The precursors held in the effusion cells are heated up and sublimated which are then transferred to the heated sample holder in the form of molecular beams. In case of liquid source materials, the starting elements are evaporated and beamed in the same pattern as for solid precursors. Heating of the effusion cells is typically achieved by using either resistive or electron beam energy source [101]. The choice is based on the required flux and the melting point of the source material stored in the crucibles. The effusion cells are armed with shutters to control deposition of the substances. Once they are open, physical vapour from each K-cell is diffused towards the substrate to deposit a layer. In a typical MBE chamber, the sample holder consists of a heating source and a sample rotating component which is used to achieve uniform growth of the films. The RHEED gun is used to characterize the deposited layers in-situ during the growth process. The gun emits electrons at a very low angle with respect to the sample's surface which produce a diffraction pattern. The in-situ RHEED characterization can yield information about surface structure, cleanliness, smoothness and growth rate [102], which helps in understanding the details to produce a sample with the preferred properties.

For our study, α-Sn thin film was grown on GaAs (001) substrate with 4 μm CdTe buffer layer. The desired lattice mismatch between CdTe and α-Sn incorporates an in-plane compressive strain (~0.1 %) in α-Sn, leading to the formation of a Dirac semimetallic phase (DSM). Detailed description of the growth procedure and structural information available in Ref. [97].

2.2 High field cryogenic system

High magnetic field and low temperatures are highly desirable conditions to study the quantum transport properties of materials. The former can drive an electronic system to extreme states, such as a quantum or chiral limit, while the latter reduces the thermal broadening of energy levels and allows one to measure low energy quantum phenomena . All the transport measurements data presented in this thesis were measured in a high magnetic field cryostat system. The superconducting electromagnet coils were manufactured by Cryogenic Consultant Limited, while the cryostat was manufactured by KrioSystem. A schematic representation of our High field cryogenic system shown in Fig.2.3. Here I will shortly discuss key components of the experimental rig and its operating procedures.

We used a “wet” passive cryogenic system that required filling with liquid helium (LHe) to operate. To reduce a heat exchange between the inner and outer space of the cryostat they were separated with vacuum jackets and the liquid nitrogen (LN_2). While high vacuum prevents a convective and diffusive heat transfers, the thermal radiation was reduced by multiple layers of mylar foil (also referred to as a superinsulation). To further reduce the thermal radiation, the nitrogen tank (jacket) was installed in such a way that it surrounds the inner vessel. This was filled with LHe in which the superconducting coil was immersed. At the boiling temperature of helium at atmospheric pressure (4.2 K for ${}^{4}_{2}\mathrm{He}$) the superconducting coil was able to generate a magnetic field of ±14.5 T, which allowed us to study the magneto-transport in a wide range of conditions. To control the temperature of a sample we used the variable temperature insert (VTI) into which a sample probe was inserted. LHe from the main bath was sucked to VTI through a needle valve, after which it was transformed into gas of desired temperature at a heat exchanger and drawn to the sample space. The temperature of the heat exchanger was measured by Rhodium Iron (RhFe) thermometer and controlled by a resistive heater. An evacuation port (located at the top flange of the VTI) was connected to a rotary pump that allowed us to keep the gas pressure in VTI below atmospheric pressure.

There are several steps needed to be performed to prepare a system for measurements. To maintain high vacuum in vacuum jackets of cryostat and VTI we used Edwards pump station that was set of a scroll and turbo molecular pump. We pumped the vacuum for a few days and waited for the pressure to reach 10^{-6} mbar before cooling the system. Next we filled the nitrogen jacket with LN_2 and waited until the superconducting coil cooled down to a temperature of about 160 K through thermal radiation. This cooling process took at least 72 hours, but allowed us to keep the main bath filled with helium gas. During this process the coil temperature was monitored by another RhFe thermometer, which was attached to the lambda plate placed above the superconducting coil. After reaching the desired temperature, we could start filling the helium reservoir with a liquid through a double sided transfer tube by ICE Oxford. The level of LHe was monitored by a liquid helium level meter DLG200 constructed by Cryogenic Consultant Ltd. An exhaust port at the head of the cryostat was connected to the recovery line to continuously release the overpressure of the helium gas from the reservoir.

When the system was filled with LHe the sample probe could be inserted inside VTI. In order to easily regulate the flow of helium through the originally manual needle valve during measurements, we connected it to a stepper motor controlled from a personal computer (PC). An additional electronic valve by Leybold (also controlled from PC) was attached to the pumping line to fine tune the He pressure inside the VTI. This was monitored by an electronic pressure gauge by Leybold which, like all other instruments, was read and controlled by measurement software that was written and run in the National Instrument Labview environment.

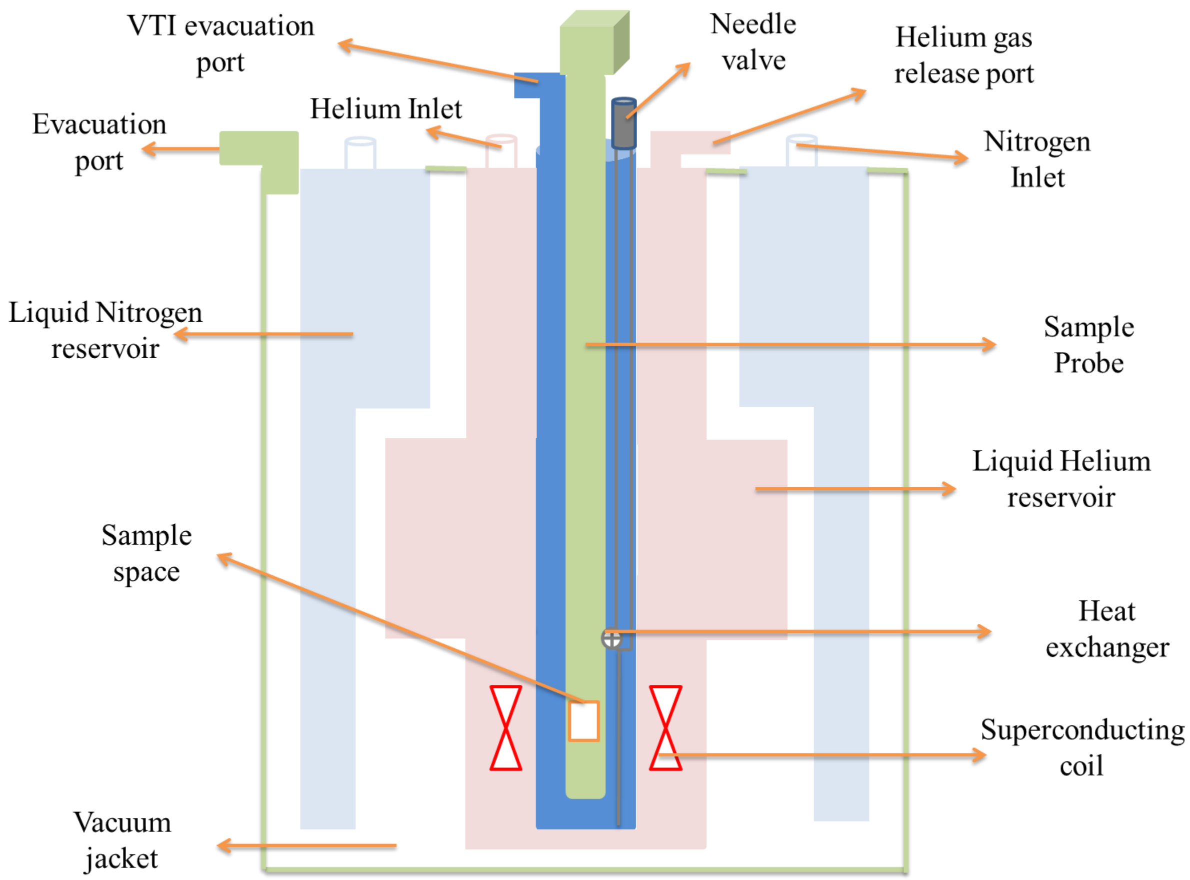

Figure 2.3. A schematic representation of the cryogenic system.

2.3 Electrical probe

Electrical transport properties were measured using a custom-made probe equipped with a sample holder allowing 360° rotation of the sample. It is shown in Figure 2.4, where three panels present the three different segments of the probe. The left section shows the head of the probe fitted with a rotary knob that allows us to manually control the angle of the sample tilt with high precision. The actual position can be read from the dial. Below, the probe has installed five copper discs five copper disks are installed to prevent radiative heat transfer to the sample from the top of the probe being at room-temperature. For the electrical connection, a set of twisted pairs made of thin copper wire are used. These wires connected to the external devices through a multi-pin hermetic connector shown in the center panel of

Fig.2.4. The most important part of the probe, shown in the right panel of the Fig. 2.4. The sample holder consists of an 8-pin socket connected to a wheel, the position of which is controlled by the knob. To accurately determine the sample temperature, a Cernox thermometer is attached to the sample holder.

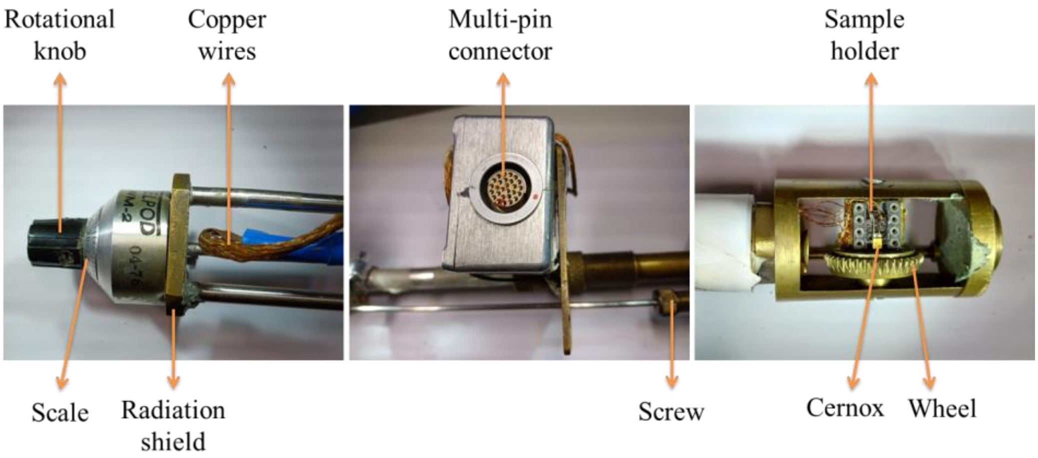

Figure 2.4. Different parts of our hand crafted electrical probe

2.4 Thermoelectric probe (TEP)

Thermoelectric coefficients are measured with another custom-made probe. I will again discuss its construction by describing the three segments - these are shown in Figure 2.5. The head of the probe shown in Figure 2.5a consists of a vacuum port, a stepper motor connector and a multi-pin sample connector. Figure 2.5b presents the base of the probe, where we have 16 pairs of coils made of 25 µm thick phosphor - bronze wire for the electrical connections. These are connected to twisted pairs made of 50 µm copper wire leading to the top of the probe. To prevent electrical shortcuts between twisted pairs and the probe, a cigarette paper was glued to the tube, which joins the head and base of the problem and Teflon tape was wrapped around. The twisted-pair cables are fed into the base via a vacuum-tight electrical conduit prepared using a Stycast 2850FT epoxy. The base consists of several components, including a beryllium oxide chips for connections, a couple of gears and the sample space. The beryllium oxide chips, due to their high thermal conductivity, are used as thermal anchors to equalize temperature of the wires. The gears made of brass are controlled by the stepper motor allow us to measure the angular variation (± 180° out-of-plane) of thermoelectric coefficients. An enlarged view of the sample space is presented in Figure 2.5c. Two phosphor - bronze blocks are fixed together using Vespel fittings and tensioned with a stainless spring – a sample is mounted between them. In order to induce a thermal gradient along the sample we used resistive heater of 10 kΩ resistance glued with GE varnish into one of the blocks. For determination of temperature gradient two Cernox thermometers were attached to the Ph-Br blocks using Stycast 2850FT epoxy. Figure 2.5d shows the brass can that was used to seal the base of the probe to make it vacuum-tight.

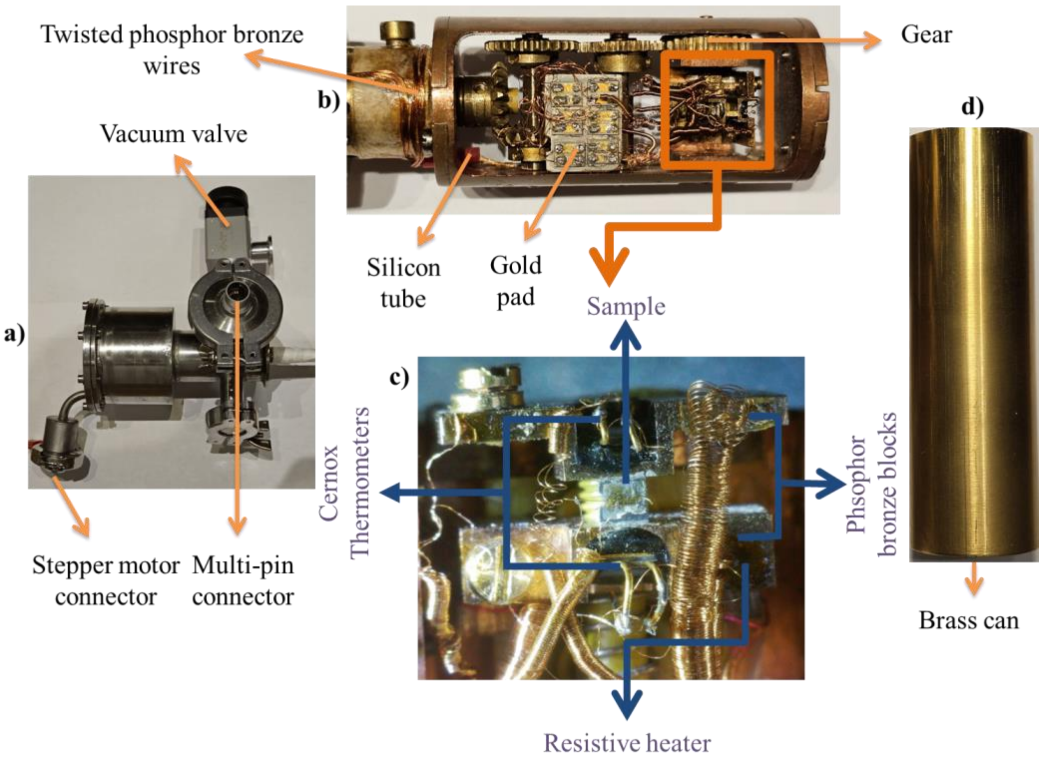

Figure 2.5. Sections of our custom-made thermoelectrical probe

2.5 Electrical transport measurements

In the past decade, many unusual electrical transport phenomena have been reported in topological semimetals. For example, in the presence of a magnetic field (B) observation of changes to the electrical resistivity (i.e. magnetoresistance, MR) and Hall resistivity provide opportunity to study the extraordinary behavior of Dirac and Weyl fermions. We measured the temperature dependences of the resistivity for all materials studied and also magnetic field dependences of the magnetoresistance and Hall resistivity for several fixed temperatures. To determine the longitudinal and transverse electrical signals we used contacts arranged in the standard Hall bar configuration shown in Fig. 2.6.

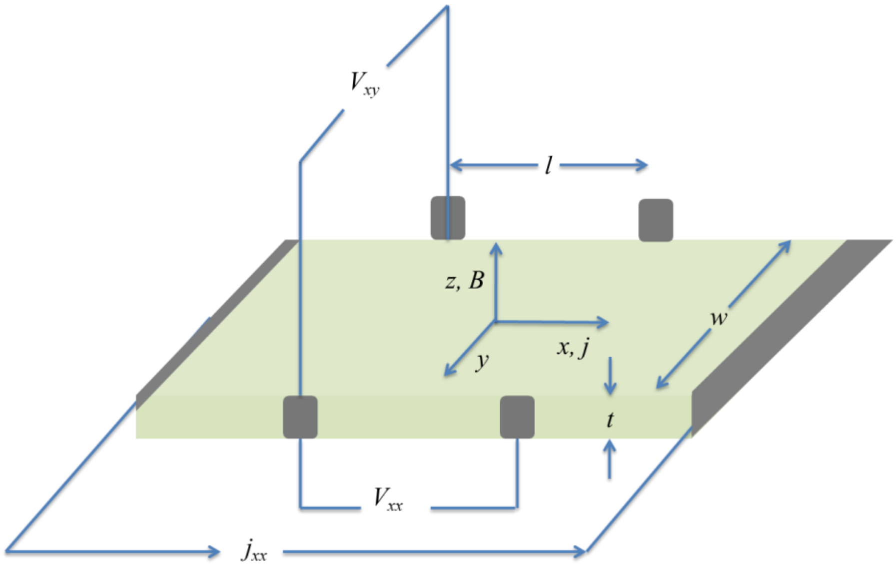

Figure 2.6. A typical schematic diagram of the Hall bar geometry. A constant current (j_{xx}) is injected along the longest side, the x-axis of the sample. The magnetic field (B) is applied perpendicular to the surface of the sample, i.e. z-axis. The generated longitudinal (V_{XX}) and transverse (V_{xy}) voltages were recorded using a Nanovoltmeter.

The electric field governed by the relation $E = \rho j$, when a mutually perpendicular current (j_{xx}) and magnetic field (B_z) applied to sample, here ρ is the resistivity rank 2 tensor quantity, E and j are the vectors . Hence, in terms of Einstein notation, this relation further can be expressed as $E_i = \rho_{ij} j_{i,}$ where i,j in the subscript represent the component of electrical resistivity, electric field and the current. The matrix representation of this expression can be written as:

$$\begin{pmatrix} E_x \\ E_y \\ E_z \end{pmatrix} = \begin{pmatrix} \rho_{xx} & \rho_{xy} & \rho_{xz} \\ \rho_{yx} & \rho_{yy} & \rho_{yz} \\ \rho_{zx} & \rho_{zy} & \rho_{zz} \end{pmatrix} \begin{pmatrix} j_x \\ j_y \\ j_z \end{pmatrix} \tag{2.1}$$

Now restricting the current flowing into x direction only and eliminating the z component of E, ρ and j, as a result Eqn.2.1 can be rewritten as,

$$\begin{pmatrix} E_x \\ E_y \end{pmatrix} = \begin{pmatrix} \rho_{xx} & \rho_{xy} \\ \rho_{yx} & \rho_{yy} \end{pmatrix} \begin{pmatrix} j_x \\ 0 \end{pmatrix} \tag{2.2}$$

Including the sample dimensions: l (the length between two longitudinal electrical contacts), w (width) and t (thickness) Eqn. 2.2 can be expressed in terms of voltages V_{xx} and V_{xy}:

$$\begin{pmatrix} \frac{V_{xx}}{l} \\ \frac{V_{xy}}{w} \end{pmatrix} = \begin{pmatrix} \rho_{xx} \\ \rho_{yx} \end{pmatrix} \frac{j}{w * t} \tag{2.3}$$

From the above relation, the longitudinal and Hall resistivity can be calculated respectively as:

$$\rho_{xx} = \frac{V_{xx}}{j} * \frac{w * t}{l} \tag{2.4}$$

$$\rho_{yx} = \frac{V_{xy}}{j} * t \tag{2.5}$$

To separate the electrical signal into field-symmetrical (magnetoresistance) and anti-symmetrical (Hall resistivity) components, we need to measure ρ_{xx} and ρ_{yx} in both positive and negative magnetic fields. Thus, the final form of longitudinal and Hall resistivities can be expressed as:

$$\rho_{xx}(B) = \frac{\rho_{xx}(+B) + \rho_{xx}(-B)}{2} \tag{2.6}$$

$$\rho_{yx}(B) = \frac{\rho_{yx}(+B) - \rho_{yx}(-B)}{2} \tag{2.7}$$

2.5.1 Sample preparation

To measure ρ_{xx} and ρ_{yx}, we need a suitable bar- or plate-like shaped single crystal. To this end we cut the bulk single crystals using a wire-saw. The sample attached to a suitable plastic sample holder with GE varnish. In this process, a tungsten wire continuously performs a reciprocating motion against the surface of the sample that is coated with a dripping mixture of glycerin and alumina powder (Al_2O_3). The abrasive particles remove the material and the liquid acts also as a coolant to prevent overheating due to friction between wire/alumina and a sample. After cutting a sample to suitable dimensions, it needs to be properly cleaned before making the electrical contacts. The cleaning process has couple of steps, including washing in acetone (C_3H_6O) to soften the adhesive glue which can then be removed with tweezers. After acetone treatment, the remaining residue is removed by soaking a sample in ethanol (CH_3CH_2OH) bath for 15-20 minutes. Ethanol can dissolve the both polar and nonpolar molecules, can effectively remove the unwanted contaminants those were embedded onto surfaces of the samples. The cleaned sample is then ready to make electrical contacts.

A typical example of Hall bar contacts made on a sample is shown in Figure 2.7. To mount a sample we used an 8 legs puck with a mica flake (that is electrically insulating) as a base. Mica sheet is electrically and thermally insulating, preventing additional unwanted signals during the measurements. A double-sided cellulose tape was placed on top of the mica to gently hold the sample and six electrical connections (two of them used for current and four served as voltage contact) using 25 μm thick gold wires were made. These gold wires were attached to the pin of puck with indium using a soldering-iron. We use indium as a soldering agent as it does not easily dissolve gold, has a low melting point (156.7 °C) and is very ductile. The other ends of the gold wires were attached to the sample with DuPont 4929N silver paint. After making appropriate electrical connections, we ensured that the resistivity is within several Ohms range.

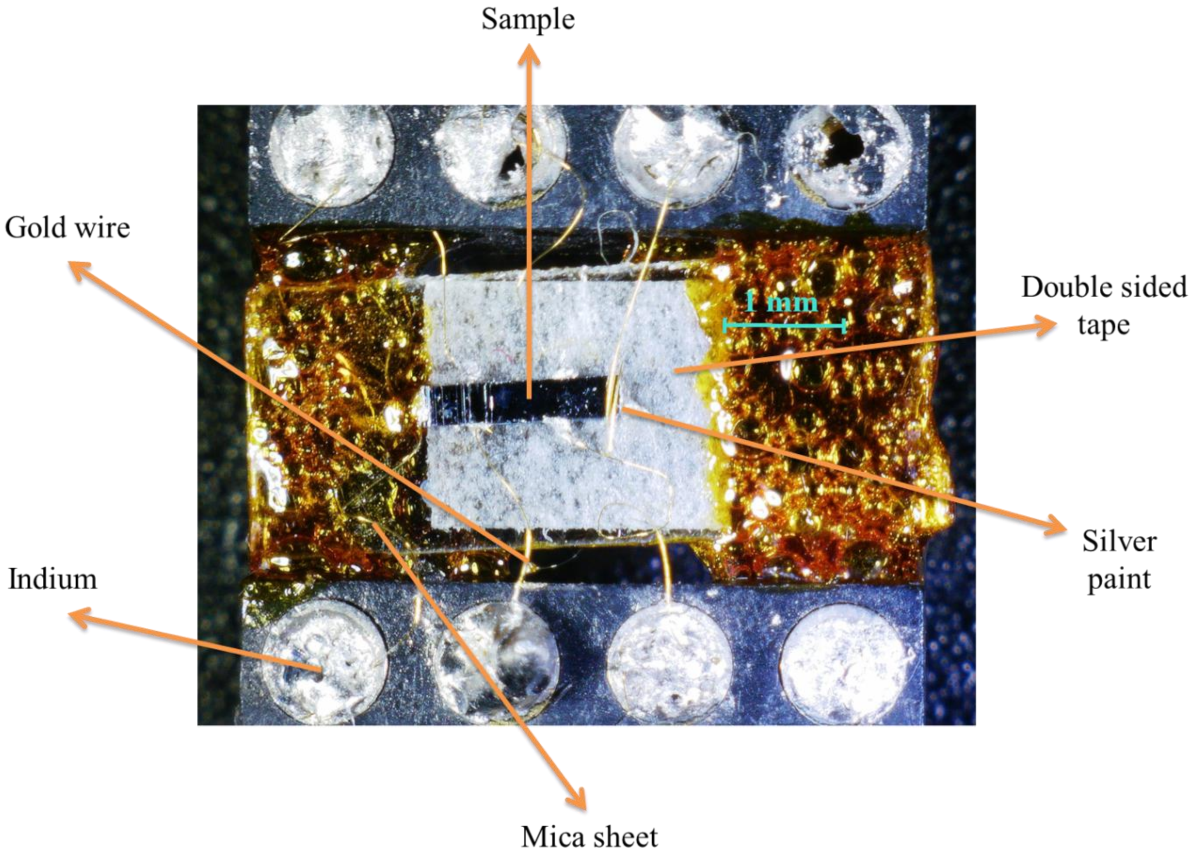

Figure 2.7. An example of a single crystalline sample prepared for the electrical measurements.

2.5.2 Measurements

Properties of a sample were investigated using a high magnetic field cryostat system, and a schematic representation of the entire magnetoelectric transport system is shown in Figure 2.8. This setup allowed us to measure the electrical properties in the temperature range from 1.7 to 300 K and in the magnetic field up to 14.5 T. The prepared sample was mounted in the electrical probe, which was then inserted into the cryostat system for measurements. The electrical measurements were performed using a four probe method. In this process, the electrical current was injected to the sample through a Keithley 6221 current source, the voltages were determined using Keithley 2182A nanovoltmeter and the sample temperature were recorded with a Lakeshore 332 temperature controller. The temperature of the VTI base was varied with a heating element controlled by another Lakeshore 332 temperature controller. MR and Hall measurements were done simultaneously in the presence of a magnetic field at several temperatures in between 1.7 to 300 K. The magnet was powered by a power supply IPS 120, which can provide a bipolar current of -97 A $\leq j \leq$ +97 A, leading to generation of a magnetic field of -14.5 T $\leq B \leq$ 14.5 T. This power supply can also operate the magnet in either non-persistent or persistent mode. The latter was used to acquire data on temperature sweeps at a constant magnetic field. All the instruments were interfaced with Labview to PC to control condition of the experiment and to collect the data.

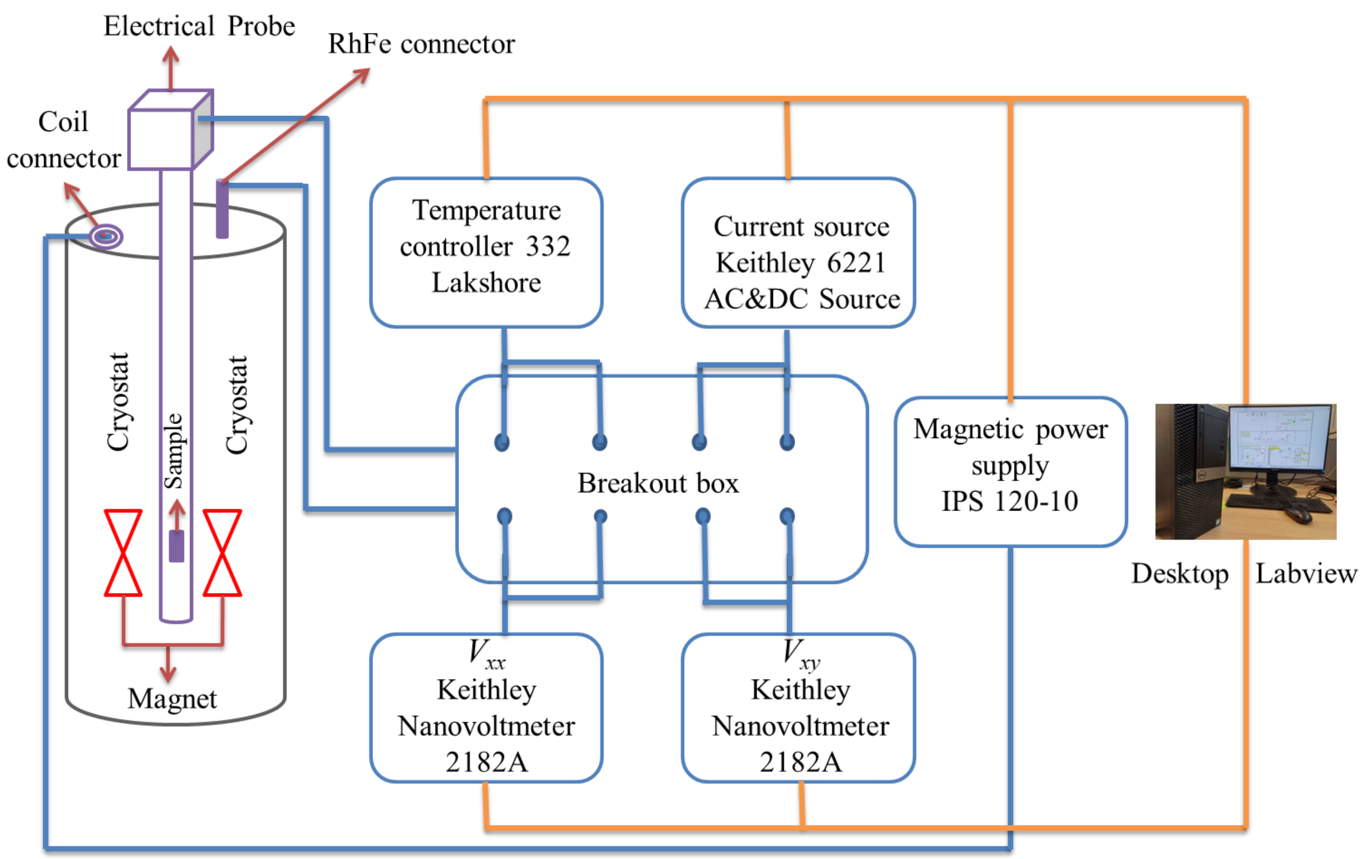

Figure 2.8. Schematic diagram of the magnetoelectric measurement setup. Blue lines denote electrical connections, orange ones denote data transfer.

2.6 Thermoelectrical transport measurements

The thermoelectric measurements can be seen as a relative of electrical transport measurements – they probe the same electronic system and the relevant coefficients are linked, for example through the Mott relation (discussed in detail in chapter 1). However, the former are often more sensitive to details of the electronic structure. The schematic diagram of the experimental setup for measurements of the thermoelectric power and Nernst effect is shown in Figure 2.9. The application of thermal gradient ($\nabla_x T$) to a sample causes charge particles to drift the from the hot end ($T+\Delta T$) to cold end (T), resulting in thermoelectrical current. As we carried out measurements in an open circuit configuration, this drift is offset by the appearance of the electric field, which is effectively measured as the voltage (V) across the sample. The thermopower (S) is defined as the ratio of developed longitudinal voltages (V_x) to the temperature difference ($\Delta_x T$) :

$$S_{xx} = \frac{V_x}{\Delta_x T} \tag{2.8}$$

Subjecting of a sample to a mutually perpendicular thermal gradient and magnetic field (B_z), results in development of a transverse voltages perpendicular to both $\nabla_x T$ and B_z. The phenomenon is called the Nernst effect and the Nernst signal is denoted by S_{xy}:

$$S_{xy} = \frac{V_y}{\Delta_x T} \tag{2.9}$$

During the measurements of the thermoelectric coefficients, it was observed that the data always contained mixed contributions from longitudinal to transverse signals due to the asymmetric position of the contacts. Therefore, for the magnetic field dependences it was necessary to symmetrize the thermopower data and anti-symmetrize the Nernst data. The results can be presented in the following form:

$$S_{xx}(B) = \frac{S_{xx}(+B) + S_{xx}(-B)}{2} \tag{2.10}$$

$$S_{xy}(B) = \frac{S_{xy}(+B) - S_{xy}(-B)}{2} \tag{2.11}$$

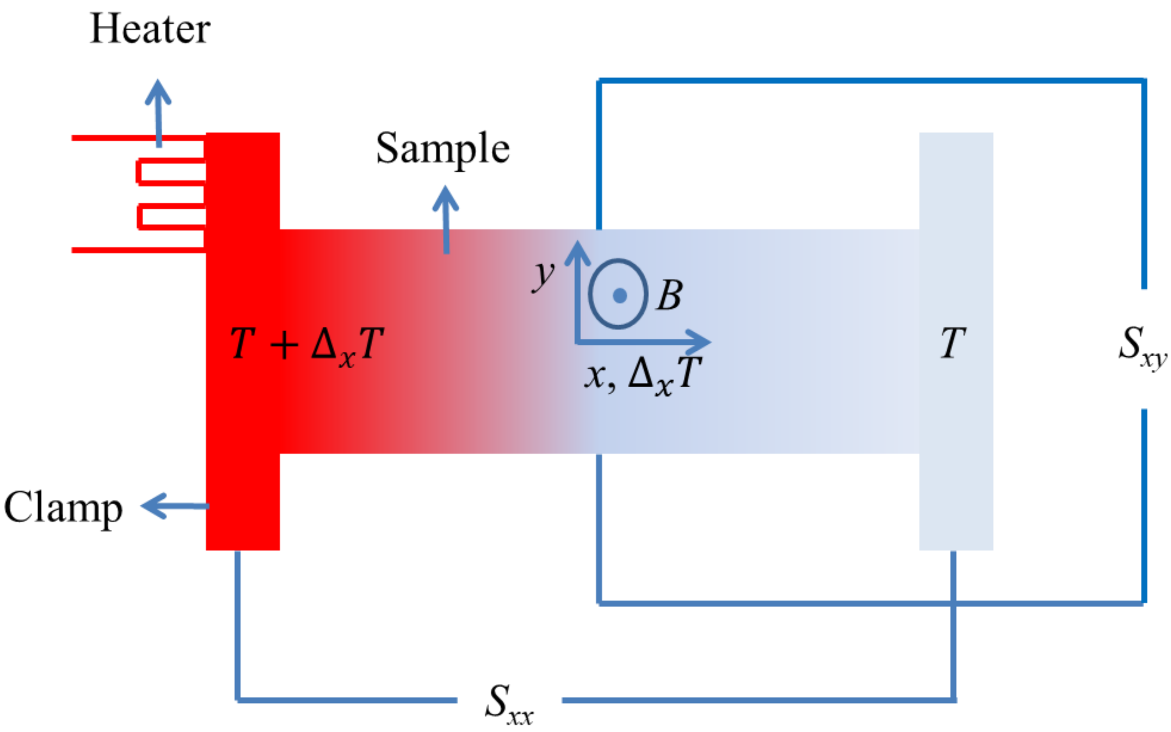

Figure 2.9. A schematic representation thermopower and Nernst effect.

2.6.1 Sample preparation

For thermoelectric measurements, we need a sample with a similar plate shape as for electrical measurements. Actually, in most cases, we performed set of the experiments on the literally same sample. To measure the thermoelectric power the sample was placed between two phosphor bronze clamps that were used as longitudinal voltage contacts. For the Nernst effect measurement, we made two transverse electrical contacts of 25 µm thick gold wires attached to sides of the sample with Dupond 4929N silver paint. Gold wires were fixed to the the surface of the sample through cigarette paper to improve their mechanical stability. Figure

2.10. Illustrates the sample preparation of a Single crystal of $TaAs_2$ to determine its thermoelectric properties.

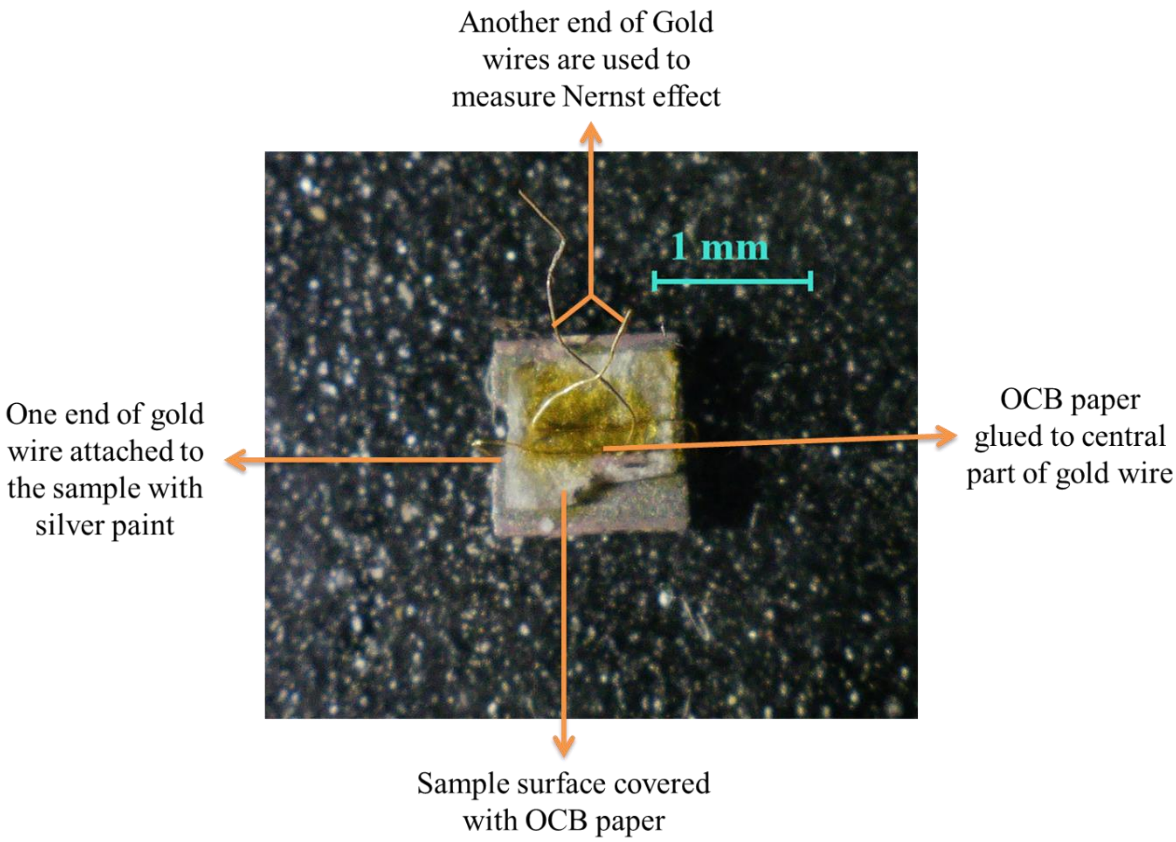

Figure 2.10. A Single crystal of $TaAs_2$ was prepared to determine its thermoelectric properties.

2.6.2 Measurements

The thermoelectric properties were determined using a probe of our own design. The prepared sample was mounted between the phosphor bronze clamps in the thermoelectrical probe. For making proper electrical connection, inevitable void space between sample and clamps was also filled with the silver paints. Other end of the gold wires was connected to the phosphorbronze wires which were already there in the probe to measure the Nernst effect. After assuring that we had proper electrical connections to the sample, the thermoelectric probe was sealed with a vacuum tight brass can. The vacuum port of the probe was connected to the Edwards pumping system, and we evacuated the probe until the pressure inside reached approximately 10^{-6} mbar, and this process takes around 24 hours. However, in order to increase the rate of temperature equalization, we allowed a very small amount of He gas into the internal volume of the probe before the measurement. A schematic diagram of thermoelectric measurements setup Figure 2.11. The thermoelectric probe was then inserted into the VTI for measurements in temperature between 1.7 and 300 K that was controlled using a LakeShore 332. Thermal gradient along the sample was induced using a strain gauge resistive heater excited with current from a Keithley 6221 current source. The temperature of the sample and temperature difference between its ends were determined using two Cernox thermometers glued with Stycast 2850FT to the clamps. Temperatures were recorded using a temperature controller LakeShore 332, while the voltage difference along the sample was detected using Keithley 2182A nanovoltmeter. The magnitude of transverse thermoelectric voltage was usually small, therefore we used EM Electronics A20a DC nanovolt amplifier to amplify the signal, which was then recorded with a Keithley 2182A. We have measured the temperature dependences of thermopower utilizing a heater ON/OFF method, while for field sweeps the heater was always ON. During the measurements of magneto-thermopower and Nernst effect, the superconducting coils were powered by the IPS 120 power supply, allow us to measure the thermoelectric coefficients up to ±14.5 T magnetic field.

The angular variation of the magnetothermal power and the Nernst effect at different temperatures was also measured. The angle between the sample and the magnetic field was varied by changing the position of the sample. This was achieved using a stepper motor connected to a thermoelectric probe controlled by a microprocessor controller. All instruments used in the thermoelectric set-up are connected to LabView for communication and control.

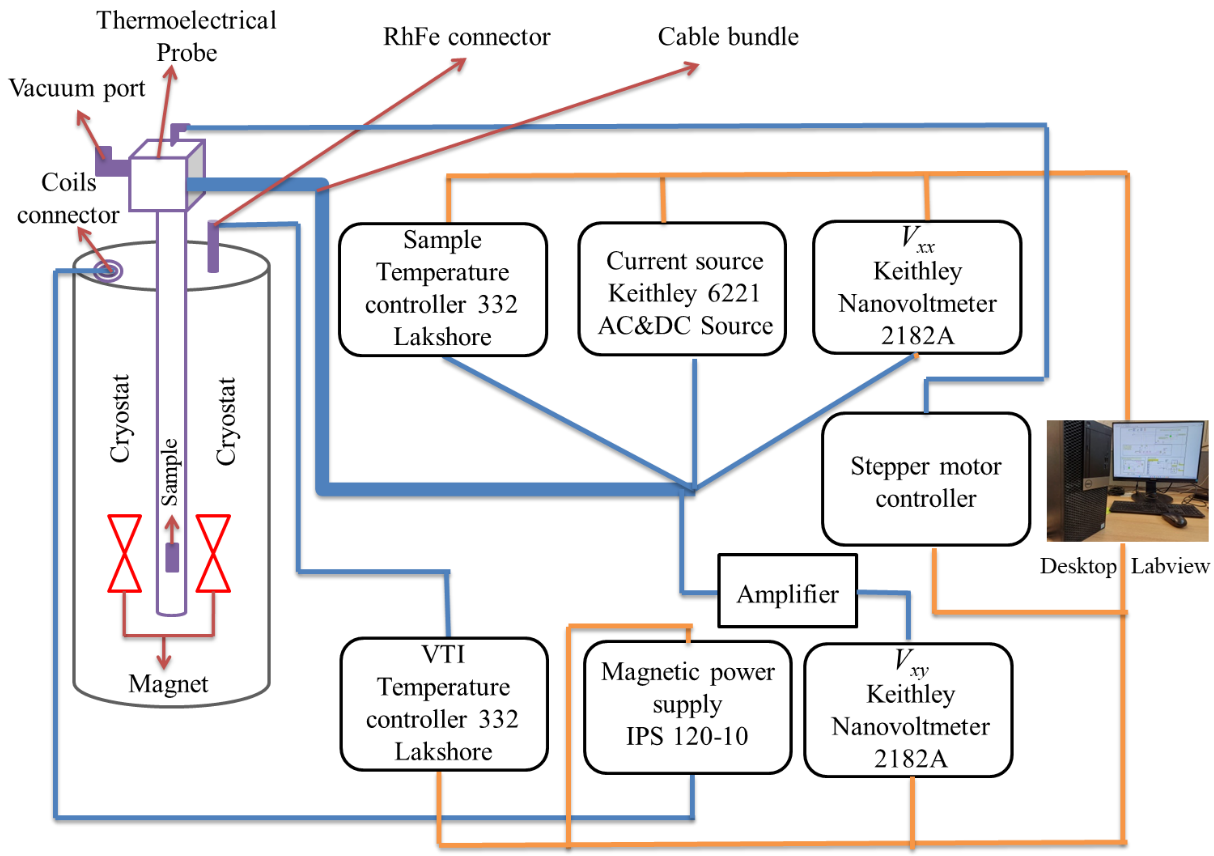

Figure 2.11. A schematic diagram of thermoelectric measurements setup. Blue lines denote electrical connections, orange ones denote data transfer.

2.7 Calibration of TEP

To subtract the back ground signal from leads of the TEP , we have measured the thermopower (*S*) of a high temperature superconductor $EuBa_2Cu_3O_{7-d}$, which has $S = 0$ μV/K up to critical temperature (*Tc*) ~90K. Temperature (*T*) dependences of S_{Leads} is presented in Fig.2.12 (solid blue circles). Back ground signal from the wires was small and linearly increases above *T* ~60K. For higher temperature, above $T>T_c$ the signal was linearly extrapolated to the room temperature. Than we can subtract this from the raw data to get actual *S* of a sample. Otherwise you will have a mixture of a sample and wires signals together.

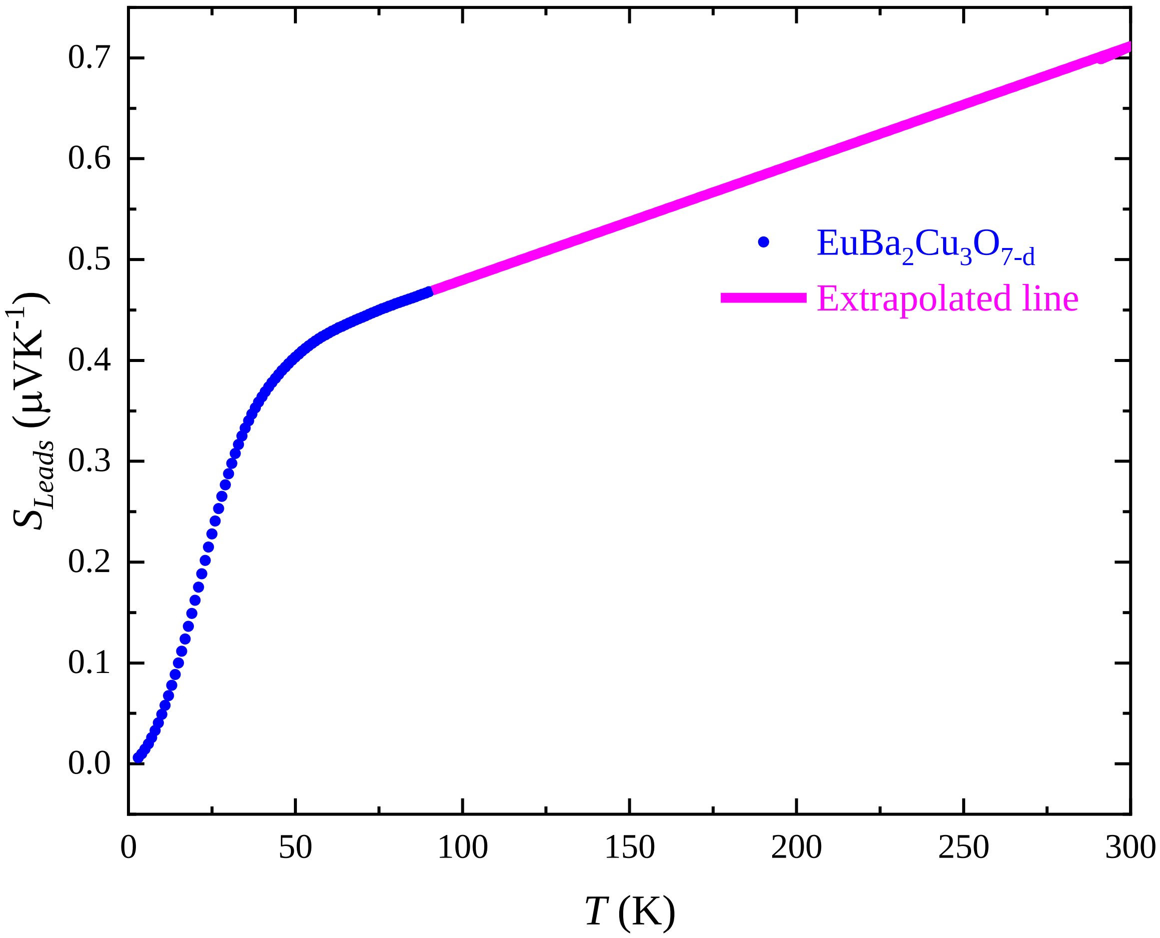

Figure 2.12. Temperature dependences of thermoelectric power of Leads of TEP.

CHAPTER 3

ARTICLES COMPRISING THE THESIS

3.1 A brief summary of the main results

In this PhD thesis, my aim was to explore the attributes of topological semimetals by studying their electrical and thermoelectric properties. This choice is motivated by the fact that the non-trivial electron structure is readily manifested by unconventional transport effects. In particular, thermoelectric coefficients show a profound response, providing a valuable source of information about an electronic system.

In the first project, we have studied the magnetoelectrical and magnetothermoelectrical transport properties of the topological semimetal $TaAs_2$. This work involved the analysis of the prominent quantum oscillations observed at low temperatures in the resistivity as well as Hall, Seebeck, and Nernst coefficients. We noticed that of the amplitude the fundamental frequency shows an unusual temperature evolution when compared to its second harmonic. The effect of suppressing the fundamental oscillation while enhancing its second harmonic has turned out to be a consequence of Zeeman splitting and is referred to as the spin-zero effect. Such a phenomenon was previously reported to be caused by changes in the angle at which the magnetic field was applied. However, in our study, we reported the spin-zero effect in $TaAs_2$ to be induced by temperature changes, most likely the temperature evolution of the Lande´ g-factor. We concluded that the temperature evolution of the Lande´ g-factor can reflect changes in the spin-orbit coupling and be related to changes of the topological properties of $TaAs_2$.

In the second project, we have reported anomalous Hall and anomalous Nernst effects arising from the k-space topology of the magnetic Weyl semimetal CeAlSi. In this work, we observed that at low temperature the sign of the anomalous Hall conductivity is positive for the out-of-plane oriented magnetic field and negative for the in-plane magnetic field. Based on the theoretical calculations, we showed that the sign change of the AHC originates from the reconstruction of the band structure under the variation of the spin orientation. To describe properties of the paramagnetic phase, we proposed a single-band toy model assuming a finite Berry curvature around Weyl nodes. This simple model recreates the experimental temperature evolution of AHE and ANE and suggests that the presence of Weyl points near the Fermi level plays a key role in determining the anomalous properties of CeAlSi.

In the third project, we conducted in-field electric and thermoelectric transport measurements in a thin film of the topological Dirac semimetal α-Sn. When the magnetic field was applied along the electrical current or thermal gradient, we observed the negative longitudinal magnetoresistance and negative slope in the magnetic field dependence of the thermopower. This characteristic features of resistivity and thermopower vanish when the magnetic field is deviated from an orientation parallel to the electrical field or the thermal gradient. We showed that the appearances of NLMR and negative slope of the thermopower stems from the charge pumping between Weyl nodes of different chirality. This process diminishes at high temperature as a result of the reduction in the ratio of intervalley scattering time to Drude scattering time.

3.1.1 ARTICLE I: Quantum oscillations

To study the quantum oscillations, we have selected a single crystal of $TaAs_2$, which belongs to the MPn_2 class, where M represents the transition metal and Pn stands for the pnictide. The electronic structure of the MnP_2 family has recently been comprehensively investigated and shown to consist of a number of trivial pockets together with those described by non-trivial weak topological indices [103,104]. Among the MnP_2 compounds, $TaAs_2$, which crystallizes in a centrosymmetric monoclinic structure, has attracted considerable attention. This could be induced by observed at low temperatures unusual transport properties, such as ultra-high mobility and extremely large magnetoresistance (XMR) [105]. Furthermore, it was postulated that application of a magnetic field induces Weyl points in $TaAs_2$ [94]. The associated Zeeman effect can also generate a non-zero Berry curvature, which will translate into an additional phase of the electron wave functions. This, in turn, can alter the conditions necessary for occurrence of the destructive interference of quantum oscillations, which is referred to as the spin-zero effect [95]. We have observed this phenomenon in measurements of the electrical and thermo-electrical transport properties of $TaAs_2$ single crystal with applied magnetic field along [-210] crystallographic direction. In the Nernst signal, we detected two fundamental frequencies $f_{\nu\alpha} \sim 105$ T and $f_{\nu\beta} \sim 221$ T and a second harmonic of $f_{\nu\beta}$. Analogous to the Nernst oscillations, the fast Fourier transform of Shubnikov–de Haas oscillations also gave us two fundamental frequencies $f_{\rho\alpha} \sim 122$ T and $f_{\rho\beta} \sim 210$ T as well as a second harmonic $2f_{\rho\beta} \sim 420$ of the latter. Although, the signal to noise ratio was higher for the former. Remarkably, the amplitude ratio of the fundamental β frequency and its second harmonic evolves in unusual way with temperatures, indicating the spin-zero effect at $T \approx 25$ K. In addition, we observed that the phase of Nernst oscillations at $T = 35$ K is opposite to one detected at $T = 11.2$ K, which provides additional compelling evidence that the phenomenon is indeed caused by temperature changes rather than the angle at which the magnetic field was applied. A plausible source of the spin-zero effect in $TaAs_2$ is the Lande´ g-factor showing significant temperature dependence. Further, a possible reason for the temperature dependent Lande´ g-factor is the evolution of the spin-orbit coupling, which can influence the topological properties of $TaAs_2$.

Journal of Physics and Chemistry of Solids 170 (2022) 110939

Contents lists available at ScienceDirect

Journal of Physics and Chemistry of Solids

journal homepage: www.elsevier.com/locate/jpcs

Temperature-driven spin-zero effect in $TaAs_2$

Md. Shahin Alam [a], P.K. Tanwar [a], Krzysztof Dybko [a,b], Ashutosh S. Wadge [a], Przemysław Iwanowski [a,b], Andrzej Wiśniewski [a,b], Marcin Matusiak [a,c,*]

[a] International Research Centre MagTop, Institute of Physics, Polish Academy of Sciences, Aleja Lotników 32/46, PL-02668, Warsaw, Poland
[b] Institute of Physics, Polish Academy of Sciences, Aleja Lotników 32/46, PL-02668, Warsaw, Poland
[c] Institute of Low Temperature and Structure Research, Polish Academy of Sciences, ul. Okólna 2, 50-422, Wrocław, Poland

ARTICLE INFO

Keywords:
Topological semimetals
Nernst effect
Quantum oscillations
Spin-zero effect

ABSTRACT

The electrical and thermo-electrical transport properties of the semimetal $TaAs_2$ have been measured in a magnetic field applied along the [−2 0 1] direction. The resulting field dependences of the resistivity as well as the Hall, Seebeck, and Nernst coefficients below $T \approx 100$ K can be satisfactorily described within the two-band model consisting of electron and hole pockets. At low temperature, all of the measured coefficients exhibit significant contributions from quantum oscillations. The fast Fourier-transform (FFT) of the oscillatory Nernst signal shows two fundamental frequencies, $F_\alpha = 105$ T and $F_\beta = 221$ T, and the second harmonic of the latter ($F_{2\beta} = 442$ T). The ratio between the FFT amplitudes of F_β and $F_{2\beta}$ changes with temperature in an unusual way, indicating the observation of a spin-zero effect caused by temperature change. This is likely related to the substantial temperature dependence of the Landé g-factor, which in turn may stem from the non-parabolic energy dispersion or temperature evolution of the spin-orbit coupling.

1. Introduction

The realization of the role that topological structure plays in determining the macroscopic properties of a system led to one of the biggest breakthroughs in modern solid-state physics [1–3]. Subsequent research activity resulted in the discovery of a large variety of different types of topologically non-trivial phases [4–16]. $TaAs_2$ is an interesting topological semimetal [17,18] that has been suggested to possess a trivial strong topological index along with three non-trivial weak indices [19]. Strong and weak surface states are, for example, immune or sensitive to disorder, respectively [20]. It is also envisaged that the Zeeman effect in $TaAs_2$ induces additional Berry curvature, which would make it a type-II Weyl topological semimetal in a magnetic field [21] or change the electronic structure from trivial to non-trivial (and vice versa) depending on the specific directions of the magnetic field [22].

In this work, we have investigated the magneto-thermo-electrical properties of $TaAs_2$ below $T \approx 100$ K. The field dependences of the transport coefficients in this range can be satisfactorily modelled by a semi-classical multi-band approach, but in relation to the Nernst effect we observe an unusual temperature evolution of quantum oscillations. Specifically, the relationship between amplitudes of the 221 T fundamental frequency and its second harmonic indicates occurrence of a spin-zero effect in $TaAs_2$. Remarkably, the phenomenon arises as a result of changes in temperature, and is not due to the angle at which the magnetic field is applied. This opens the possibility that topological attributes of $TaAs_2$ are temperature-dependent.

2. Material and methods

Single crystals of $TaAs_2$ were grown by two-stage chemical vapour transport. Polycrystalline $TaAs_2$ was synthesized by direct reaction of Ta foil (ZR Industrial Ltd., 99.99%) and As (PPM Pure Metals, 99.999995%). The reactants were placed inside an evacuated quartz tube at 990 °C for 19 days. After the synthesis, polycrystalline $TaAs_2$ was pressed into pellets, which were loaded into a quartz tube with iodine (POCH, 99.8%). The tube was then sealed under vacuum and placed in a gradient zone of temperature 1025 °C (crystallization zone) and 956 °C (source zone) for 23 days. Thereafter, the furnace was cooled to room temperature at 100 °C/h. X-ray powder diffraction analysis confirmed the monoclinic unit cell and $C2/m$ (No. 12) space group of the studied crystals. Surface quality and quantitative chemical composition were verified using a Bruker QUANTAX 400 energy-dispersive X-ray

* Corresponding author. International Research Centre MagTop, Institute of Physics, Polish Academy of Sciences, Aleja Lotników 32/46, PL-02668, Warsaw, Poland.

E-mail address: matusiak@magtop.ifpan.edu.pl (M. Matusiak).

https://doi.org/10.1016/j.jpcs.2022.110939
Received 22 February 2022; Received in revised form 27 July 2022; Accepted 28 July 2022
Available online 5 August 2022

spectroscopy (EDX) system coupled with a Zeiss Auriga field-emission (Schottky-type) scanning electron microscope (FESEM) [23].

For transport measurements, a single crystal was cut to a plate of dimensions 1.7 × 1.3 × 0.3 mm^3. The crystallographic *b*-axis was oriented along the longest side of the sample and electrical and thermal currents were applied along this [0 1 0] direction. The magnetic field was applied perpendicularly to the naturally occurring (−2 0 1) plane.

For resistivity measurements, the electrical contacts were arranged in the Hall bar geometry. During Seebeck (S_{xx}) and Nernst (S_{xy}) signal measurements, the sample was clamped between two phosphor bronze blocks, to which two Cernox thermometers and resistive heaters were attached. Magnetic field sweeps were performed in magnetic fields from −14.5 to +14.5 T in order to extract the voltage components, which were odd and even in *B*. For temperature ramps in $B = 0$ T, the "heater on-off" method was used, whereas for the field sweeps, the heater was permanently turned on. The temperatures were measured with Cernox thermometers that were supposed to exhibit minimal magnetoresistance. In the range over which they were used (i.e., above $T = 5$ K and up to $B = 14.5$ T), the relative error related to the magnetic field influence was expected to be smaller than ca. 2% [24,25].

3. Results

Exemplary field dependences of the electrical resistivity (ρ_{xx}) and

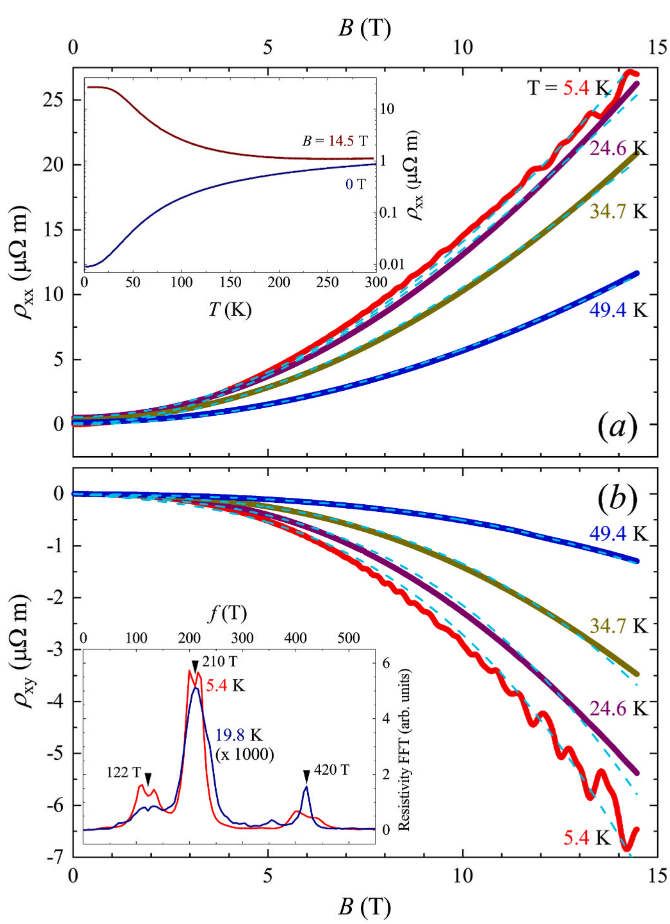

Fig. 1. (Color online) Magnetic field dependence of the longitudinal resistivity (panel *a*) and Hall resistivity (panel *b*) at various temperatures with current direction parallel to [0 1 0] and ***B*** parallel to [−2 0 1]. The dashed lines in both panels show fits prepared within the semi-classical two-band model (Eq. (1) and (2)).
The inset in panel *a* presents the temperature dependences of ρ_{xx} at 0 T and a magnetic field of 14.5 T; the inset in panel *b* shows the fast Fourier-transform spectra of ρ_{xx} at 5.4 K (red) and 19.8 K (blue).

Hall resistivity (ρ_{xy}) for $TaAs_2$ are presented in Fig. 1. These are the results of symmetrisation and anti-symmetrisation of the data collected for positive and negative magnetic fields. The temperature dependence of ρ_{xx} is shown in the inset of Fig. 1a. The value of the residual resistivity ratio (RRR $= \rho_{xx}(300\ \text{K})/\rho_{xx}(3\ \text{K})$) is about 95, which indicates good quality of the sample, and is comparable with previously reported values (RRR ≈ 85 [26], 100 [18], 120 [27]). One of the hallmarks of $TaAs_2$ is its extremely large and non-saturating magnetoresistance [18,19,26–29]. In the present case, ρ_{xx} in the low-temperature limit increases almost 35 000-fold between $B = 0$ and 14.5 T. Such a large magnetoresistance could be a consequence of the fact that $TaAs_2$ appears to be a nearly compensated semimetal, in agreement with density functional theory calculations [17]; alternatively, this might also stem from its non-trivial topology [19,22].

The slopes of the Hall resistivity dependences, presented in Fig. 1b, exhibit a similar strong dependence on the magnetic field, i.e. ρ_{xy}/B is very small at low field, but becomes large and negative at high field, which suggests a dominant role of electrons at high field. For example, at $T = 1.7$ K, calculated from the linear fit in the range $0.035\ \text{T} < B < 0.5\ \text{T}$, $\rho_{xy}/B \approx -6 \pm 2 \times 10^{-9}$ Ωm/T (= m^3/C) and $\rho_{xy}/B \approx -4.5 \times 10^{-7}$ m^3/C for $B = 14.5$ T.

The $\rho_{xx}(B)$ and $\rho_{xy}(B)$ dependences can be reasonably well modelled using a semi-classical two-band approximation [30]:

$$\rho_{xx}(B) = \frac{1}{e}\frac{(n_e\mu_e + n_h\mu_h) + (n_h\mu_e + n_e\mu_h)\mu_e\mu_h B^2}{(n_e\mu_e + n_h\mu_h)^2 + [(n_h - n_e)\mu_e\mu_h]^2 B^2} \tag{1}$$

$$\rho_{xy}(B) = \frac{B}{e}\frac{(n_h\mu_h^2 - n_e\mu_e^2) + (n_h - n_e)\mu_e^2\mu_h^2 B^2}{(n_e\mu_e + n_h\mu_h)^2 + [(n_h - n_e)\mu_e\mu_h]^2 B^2} \tag{2}$$

where *n* is concentration, *μ* is mobility, *e* is the elementary charge, and the *e* and *h* indices denote the electron and hole contributions, respectively. Fits of both $\rho_{xx}(B)$ and $\rho_{xy}(B)$ for a given temperature were performed simultaneously, and the results are shown in Fig. 1. In the low-temperature limit, they give concentrations of both electrons and holes of around 10^{25} m^{-3} ($n_e = 1.1 \times 10^{25}$ m^{-3} and $n_h = 1.0 \times 10^{25}$ m^{-3} at $T = 1.7$ K, respectively) and mobilities of around 0.5 m^2/Vs ($\mu_e = 0.52$ m^2/Vs and $\mu_h = 0.45$ m^2/Vs at $T = 1.7$ K). These are of the same order of magnitude as previously reported values [23].

At low temperature and high field, both ρ_{xx} and ρ_{xy} exhibit strong oscillatory components as a result of the Landau level quantization. The inset in Fig. 1b presents exemplary ($T = 5.4$ and 19.8 K) fast Fourier-transforms (FFT) of the resistivity calculated for the field range 8–14.4 T with a subtracted background in the form of a third-order polynomial. For the unevenly sampled signal, we used an algorithm based on the Lomb normalized periodogram. We were able to confirm the presence of two fundamental oscillations: $F_{\rho\alpha} = 122$ T, $F_{\rho\beta} = 210$ T, and the second harmonic of the latter, $F_{2\rho\beta} = 420$ T. At $T = 5.4$ K, we observed double-peak structures that might be due to additional orbits present in the irregularly shaped electron/hole pockets [17]. Similar behaviour has been reported, for instance, for NbP [31] or, due to a small misalignment of the magnetic field, in Sb [32,33].

Analogously to $\rho_{xx}(B)$ and $\rho_{xy}(B)$, the Seebeck (Fig. 2a) and Nernst (Fig. 2b) signals also show strong dependence on the magnetic field. The absolute value of S_{xy} at $B = 14.5$ T shows some non-monotonic temperature dependence, which would be removed if it were divided by temperature to account for entropy changes. The data can be fitted with the conventional semi-classical equations [34,35]:

$$S_{xx}(B) = S_{xx}^0 \frac{1}{1 + (\mu B)^2} + S_{xx}^{\infty} \frac{(\mu B)^2}{1 + (\mu B)^2} \tag{3}$$

$$S_{xy}(B) = S_{xy}^0 \frac{\mu B}{1 + (\mu B)^2} \tag{4}$$

where S_{xx}^0 and S_{xx}^{∞} are the values of the thermoelectric power at the limits

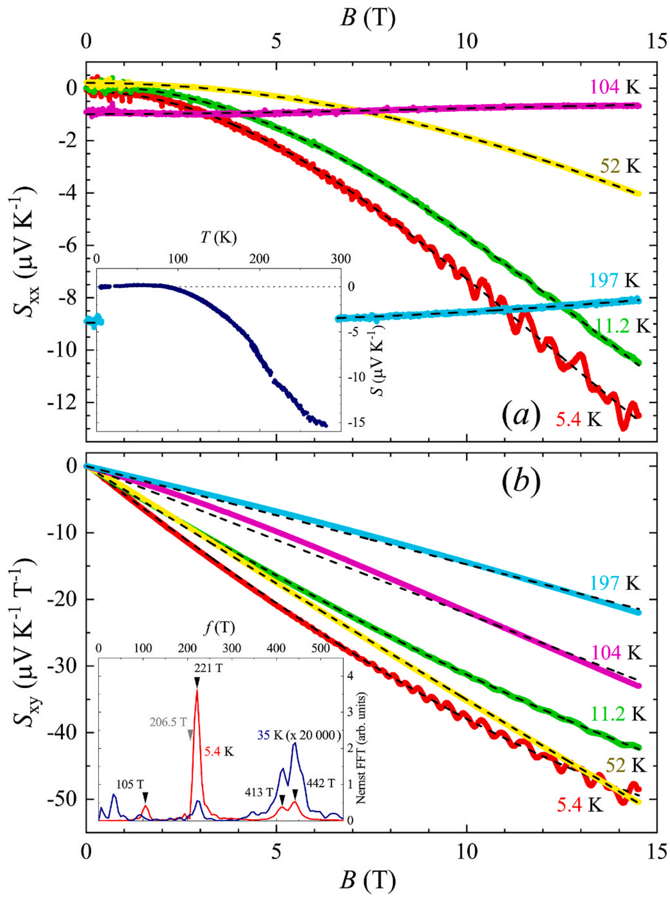

Fig. 2. (Color online) Magnetic field dependences of the thermoelectric power (panel *a*) and Nernst coefficient (panel *b*) at various temperatures. The dashed lines in both panels show fits prepared using Eqs. (3) and (4).
The inset in panel *a* presents the temperature dependence of the Seebeck coefficient at zero magnetic field; the inset in panel *b* shows FFT spectra of the Nernst coefficient at 5.4 K (red) and 35 K (blue).

of zero and infinite field, respectively, S_{xy}^0 is the amplitude of the Nernst signal at the zero-field limit, and $\mu = \sqrt{\mu_e \mu_h}$ is the mean mobility [30]. There are some deviations of the fitting lines from the actual data for the Nernst signal above $T \approx 50$ K, but overall $S_{xx}(B)$ and $S_{xy}(B)$ can be well approximated using Eqs. (3) and (4). However, the resulting μ values are about an order of magnitude smaller than those deduced from electrical transport measurements (even though they are consistent between $S_{xx}(B)$ and $S_{xy}(B)$). We conclude that although Eqs. (3) and (4), which were formulated for a single-band conductor [34], can satisfactorily reproduce the field dependence of the thermoelectrical coefficients in a multiband semimetal, the resulting mobilities are not the best approximation of the actual values. This is probably due to incomplete compensation of electron and hole carrier densities in $TaAs_2$ (at $T = 1.7$ K, the electrical conductivity of electrons in $TaAs_2$ is about 27% higher than that of holes).

Multiband character of $TaAs_2$ may also explain the field dependence of the thermoelectric power, which similarly to ρ_{xy}/B is very small when $B \to 0$ T at $T = 5.4$ K, and becomes substantially negative in a field, reaching $S_{xx}(14.5\ \mathrm{T}) \approx -12$ μV/K. The inset in Fig. 2a, showing the temperature dependence of S_{xx} in zero magnetic field, indicates that almost perfect compensation of S_{xx} in zero field occurs below $T \approx 80$ K. At low temperature and high magnetic field, a large oscillatory component appears in both $S_{xx}(B)$ and $S_{xy}(B)$. The inset in Fig. 2b presents the FFT of the latter at two temperatures: $T = 5.4$ and 35 K (which were calculated for the field range 8–14.5 T with a subtracted third-order polynomial as a background). Here, again, two fundamental frequencies are present: $F_{\nu\alpha} = 105$ T, $F_{\nu\beta} = 221$ T. They are slightly different from those estimated on the basis of the Shubnikov–de Haas effect, most likely due to small misalignment of the crystal with respect to the magnetic field in two separate experiments. Here, we observed the second harmonic of the β oscillations, $F_{2\nu\beta} = 442$ T, which in the FFT is accompanied by a somewhat smaller peak at $F_{2\nu\beta}' = 413$ T. We believe this to be the second harmonic of the twin β peak at $F_{\nu\beta}' = 206.5$ T. With our resolution, we are not able to distinguish it from the larger $F_{\nu\beta} = 221$ T, but we notice a beating pattern in the oscillatory signal of the β band filtered out from other frequencies (see Fig. S4 in the Supplementary Material (SM)). This indicates the presence of two close frequencies. We envisage that this is a consequence of the aforementioned shift in angle, which for an irregular electron/hole pocket (like those present in the calculated electronic structure of $TaAs_2$ [17]) can create another extremal Fermi surface area. As a general note, we would like to point out that the signal-to-noise ratio for the Nernst data was the best among the measured quantities, thus we focus mainly on analysing these results.

4. Discussion

The most striking result of our work is presented in Fig. 3, in which the oscillatory components of the Nernst signal at two different temperatures are compared. Thus, it turns out that the dominant $F_{\nu\beta}$ at $T = 11.2$ K is almost entirely replaced by its second harmonic, $F_{2\nu\beta}$, at $T = 24.6$ K. In regular metals, the higher harmonics of the quantum oscillations disappear faster with temperature than the fundamental frequency. The amplitude of the p-th harmonic of the oscillations is reduced by the factor $R_T = \frac{\lambda p T}{\sinh(\lambda p T)}$ [36], where $\lambda = \frac{2\pi^2 k_B m^*}{e\hbar B}$ (k_B, m^*, and $\hbar$ denote the Boltzmann constant, the effective mass, and the reduced Planck constant, respectively). The upper inset in Fig. 4 shows changes in the relative amplitudes of the first and second harmonics of the β oscillations at three representative temperatures. At high temperature, the amplitude of $F_{\nu\beta}$ is largely suppressed, while $F_{2\nu\beta}$ is clearly visible and the reduction factor in this region is anomalously small (i.e., smaller than 1). The ratio of the amplitudes of the first and second harmonics, A_1^ν/A_2^ν, is 0.13 at $T = 24.5$ K, whereas at $T = 34.7$ K it increases slightly ($A_1^\nu/A_2^\nu = 0.28$), possibly deviating from zero at a temperature between 24.5 and 34.7 K. In Fig. 4, we present the entire temperature dependence of A_1^ν/A_2^ν calculated from the Nernst signal, which seems to be confirmed by A_1^ρ/A_2^ρ (T) deduced from the resistivity shown in the lower inset of the same figure (separated temperature dependences of amplitudes are shown in Figs. S2 and S3 in the SM). In the latter case, the signal-to-noise ratio is somewhat lower than that based on the Nernst effect, but the overall appearance of A_1/A_2 remains similar to that in the main panel of

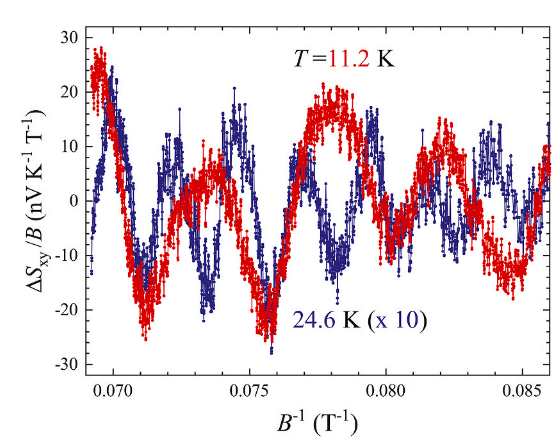

Fig. 3. Comparison of the oscillatory component of the Nernst signal in $TaAs_2$ plotted versus inverse magnetic field at $T = 11.2$ K and 24.6 K. The results for the latter are multiplied by a factor of 10.

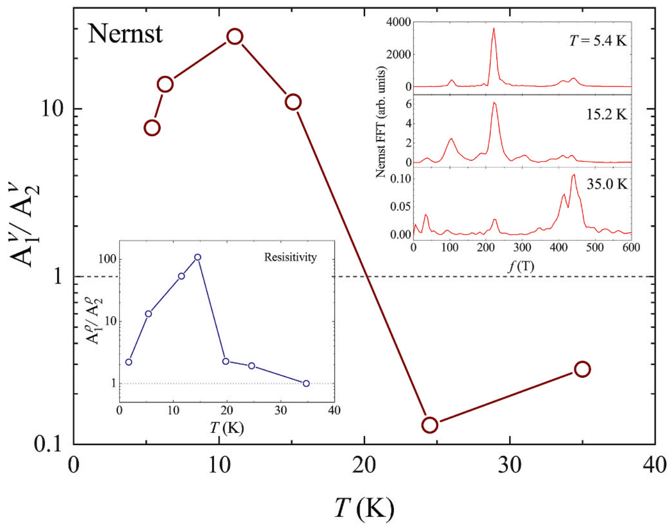

Fig. 4. (Color online) Temperature dependence of the first to second harmonic ratio for the β band calculated from the Nernst signal. The upper inset shows the evolution of the Nernst FFT spectrum around the β frequency and its second harmonic at $T = 5.4$ K, 15.2 K, and 35 K. The lower inset presents the analogous amplitude ratio as the main panel, but estimated from the resistivity data.

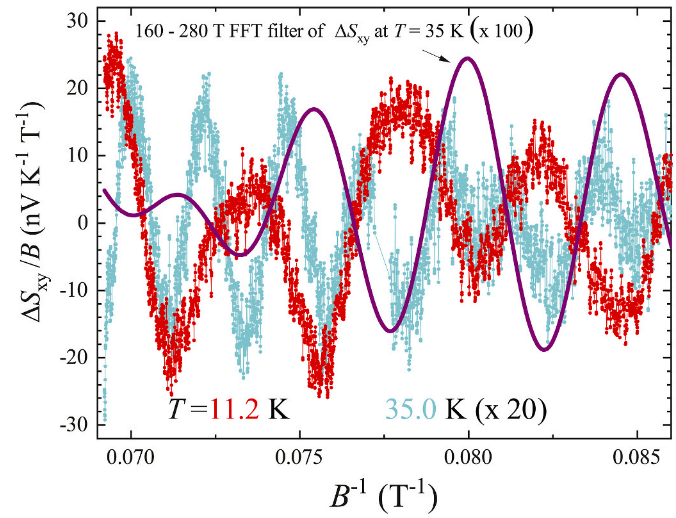

Fig. 5. Comparison of the oscillatory component of the Nernst signal plotted versus inverse magnetic field at $T = 11.2$ K and 35 K. The latter is multiplied by a factor of 20. The solid line depicts the signal at $T = 35$ K filtered with an FFT band-pass filter for the 160–280 T frequency range, which turns out to be in antiphase with the fundamental β oscillation below $T \approx 25$ K.

Fig. 4.

The effect of suppressing the fundamental amplitude with enhancement of the second harmonic is a consequence of Zeeman splitting and is called the spin-zero effect [36]. This happens when:

$$\cos\left(\frac{\pi}{2} g \frac{m^*}{m_e}\right) = 0 \tag{5}$$

and hence $g = (2r + 1)/\frac{m^*}{m_e}$, where r is any integer and g is the Landé g-factor.

The spin-zero effect is normally observed when the condition described by Eq. (5) is met for a particular orientation of applied magnetic field. Its occurrence has been reported in regular metals such as copper [37,38] and gold and silver [39]. Recently, such a phenomenon was also observed in the Weyl semimetal WTe_2 [40] and the Dirac semimetal $ZrTe_5$ [41]. Despite the relativistic energy dispersion in these topological materials, the same Eq. (5) must be satisfied for the spin-zero effect to occur [41]. However, it was shown that additional Zeeman-induced Berry curvature shifts the spin-zero angle in $ZrTe_5$ [22]. Remarkably, S. Sun et al. [22] predicted that the spin-zero effect is also expected to occur in $TaAs_2$ and that it should be affected by the Berry curvature similarly as in $ZrTe_5$. In fact, the angular dependence of the Shubnikov–de Haas effect at $T = 1.6$ K shows that the fundamental frequency amplitude of β oscillations almost vanishes in a field applied at around 30° with respect to [−2 0 1] [23].

Since the spin-zero effect emerges due to the phase shift between the oscillations coming from the spin-up and spin-down electrons, it can be expected that the phase of the fundamental frequency will be inverted at the spin-zero condition. In fact, such a phenomenon has been reported at the spin-zero angle in $ZrTe_5$ [22]. Notably, we also observed phase inversion of the β oscillations at around $T = 24.5$ K. Fig. 5 shows a comparison of the Nernst oscillations at temperatures below ($T = 11.2$ K) and above ($T = 35$ K) that of the spin-zero effect, where the β frequency, filtered out of the latter, appears to be in antiphase with the β oscillation at low temperature.

We would like to stress that our discovery of the spin-zero effect in $TaAs_2$ is unusual in terms of the condition that triggers the phenomenon. That is to say, it is not caused by a change in angle, but by a change in temperature. As indicated by Eq. (5), this can only happen due to a variation in the g-factor or the effective mass. Since the frequencies of the oscillations (and hence the areas of the Fermi surface extremal cross-sections) do not change much with temperature, we believe that T-dependence of the g-factor may be the main cause of the effect in $TaAs_2$.

In order to estimate the g-factor at $T = 5.4$ K, we used the oscillatory part of the Nernst signal presented in Fig. 6, where peaks at $B > 11$ T begin to split due to the Zeeman effect. If the spin degeneracy is lifted, the Landau level index plot should be prepared separately for spin-up and spin-down Landau levels (see the inset in Fig. 6): $n = \frac{F}{B} + \delta + \frac{1}{2}\varphi$, where n is the Landau level index, δ is the phase shift related to the topology and dimensionality of a band, and φ is the phase difference between up ($\varphi = \frac{gm^*}{2m_e}$) and down ($\varphi = -\frac{gm^*}{2m_e}$) spins [42,43]. This procedure gives the g-factor at $T = 5.4$ K equal to $g_0 = 5.8$.

Using the effective mass of the β band, $m^* = 0.35\, m_e$, estimated from the Shubnikov–de Haas effect (see Fig. S5 in the SM), the spin-zero effect can be used to estimate the value of g at temperatures close to 25 K. The values of the g-factor closest to g_0 satisfying Eq. (5) are $g = 2.9$ for $r =$

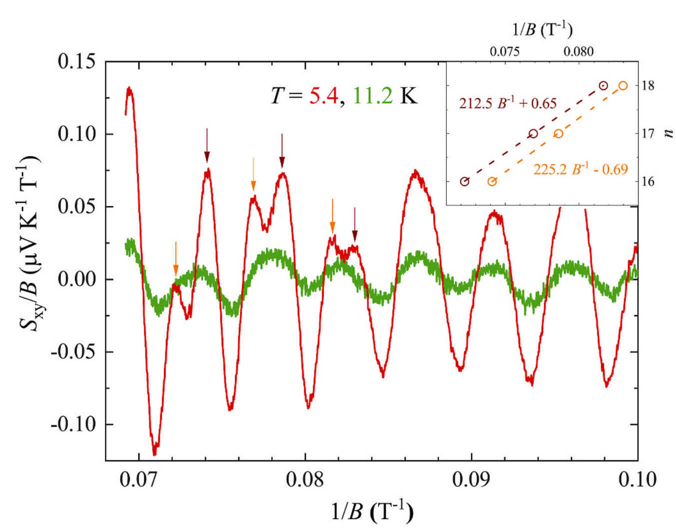

Fig. 6. (Color online) Oscillatory part of the Nernst signal plotted versus B^{-1} at $T = 5.4$ K (at which peaks split at high magnetic field) and 11.2 K (at which no such splitting is evident). The inset presents Landau level fan diagrams at $T = 5.4$ K separated by the Zeeman splitting for the spin-up and spin-down plots.

0 and $g = 8.6$ for $r = 1$. In either case, g at $T \approx 25$ K is significantly different from $g_0 = 5.8$ at $T = 5.4$ K.

Observations of a temperature-dependent g-factor have previously been reported for several semiconductors, such as CdTe and GaAs [44–48]. In the latter, the temperature variation of g was ascribed to the non-parabolicity of the band and evolution of the energy gap [48]. While relative changes of the g-factor in semiconductors are typically rather modest, a significant variation of g with temperature has been reported for the strongly correlated compound $SrIrO_3$ [49]. In this case, temperature-dependent spin-orbit coupling (SOC) was identified as the origin of the phenomenon. In this material, as in the case of the Dirac semimetal Cd_3As_2 [50], the temperature-dependent SOC was suggested to be related to changes in the Rashba coefficient. However, based on the current studies, we are unable to delineate the mechanism responsible for the changes in SOC in $TaAs_2$.

In general, SOC and the Berry phase can be related [51], but the scenario where the g-factor changes due to SOC temperature variation is of particular interest in $TaAs_2$ as the topological attributes of this material are determined by the SOC strength [52]. That is to say, according to calculations based on density functional theory in the absence of SOC, $TaAs_2$ possesses two types of bulk nodal lines. Turning on SOC opens a continuous bandgap in the energy spectrum and renders the system a topological crystalline insulator. In other words, changes of SOC in $TaAs_2$ can affect the topology of the electronic system, and hence open the possibility of the emergence of a temperature-driven topological transition. Whether the evolution of the Seebeck and Nernst signals that we have observed for $TaAs_2$ is somehow related to its topological properties may be an exciting subject for further experimental and theoretical investigations.

5. Conclusions

The temperature dependences of quantum oscillations in the Nernst effect and resistivity indicate that, for a magnetic field parallel to [−2 0 1] and $T \approx 25$ K, we observe the spin-zero effect in $TaAs_2$. The Landé g-factor estimated for this temperature is significantly different from that calculated for $T = 5.4$ K. Among possible origins of the temperature evolution of the g-factor are non-parabolicity of the band, evolution of the energy gap, or changes in the spin-orbit coupling. The latter is of particular interest because in $TaAs_2$ it can lead to modification of the topology of the electronic system.

Author statement

Md Shahin Alam: Software, Investigation, Writing - Original Draft, Writing - Review & Editing.

P.K. Tanwar: Software, Investigation, Writing - Review & Editing.

Krzysztof Dybko: Investigation, Writing - Review & Editing, Ashutosh S. Wadge: Resources.

Przemysław Iwanowski: Resources.

Andrzej Wiśniewski: Resources, Writing - Review & Editing.

Marcin Matusiak: Conceptualization, Methodology, Software, Validation, Investigation, Writing - Original Draft, Writing - Review & Editing, Visualization, Supervision.

Declaration of competing interest

The authors declare that they have no known competing financial interests or personal relationships that could have appeared to influence the work reported in this paper.

Data availability

Data will be made available on request.

Acknowledgments

We would like to thank Carmine Autieri for helpful discussion.

This work was supported by the Foundation for Polish Science through the International Research Agendas (IRA) Programme co-financed by the EU within the Smart Growth Operational Programme (SG OP).

Appendix A. Supplementary data

Supplementary data to this article can be found online at https://doi.org/10.1016/j.jpcs.2022.110939.

References

[1] B. Volkov, O. Pankratov, Two-dimensional massless electrons in an inverted contact, J. Exp. Theor. Phys. Lett. 42 (1985) 178.

[2] O.A. Pankratov, S.V. Pakhomov, B.A. Volkov, *Supersymmetry in heterojunctions: band-inverting Contact on the Basis of $Pb_{1-x}Sn_xTe$ and $Hg_{1-x}Cd_xTe$*, Solid State Commun. 61 (1987) 93, https://doi.org/10.1016/0038-1098 (87)90934-3.

[3] M. König, L.W. Molenkamp, X. Qi, S. Zhang, Quantum spin Hall insulator state in HgTe quantum wells, Science 318 (2007) 766, https://doi.org/10.1126/science.1148047, 80.

[4] L. Fu, Topological crystalline insulators, Phys. Rev. Lett. 106 (2011), 106802, https://doi.org/10.1103/PhysRevLett.106.106802.

[5] P. Dziawa, B.J. Kowalski, K. Dybko, R. Buczko, A. Szczerbakow, M. Szot, E. Łusakowska, T. Balasubramanian, B.M. Wojek, M.H. Berntsen, O. Tjernberg, T. Story, *Topological crystalline insulator States in $Pb_{1-x}Sn_xSe$*, Nat. Mater. 11 (2012) 1023, https://doi.org/10.1038/nmat3449.

[6] A.H. Castro Neto, F. Guinea, N.M.R. Peres, K.S. Novoselov, A.K. Geim, The electronic properties of graphene, Rev. Mod. Phys. 81 (2009) 109, https://doi.org/10.1103/RevModPhys.81.109.

[7] X. Wan, A.M. Turner, A. Vishwanath, S.Y. Savrasov, Topological semimetal and fermi-arc surface states in the electronic structure of pyrochlore iridates, Phys. Rev. B 83 (2011), 205101, https://doi.org/10.1103/PhysRevB.83.205101.

[8] A.A. Burkov, L. Balents, Weyl semimetal in a topological insulator multilayer, Phys. Rev. Lett. 107 (2011), 127205, https://doi.org/10.1103/physrevlett.107.127205.

[9] A.A. Soluyanov, D. Gresch, Z. Wang, Q. Wu, M. Troyer, X. Dai, B.A. Bernevig, Type-II Weyl semimetals, Nature 527 (2015) 495, https://doi.org/10.1038/nature15768.

[10] K. Deng, G. Wan, P. Deng, K. Zhang, S. Ding, E. Wang, M. Yan, H. Huang, H. Zhang, Z. Xu, J. Denlinger, A. Fedorov, H. Yang, W. Duan, H. Yao, Y. Wu, S. Fan, H. Zhang, X. Chen, S. Zhou, *Experimental Observation of topological Fermi Arcs in type-II Weyl semimetal $MoTe_2$*, Nat. Phys. 12 (2016) 1105, https://doi.org/10.1038/nphys3871.

[11] C. Fang, Y. Chen, H.Y. Kee, L. Fu, Topological nodal line semimetals with and without spin-orbital coupling, Phys. Rev. B 92 (2015), https://doi.org/10.1103/PhysRevB.92.081201, 081201(R).

[12] Y. Wu, L.L. Wang, E. Mun, D.D. Johnson, D. Mou, L. Huang, Y. Lee, S.L. Bud'ko, P. C. Canfield, A. Kaminski, *Dirac node Arcs in $PtSn_4$*, Nat. Phys. 12 (2016) 667, https://doi.org/10.1038/nphys3712.

[13] L.M. Schoop, M.N. Ali, C. Straßer, A. Topp, A. Varykhalov, D. Marchenko, V. Duppel, S.S.P. Parkin, B.V. Lotsch, C.R. Ast, Dirac cone protected by non-symmorphic symmetry and three-dimensional Dirac line node in ZrSiS, Nat. Commun. 7 (2016), 11696, https://doi.org/10.1038/ncomms11696.

[14] M. Neupane, I. Belopolski, M.M. Hosen, D.S. Sanchez, R. Sankar, M. Szlawska, S. Y. Xu, K. Dimitri, N. Dhakal, P. Maldonado, P.M. Oppeneer, D. Kaczorowski, F. Chou, M.Z. Hasan, T. Durakiewicz, Observation of topological nodal fermion semimetal phase in ZrSiS, Phys. Rev. B 93 (R) (2016), 201104, https://doi.org/10.1103/PhysRevB.93.201104.

[15] X.Y. Hou, Z. Wang, Y.D. Gu, J.B. He, D. Chen, W.L. Zhu, M. Di Zhang, F. Zhang, Y. F. Xu, S. Zhang, H.X. Yang, Z.A. Ren, H.M. Weng, N. Hao, W.G. Lv, J.P. Hu, G. F. Chen, L. Shan, Superconductivity induced at a point contact on the topological semimetal tungsten carbide, Phys. Rev. B 100 (2019), 235109, https://doi.org/10.1103/PhysRevB.100.235109.

[16] A. Lau, T. Hyart, C. Autieri, A. Chen, D.I. Pikulin, Designing three-dimensional flat bands in nodal-line semimetals, Phys. Rev. X 11 (2021), 031017, https://doi.org/10.1103/PhysRevX.11.031017.

[17] C. Xu, J. Chen, G.X. Zhi, Y. Li, J. Dai, C. Cao, *Electronic Structures of transition metal dipnictides XPn_2 (X = Ta, Nb; pn = P, as, Sb)*, Phys. Rev. B 93 (2016), 195106, https://doi.org/10.1103/PhysRevB.93.195106.

[18] D. Wu, J. Liao, W. Yi, X. Wang, P. Li, H. Weng, Y. Shi, Y. Li, J. Luo, X. Dai, Z. Fang, *Giant semiclassical Magnetoresistance in high mobility $TaAs_2$ semimetal*, Appl. Phys. Lett. 108 (2016), 042105, https://doi.org/10.1063/1.4940924.

[19] Y. Luo, R.D. McDonald, P.F.S. Rosa, B. Scott, N. Wakeham, N.J. Ghimire, E. D. Bauer, J.D. Thompson, F. Ronning, *Anomalous electronic Structure and Magnetoresistance in $TaAs_2$*, Sci. Rep. 6 (2016), 27294, https://doi.org/10.1038/srep27294.

[20] K. Kobayashi, T. Ohtsuki, K.-I. Imura, Disordered weak and strong topological insulators, Phys. Rev. Lett. 110 (2013), 236803, https://doi.org/10.1103/PhysRevLett.110.236803.

[21] D. Gresch, Q. Wu, G.W. Winkler, A.A. Soluyanov, Hidden Weyl points in centrosymmetric paramagnetic metals, New J. Phys. 19 (2017), 035001, https://doi.org/10.1088/1367-2630/aa5de7.
[22] S. Sun, Z. Song, H. Weng, X. Dai, Topological metals induced by the zeeman effect, Phys. Rev. B 101 (2020), 125118, https://doi.org/10.1103/PhysRevB.101.125118.
[23] A.S. Wadge, G. Grabecki, C. Autieri, B.J. Kowalski, P. Iwanowski, G. Cuono, M. F. Islam, C.M. Canali, K. Dybko, A. Hruban, A. Łusakowski, T. Wojciechowski, R. Diduszko, A. Lynnyk, N. Olszowska, M. Rosmus, J. Kołodziej, A. Wiśniewski, *Electronic Properties of $TaAs_2$ topological semimetal Investigated by Transport and ARPES*, J. Phys. Condens. Matter 34 (2022), 12560.
[24] B.L. Brandt, D.W. Liu, L.G. Rubin, Low temperature thermometry in high magnetic fields. VII. Cernox™ sensors to 32 T, Rev. Sci. Instrum. 70 (1999) 104, https://doi.org/10.1063/1.1149549.
[25] M. Süßer, F. Wüchner, Behavior of CERNOX temperature sensors at static magnetic fields up to 15 T, Cryogenics 40 (2000) 413, https://doi.org/10.1016/S0011-2275(00)00055-2.
[26] Y.Y. Wang, Q.H. Yu, P.J. Guo, K. Liu, T.L. Xia, *Resistivity Plateau and extremely large Magnetoresistance in $NbAs_2$ and $TaAs_2$*, Phys. Rev. B 94 (2016), https://doi.org/10.1103/PhysRevB.94.041103, 041103(R).
[27] T.A. Butcher, J. Hornung, T. Förster, M. Uhlarz, J. Klotz, I. Sheikin, J. Wosnitza, D. Kaczorowski, *Fermi surface Investigation of the semimetal $TaAs_2$*, Phys. Rev. B 99 (R) (2019), 245112, https://doi.org/10.1103/PhysRevB.99.245112.
[28] H. Wang, C. Pei, H. Su, Z. Yu, M. Li, W. Xia, X. Liu, Q. Liang, J. Zhao, C. Zhou, N. Yu, X. Wang, Z. Zou, L. Wang, Y. Qi, Y. Guo, *Robust Magnetoresistance in $TaAs_2$ under Pressure up to about 37 GPa*, Appl. Phys. Lett. 115 (2019), 122403, https://doi.org/10.1063/1.5115008.
[29] Z. Yuan, H. Lu, Y. Liu, J. Wang, S. Jia, *Large Magnetoresistance in compensated semimetals $TaAs_2$ and $NbAs_2$*, Phys. Rev. B 93 (2016), 184405, https://doi.org/10.1103/PhysRevB.93.184405.
[30] K.G. Rana, F.K. Dejene, N. Kumar, C.R. Rajamathi, K. Sklarek, C. Felser, S.S. P. Parkin, *Thermopower and unconventional Nernst Effect in the predicted type-II Weyl semimetal WTe_2*, Nano Lett. 18 (2018) 6591, https://doi.org/10.1021/acs.nanolett.8b03212.
[31] J. Klotz, S.-C. Wu, C. Shekhar, Y. Sun, M. Schmidt, M. Nicklas, M. Baenitz, M. Uhlarz, J. Wosnitza, Cl Felser, B. Yan, Quantum oscillations and the Fermi surface topology of the Weyl semimetal NbP, Phys. Rev. B 93 (R) (2016), 121105, https://doi.org/10.1103/PhysRevB.93.121105.
[32] J.R. Long, C.G. Grenier, J.M. Reynolds, *Electron and lattice transport phenomena in an antimony crystal at liquid-He^4 temperatures*, Phys. Rev. 140 (1965) A187, https://doi.org/10.1103/PhysRev.140.A187.
[33] A. Jaoui, A. Gourgout, G. Seyfarth, A. Subedi, T. Lorenz, B. Fauqué, K. Behnia, Formation of an electron-phonon Bi-fluid in bulk antimony, arXiv:2105.08408v2 (2021).
[34] T. Liang, Q. Gibson, J. Xiong, M. Hirschberger, S.P. Koduvayur, R.J. Cava, N. P. Ong, *Evidence for massive bulk Dirac Fermions in $Pb_{1-X}Sn_XSe$ from Nernst and thermopower experiments*, Nat. Commun. 4 (2013) 2696, https://doi.org/10.1038/ncomms3696.
[35] T. Liang, J. Lin, Q. Gibson, T. Gao, M. Hirschberger, M. Liu, R.J. Cava, N.P. Ong, *Anomalous Nernst Effect in the Dirac semimetal Cd_3As_2*, Phys. Rev. Lett. 118 (2017), 136601, https://doi.org/10.1103/PhysRevLett.118.136601.
[36] D. Shoenberg, Magnetic Oscillations in Metals, Cambridge Univ. Press, 1984.
[37] A.S. Joseph, A.C. Thorsen, Low-field de Haas—van Alphen effect in copper*, Phys. Rev. 134 (1964) A979, https://doi.org/10.1103/PhysRev.134.A979.
[38] A.S. Joseph, A.C. Thorsen, E. Gertner, L.E. Valby, Low-field de Haas-van Alphen effect in copper, Phys. Rev. 148 (1966) 569, https://doi.org/10.1103/PhysRev.148.569.
[39] A.S. Joseph, A.C. Thorsen, Low-field de Haas—van Alphen effect and Fermi surface in Ag and Au, Phys. Rev. Lett. 13 (1964) 9, https://doi.org/10.1103/PhysRevLett.13.9.
[40] R. Bi, Z. Feng, X. Li, J. Niu, J. Wang, Y. Shi, D. Yu, X. Wu, *Spin Zero and large Landé G-Factor in WTe_2*, New J. Phys. 20 (2018), 063026, https://doi.org/10.1088/1367-2630/aacbef.
[41] J. Wang, J. Niu, B. Yan, X. Li, R. Bi, Y. Yao, D. Yu, X. Wu, *Vanishing quantum Oscillations in Dirac semimetal $ZrTe_5$*, Proc. Natl. Acad. Sci. U.S.A. 115 (2018) 9145, https://doi.org/10.1073/pnas.1804958115.
[42] Y. Liu, X. Yuan, C. Zhang, Z. Jin, A. Narayan, C. Luo, Z. Chen, L. Yang, J. Zou, X. Wu, S. Sanvito, Z. Xia, L. Li, Z. Wang, F. Xiu, *Zeeman Splitting and dynamical mass Generation in Dirac semimetal $ZrTe_5$*, Nat. Commun. 7 (2016), 12516, https://doi.org/10.1038/ncomms12516.
[43] L. Xing, R. Chapai, R. Nepal, R. Jin, *Topological Behavior and zeeman Splitting in trigonal $PtBi_{2-X}$ single crystals*, npj Quantum Mater 5 (2020) 10, https://doi.org/10.1038/s41535-020-0213-9.
[44] M. Oestreich, W.W. Rühle, Temperature dependence of the electron Landé g factor in GaAs, Phys. Rev. Lett. 74 (1995) 2315, https://doi.org/10.1103/PhysRevLett.74.2315.
[45] M. Oestreich, S. Hallstein, A. Heberle, Temperature and density dependence of the electron Landé g factor in semiconductors, Phys. Rev. B Condens. Matter 53 (1996) 7911, https://doi.org/10.1103/PhysRevB.53.7911.
[46] K.L. Litvinenko, L. Nikzad, C.R. Pidgeon, J. Allam, L.F. Cohen, T. Ashley, M. Emeny, W. Zawadzki, B.N. Murdin, Temperature dependence of the electron Landé g factor in InSb and GaAs, Phys. Rev. B 77 (2008), 033204, https://doi.org/10.1103/PhysRevB.77.033204.
[47] J. Hübner, S. Döhrmann, D. Hägele, M. Oestreich, Temperature-dependent electron Landé g factor and the interband matrix element of GaAs, Phys. Rev. B Condens. Matter 79 (2009), 193307, https://doi.org/10.1103/PhysRevB.79.193307.
[48] W. Zawadzki, P. Pfeffer, R. Bratschitsch, Z. Chen, S.T. Cundiff, B.N. Murdin, C. R. Pidgeon, Temperature dependence of the electron spin g factor in GaAs, Phys. Rev. B 78 (2008), 245203, https://doi.org/10.1103/PhysRevB.78.245203.
[49] L. Zhang, Y.B. Chen, B. Zhang, J. Zhou, S. Zhang, Z. Gu, S. Yao, Y. Chen, *Sensitively temperature-dependent spin-orbit Coupling in $SrIrO_3$ thin films*, J. Phys. Soc. Japan 83 (2014), 054707, https://doi.org/10.7566/JPSJ.83.054707.
[50] C.-Z. Li, J.-G. Li, L.-X. Wang, L. Zhang, J.-M. Zhang, D. Yu, Z.-M. Liao, *Two-carrier transport induced Hall Anomaly and large tunable Magnetoresistance in Dirac semimetal Cd_3As_2 nanoplates*, ACS Nano 10 (2016) 6020, https://doi.org/10.1021/acsnano.6b01568.
[51] D. Xiao, M.-C. Chang, Q. Niu, Berry phase effects on electronic properties, Rev. Mod. Phys. 82 (2010) 1959, https://doi.org/10.1103/RevModPhys.82.1959.
[52] B. Wang, B. Singh, B. Ghosh, W.C. Chiu, M.M. Hosen, Q. Zhang, L. Ying, M. Neupane, A. Agarwal, H. Lin, A. Bansil, Topological crystalline insulator state with type-II Dirac fermions in transition metal dipnictides, Phys. Rev. B 100 (2019), 205118, https://doi.org/10.1103/PhysRevB.100.205118.

Supplementary material: Temperature driven spin-zero effect in $TaAs_2$

Md Shahin Alam [1], P.K. Tanwar [1], Krzysztof Dybko [1,2], Ashutosh S. Wadge [1], Przemysław Iwanowski [1,2], Andrzej Wiśniewski [1,2] and Marcin Matusiak [1,3,*]

1. *International Research Centre MagTop, Institute of Physics, Polish Academy of Sciences, Aleja Lotnikow 32/46, PL-02668 Warsaw, Poland*

2. *Institute of Physics, Polish Academy of Sciences, Aleja Lotników 32/46, PL-02668 Warsaw, Poland*

3. *Institute of Low Temperature and Structure Research, Polish Academy of Sciences, ul. Okólna 2, 50-422 Wrocław, Poland*

A: Nernst signal oscillations in $TaAs_2$ and corresponding fast Fourier transform spectra

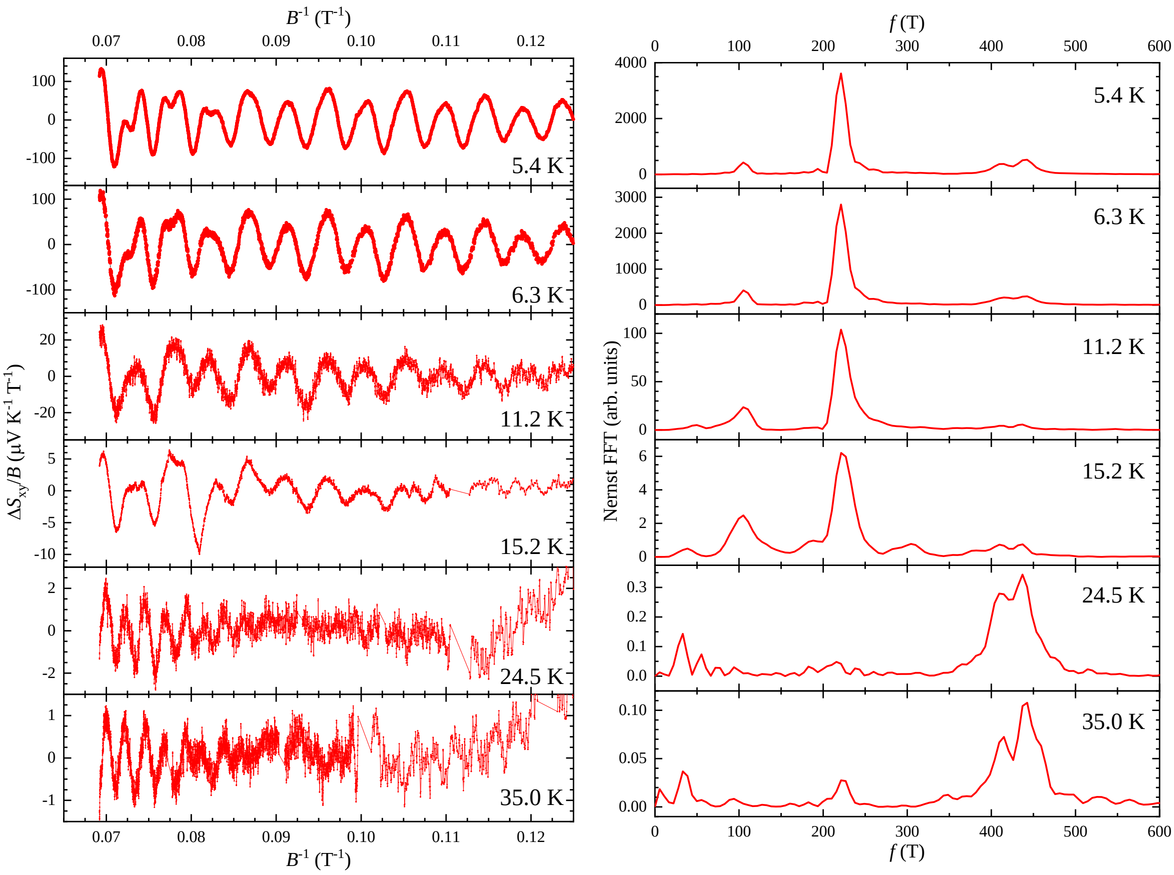

Figure S1. The oscillatory component of the Nernst coefficient in $TaAs_2$ plotted versus inverse magnetic field for various temperatures (left panel). The right panel presents respective FFT spectra.

Table S1. Parameters obtained from Lorentzian multiple peak fitting of the Nernst FFT spectra for β and 2β oscillations.

T **(K)**	**1st harmonic amplitude (arb. units)**	**2nd harmonic amplitude (arb. units)**	$\mathbf{A_1/A_2}$	**1st harmonic Frequency (T)**	**2nd harmonic Frequency (T)**
5.4	3.81E-16	4.94E-17	7.7	220	441
6.3	2.94E-16	2.05E-17	14	221	441
11.2	1.05E-17	3.85E-19	27	223	421
15.2	6.20E-19	5.69E-20	11	224	436
24.5	3.81E-21	2.98E-20	0.13	211	437
35.0	2.77E-21	9.89E-21	0.28	223	443

B: Temperature evolution of the β and 2β oscillations amplitudes

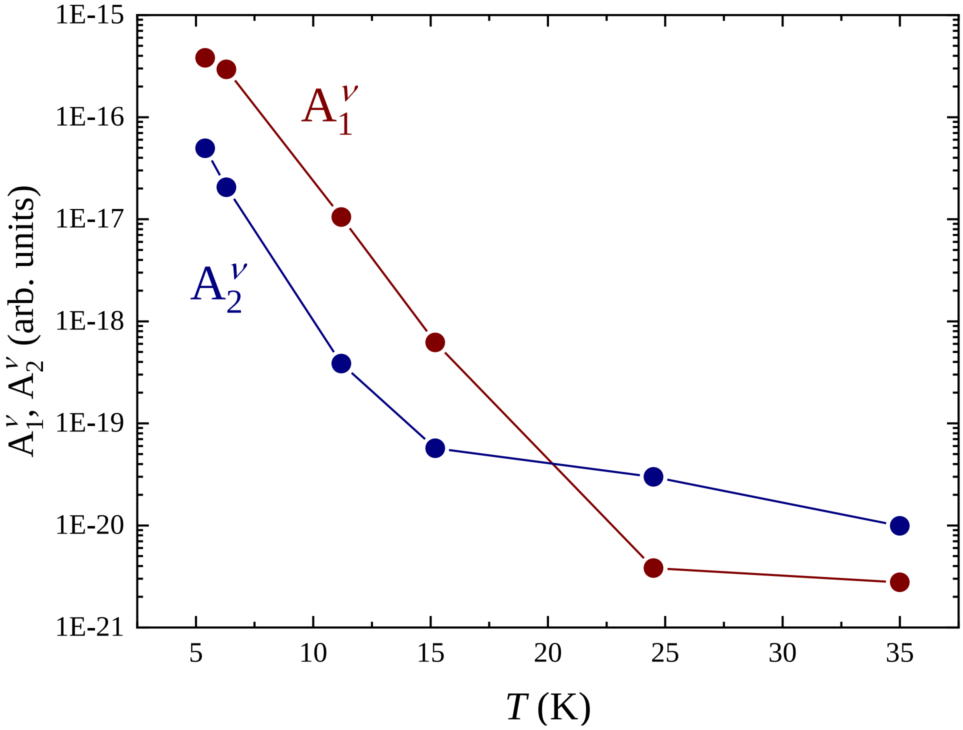

Figure S2. Calculated from the Nernst signal temperature dependence of the first (A_1^ν) and second (A_2^ν) harmonic amplitudes for the β band.

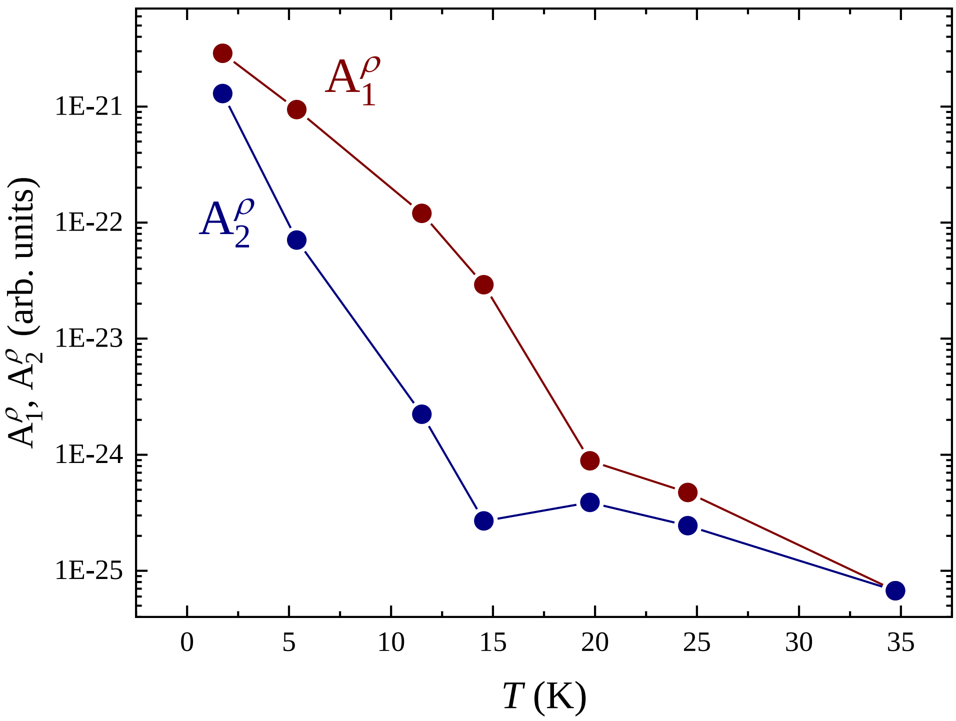

Figure S3. Calculated from the resistivity data temperature dependence of the first (A_1^ρ) and second (A_2^ρ) harmonic amplitudes for the β band.

B: Filtered Nernst signal

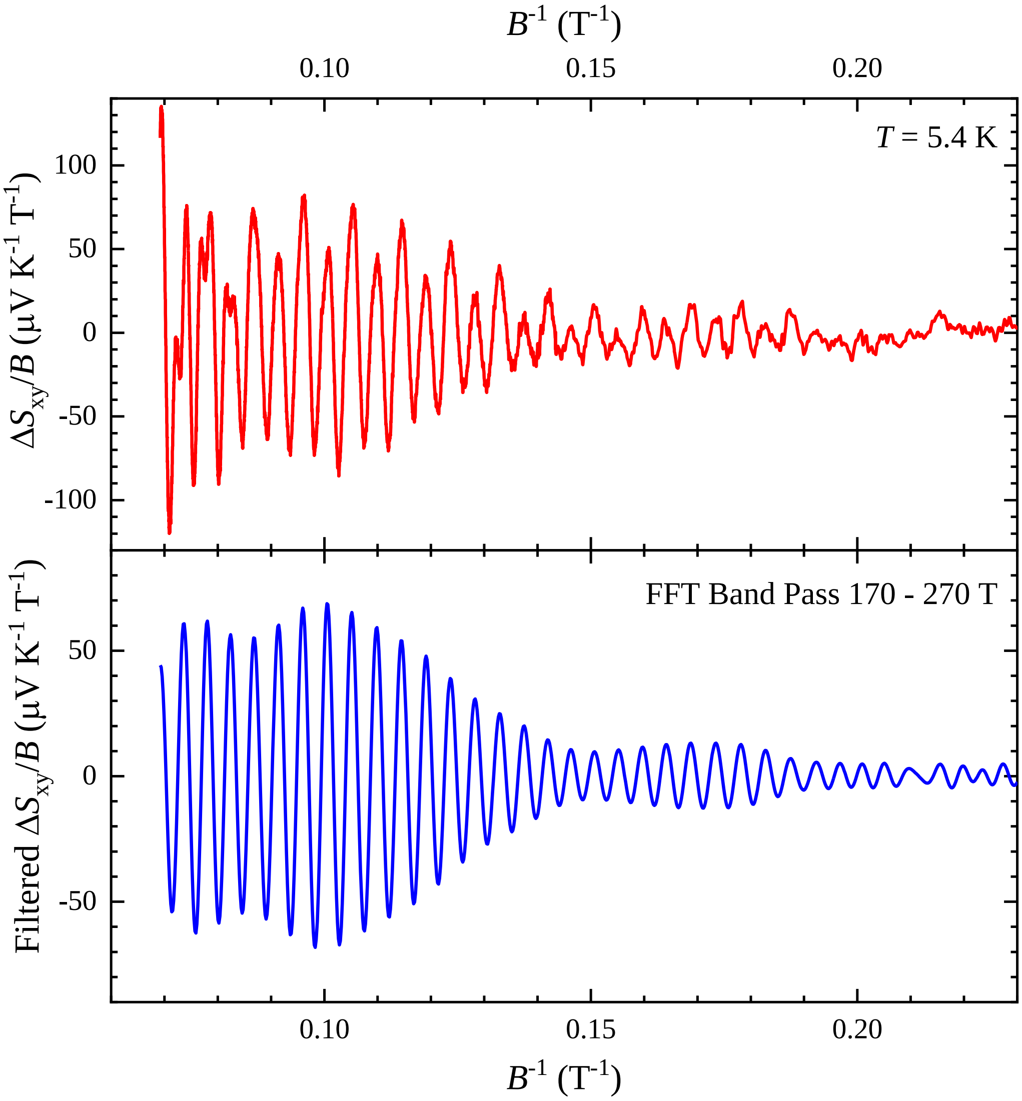

Figure S4. Upper panel: oscillatory Nernst signal in $TaAs_2$ measured at the temperature $T = 5.4$ K plotted versus inverse magnetic field. Lower panel: signal from the upper panel filtered with the FFT band pass filter for the 170 - 270 T frequency range (β oscillations).

C: Effective mass calculation

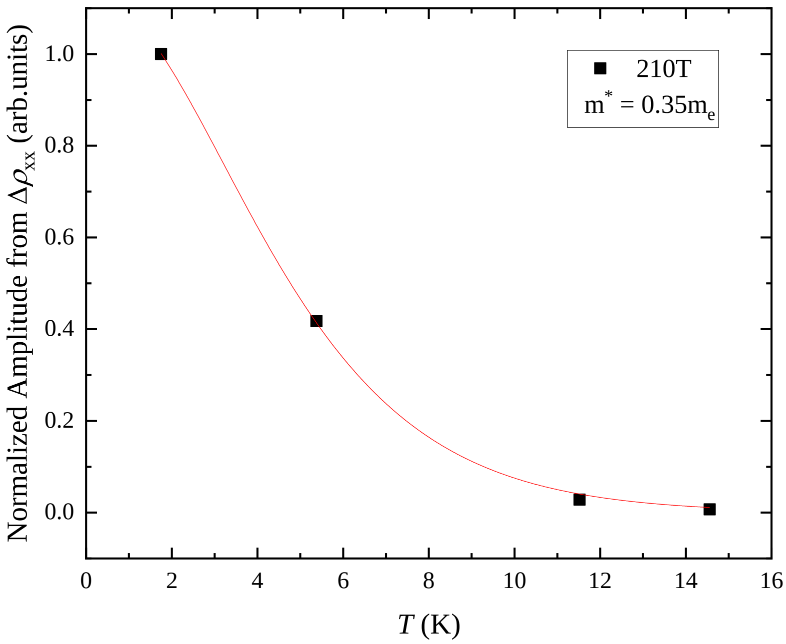

Figure S5. Temperature dependence of normalized FFT amplitude of the resistivity oscillations (8 T < B < 14.5 T) for the β frequency in $TaAs_2$. Solid line is fit of the Lifshitz-Kosevich formula.

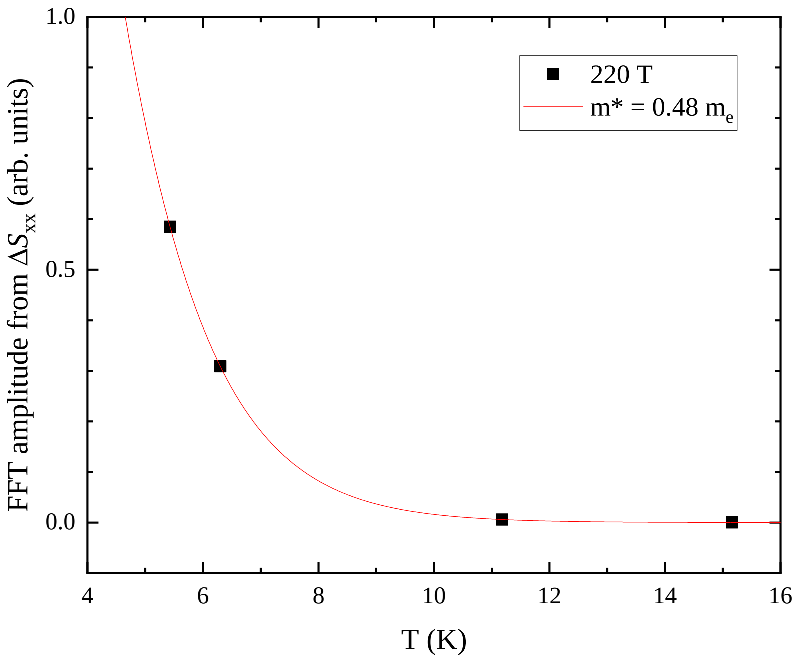

Figure S6. Temperature dependence of normalized FFT amplitude of the thermopower oscillations for the β frequency in $TaAs_2$, 5 T < B < 14.5 T. Solid line is fit of the modified Lifshitz-Kosevich formula [A.P. Morales et al., Phys. Rev. B **93**, 155120 (2016)]: $A(T) \propto \frac{(\alpha pX)\coth(\alpha pX)-1}{\sinh(\alpha pX)}$, where $\alpha = 2\pi^2 k_B/e\hbar$, k_B is the Boltzmann constant, e is the elementary charge, $\hbar$ is the reduced Planck constant, p is the harmonic number, and $X = m^*T/B$.

D: Amplitude ratio

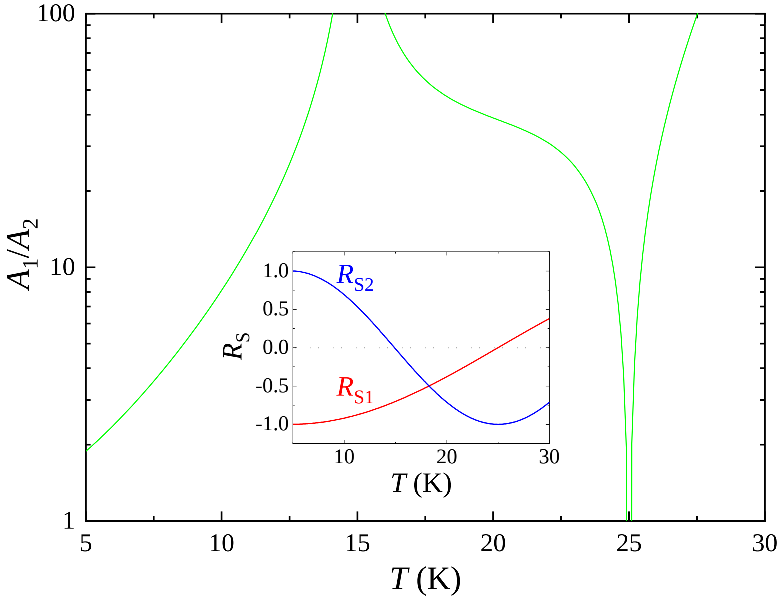

Figure S7. Temperature dependence of the absolute value of the first to second harmonic ratio calculated from the Lifshitz-Kosevich formula. The Dingle damping factor was assumed to be $R_D = 1$, the effective mass $m^* = 0.18\ m_0$, and the Landé g-factor linearly increasing with temperature to reach the spin zero condition at $T = 25$ K. Inset presents the temperature dependences of the spin damping factors for the fundamental frequency and its second harmonic. The latter goes through zero at $T \approx 15$ K which causes the second harmonic to disappear at this temperature. The resulting $A_1/A_2(T)$ qualitatively matches the experimental results, namely it initially (up to $T \approx 15$ K) increases, then decreases and goes through zero at $T = 25$ K and then increases again.

E: Sample

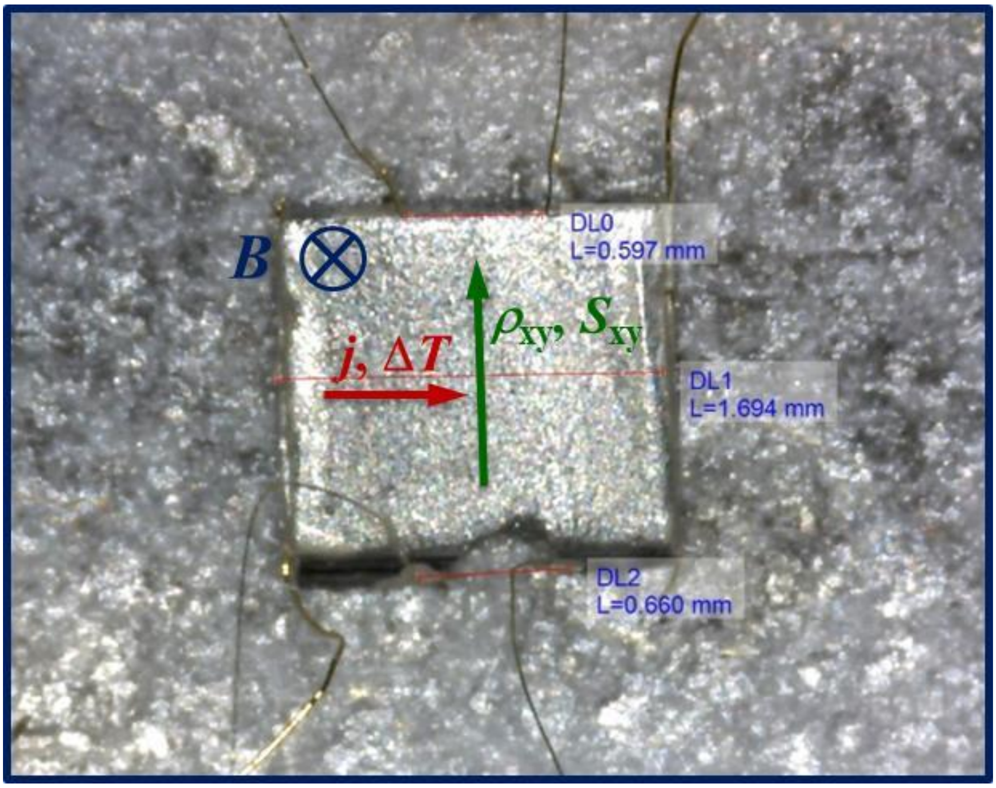

Figure S8. Single crystal of $TaAs_2$ with schematically shown experimental configuration.

3.1.2 ARTICLE II: Anomalous Hall and anomalous Nernst effect

The non-trivial topology of the electronic structure with Weyl nodes (WNs) near the Fermi level manifests itself in interesting phenomena such as the anomalous Hall and the anomalous Nernst effect. Generally, the creation of WNs requires breaking the time reversal symmetry or the inversion symmetry . Recently, it has been reported that in the case of RAlSi semimetals (R stands for rare earth element) Weyl points can be generated by SI breaking, whereas TRS breaking shifts the position of WNs in the k-space [46,96,106,107]. An example is the ferromagnetic Weyl semimetal CeAlSi, which makes it an unique platform for studying the interplay between magnetism and topology. In this study, we reported the sign reversal of anomalous Hall conductivity in the ferromagnetic phase of CeAlSi for two different orientations of magnetic field, namely AHC is negative ($\sigma_{yz}^{A} < 0$) for $B \parallel a$, and positive ($\sigma_{xy}^{A} > 0$) for $B \parallel c$, where a and c denote the crystallographic axes. We indicated that the sign change of AHC in CeAlSi originates from the band structure reconstruction driven by the spin reorientation. The anomalous contribution has also been visible in the thermoelectric Nernst conductivity (α_{xy}^{A}) measured for $B \parallel c$. Furthermore, we observed persistence of anomalous Hall and Nernst signals even in the paramagnetic phase. To explain the temperature dependences of σ_{xy}^{A} and α_{xy}^{A}/T above the Curie temperature, we proposed a single band toy-model, which includes a finite Berry curvature in the vicinity of Weyl nodes. The temperature dependences of σ_{xy}^{A} and α_{xy}^{A}/T calculated using this simplistic approach correspond well to the experimental ones. This indicate that origin of high temperature large σ_{xy}^{A} and non-vanishing α_{xy}^{A} lies in the CeAlSi topology.

Sign change of anomalous Hall effect and anomalous Nernst effect in the Weyl semimetal CeAlSi

Md Shahin Alam,[1,*] Amar Fakhredine,[2] Mujeeb Ahmad,[1] P. K. Tanwar,[1] Hung-Yu Yang,[3] Fazel Tafti,[3] Giuseppe Cuono,[1] Rajibul Islam,[1] Bahadur Singh,[4] Artem Lynnyk,[2] Carmine Autieri,[1,†] and Marcin Matusiak[1,5,‡]

[1]*International Research Centre MagTop, Institute of Physics, Polish Academy of Sciences, Aleja Lotników 32/46, PL-02668 Warsaw, Poland*
[2]*Institute of Physics, Polish Academy of Sciences, Aleja Lotników 32/46, PL-02668 Warsaw, Poland*
[3]*Department of Physics, Boston College, Chestnut Hill, Massachusetts 02467, USA*
[4]*Department of Condensed Matter Physics and Materials Science, Tata Institute of Fundamental Research, Mumbai 400005, India*
[5]*Institute of Low Temperature and Structure Research, Polish Academy of Sciences, ulica Okólna 2, 50-422 Wrocław, Poland*

(Received 17 October 2022; revised 14 December 2022; accepted 18 January 2023; published 3 February 2023; corrected 1 March 2023)

We report the anomalous Hall effect (AHE) and the anomalous Nernst effect (ANE) data for the noncollinear Weyl semimetal CeAlSi. The anomalous Hall conductivity (σ_{ij}^A) was measured for two different orientations of the magnetic field (B), namely σ_{yz}^A for $B||a$ and σ_{xy}^A for $B||c$, where a and c denote the crystallographic axes. We find that σ_{xy}^A and σ_{yz}^A are of opposite sign and both are large below the Curie temperature (T_C). In the paramagnetic phase, σ_{xy}^A rises even more and goes through a maximum at $T \approx 170$ K, whereas the absolute value of σ_{yz}^A decreases with increasing temperature. The origin of the sign difference between σ_{xy}^A and σ_{yz}^A was attributed to the reconstruction of the band structure under the variation of the spin orientation. Further, in a system where humps in the AHE are present and scalar spin chirality is zero, we show that the **k**-space topology plays an important role to determine the transport properties at both low and high temperatures. We also observed the anomalous contribution in the Nernst conductivity (α_{xy}^A) measured for $B||c$. α_{xy}^A/T turns out to be sizeable in the magnetic phase and above T_C slowly decreases with temperature. We were able to recreate the temperature dependencies of σ_{xy}^A and α_{xy}^A/T in the paramagnetic phase using a single band toy model assuming a nonzero Berry curvature in the vicinity of the Weyl node. A decisive factor appears to be a small energy distance between the Fermi level and a Weyl point.

DOI: 10.1103/PhysRevB.107.085102

I. INTRODUCTION

Topological Weyl semimetals (WSMs) are characterized by linear energy dispersions of the valence and conduction bands touching each other in momentum space at Weyl nodes [1–4]. The emergence of massless Weyl fermions as low-energy excitations manifests in many exotic physical effects like the presence of Fermi arcs on the surface [5], chiral anomaly induced negative magnetoresistance [6], chiral zero sound effect [7,8], etc. The subclass of WSMs that also exhibit magnetic ordering is a particularly interesting object of study [9–15]. These materials allow, for example, the manipulation of the anomalous Hall and anomalous Nernst effect [16,17], which is interesting from both scientific and applicative points of view. Recently, huge efforts have been made to investigate the sign change of the anomalous Hall effect (AHE) in Weyl fermions or closely relevant systems as the collinear ferromagnet $SrRuO_3$ [18]. It turns out that many factors, such as the value of the magnetization [19], the presence of the interface which can tune the spin-orbit coupling (SOC), or breaking of the inversion symmetry [20], can change the sign of AHE. Moreover, in the presence of the sign change, the anomalous Hall effect may take values smaller than other features, such as humps in the hysteresis loop of AHE [19,20]. The presence of these humps seems to be particularly favored by a large spin-orbit coupling as well as the absence of inversion symmetry [19,20] and in CeAlSi they were dubbed the loop Hall effect [21]. In CeAlSi, the humps are related to the **k**-space topology [21]. In order to get more insight into the **k**-space topology that governs these humps in CeAlSi, we investigated CeAlSi focusing on the transport properties in magnetic fields and looking for the sign change of the AHE. Additionally, we also measured the anomalous Nernst effect (ANE), whose response to nonzero Berry curvature around the Fermi energy is different than that expected for AHE. In the paramagnetic phase of CeAlSi, the simultaneous temperature evolution of both ANE and AHE can be well described by a simple model assuming the presence of the Weyl node about 20 meV from the Fermi level. The paper is organized as follows: We describe the material and methods in Sec. II; in Sec. III, we present our experimental results; in Sec. IV, we discuss our results, and in Sec. V we summarize our conclusions.

II. MATERIAL AND METHODS

CeAlSi single crystals were grown by a self-flux method using the Canfield crucible sets. The starting materials were weighed in the ratio Ce : Al : Si = 1 : 10 : 1, placed inside a crucible in an evacuated quartz tube, heated to 1000 °C at 3 °C/min, held at 1000 °C for 12 h, cooled to 700 °C at

*shahin@magtop.ifpan.edu.pl
†autieri@magtop.ifpan.edu.pl
‡matusiak@magtop.ifpan.edu.pl

0.1 °C/min, stayed at 700 °C for 12 h, and centrifuged to decant the residual Al flux.

For electrical and thermoelectrical transport measurements a suitable single crystal was cut into a plate with dimensions of $1.4 \times 1.3 \times 0.4$ mm^3 with sides parallel to the natural crystallographic $a \times a \times c$ axes. The electrical and thermal currents were applied along the longest side of the sample (a axis), while the magnetic field (B) was applied parallel to the c axis and perpendicular to the thermal and electrical currents. For electrical measurements with B applied along the crystallographic a axis we selected another single crystal, which was cut into a plate with dimensions of $0.2 \times 2.9 \times 0.6$ mm^3 ($a \times a \times c$). The electrical current (J) was applied along the a axis and B was perpendicular to the current and parallel to another a axis.

For the electrical measurements, the contacts were arranged in the Hall-bar geometry with 25-μm-thick gold wires attached to the sample using DuPont 4929N silver paste. During the measurements of thermoelectric power (S_{xx}) and Nernst signal (S_{yx}) the sample was mounted between two blocks made of phosphor bronze. The temperature difference was determined using two Cernox thermometers and the thermal gradient was implied using a strain gauge as a resistive heater. For selected temperatures, the magnetic field was swept from -14.5 to $+14.5$ T to extract the field voltage components that were antisymmetric and symmetric in B. All the presented data were symmetrized and antisymmetrized for the positive and negative magnetic fields.

Magnetic properties of the sample have been investigated using a Quantum Design Magnetic Property Measurement System MPMS XL equipped with a superconducting quantum interference device. The reciprocating sample option has been chosen to provide a precision of about 10^{-8} emu during the direct current (dc) measurements. A magnetic moment as a function of external dc magnetic field has been measured in the range –7 to +7 T after cooling at zero field. To study the temperature dependencies of susceptibility, alternative current (ac) option has been utilized. An ac field of 1 Oe amplitude and 1 kHz of frequency has been applied during the measurements.

III. RESULTS

The electrical transport properties of CeAlSi were studied for two different orientations of the magnetic field (B), which was applied along the a axis (magnetically easy) or along the c axis (magnetically hard). The temperature (T) dependence of the longitudinal resistivity (ρ_{xx}) for the electrical current (J) parallel to the a axis and $B = 0$ T (see Fig. 1) shows semimetallic behavior with the residual resistivity ratio of 3.2 (see Fig. 1). A kink at $T_C \approx 8.5$ K appears due to the transition from the high-temperature-paramagnetic (PM) phase to the low-temperature ferromagnetic (FM) phase [21]. The value of the transition temperature and overall temperature dependence of ρ_{xx} agree well with the previous reports [21–23]. The magnetic field dependencies of the longitudinal resistivity (ρ_{xx}) and Hall resistivity (ρ_{yx}) ($B||c$ and $J||a$), as well as ρ_{yy} and ρ_{zy} (B and $J||a$, $B\perp J$) are shown in Fig. 2. The Hall resistivities for both orientations of B [Figs. 2(b) and 2(d)] becomes negative at low temperature and high magnetic field,

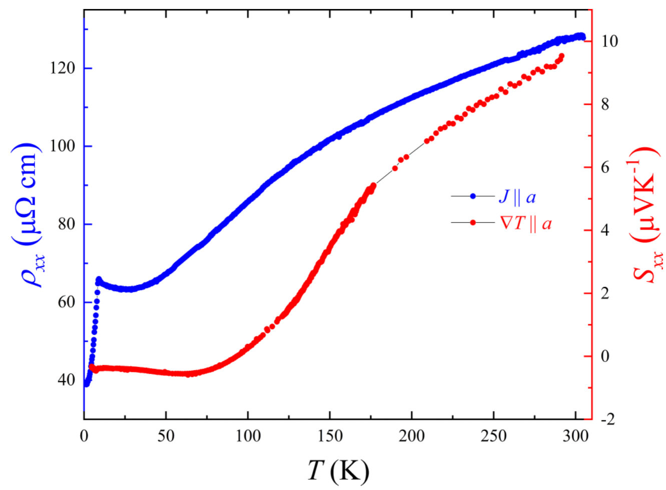

FIG. 1. Temperature dependencies of the zero field resistivity (ρ_{xx}) and the thermoelectric power (S_{xx}) of the noncollinear Weyl semimetal CeAlSi with the current (J) or thermal gradient (∇T) applied parallel to a axis.

which indicates that the electronlike charge carriers dominate electrical transport in this region. Specifically, at $B = 14.5$ T, $\rho_{yx} \approx -35\ \mu\Omega$ cm for $T \approx 5.4$ K and $\rho_{zy} \approx -65\ \mu\Omega$ cm for $T \approx 1.7$ K. However, the high-field slope of the ρ_{yx} Hall resistivity evolves with temperature and becomes slightly positive at room temperature ($d\rho_{yx}/dB = 1.2 \times 10^{-9}$ m^{-3} C^{-1} at $T = 301$ K), which might be due to the slowly increasing with temperature role of holes in the electrical transport.

A prominent characteristic of the Hall resistivity in CeAlSi is its nonlinear field dependence [see Fig. 2(b)]. Although this type of behavior might be due to simultaneous contributions from different types of charge carriers [24,25], it seems to be not the case in CeAlSi. In fact, ρ_{yx} varies linearly at high field, but $\rho_{yx}(B)$ does not extrapolate to $\rho_{yx} = 0\ \mu\Omega$ cm at $B = 0$ T. The field dependence of ρ_{yx} cannot be satisfactorily explained within the two-band model approach as shown in Fig. S1 in the Supplemental Materials (SM) [26] (see also Refs. [27–31] therein), which is in line with the previous reports indicating that the transport in CeAlSi is dominated at low temperatures by a single type of charge carrier [32]. A likely cause for the nonlinear behavior of the Hall resistivity in CeAlSi is a contribution from the anomalous Hall effect (AHE) [21,33–36]. In general, the magnetic field dependencies of Hall resistivity in the presence of the anomalous contribution can be expressed as

$$\rho_{yx} = R_0 B + \rho_{yx}^A, \tag{1}$$

where R_0 is the ordinary Hall coefficient and ρ_{yx}^A is the anomalous Hall resistivity. To determine R_0 and to separate ρ_{yx}^A (or ρ_{zy}^A) from the total Hall resistivity, $\rho_{yx}(B)$ [or $\rho_{zy}(B)$] was fitted with a linear function in the high-field regime (>3 T) [see Figs. 3(a) and 3(b)]. At low temperature, the fitting range of the former was restricted to $B_{\max} = 9$ T, because of a change in the $\rho_{yx}(B)$ slope happening at this field. This anomaly is also visible in the field dependencies of ρ_{xx} [Fig. 2(a)] and it is likely related to the magnetic phase transition caused by increasing magnetic field perpendicular to the initially FM

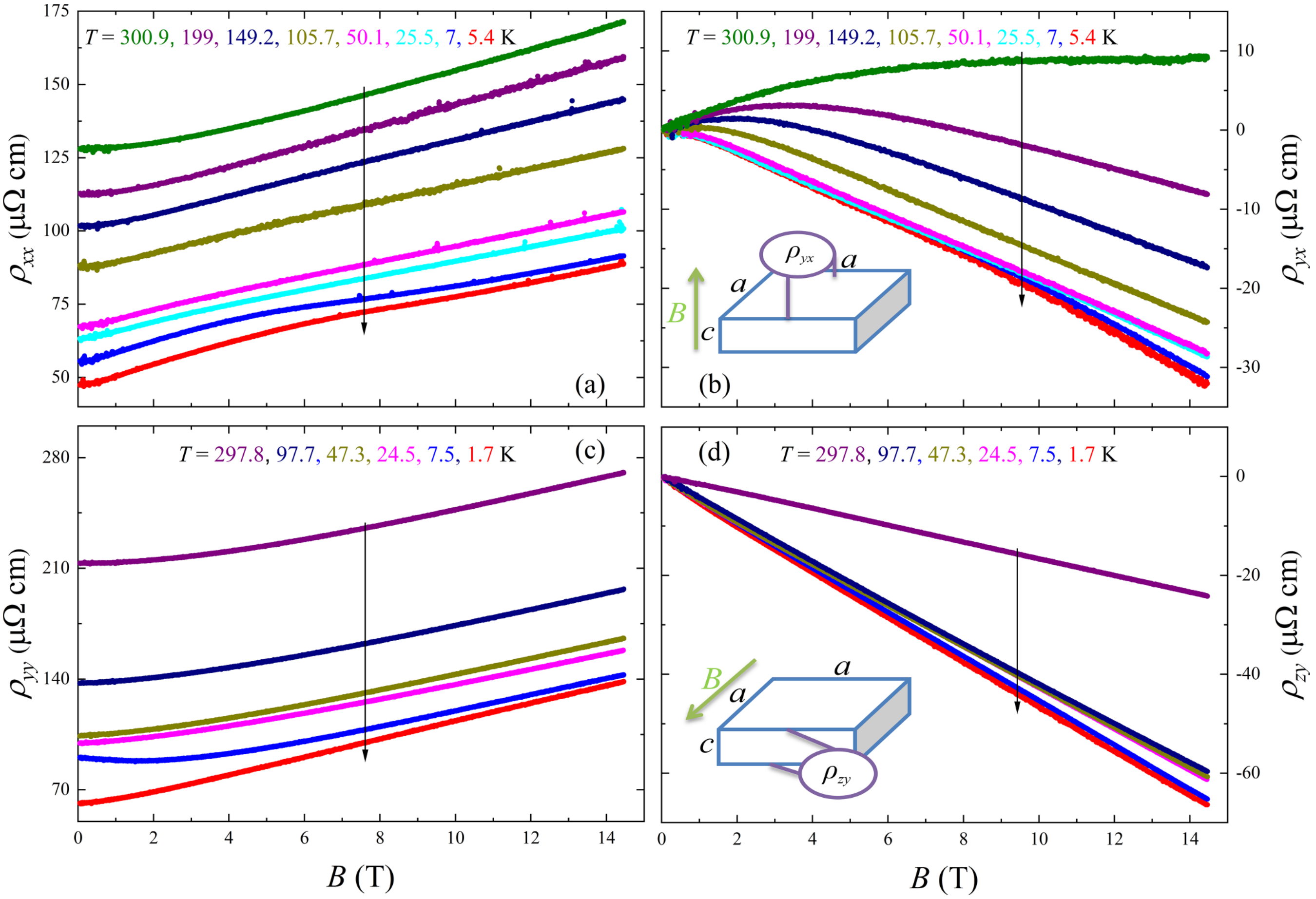

FIG. 2. Magnetic field dependencies of the longitudinal resistivity and Hall resistivity in CeAlSi for two different configurations of the sample. For $J \parallel a$ and $B \parallel c$, (a) longitudinal resistivity (ρ_{xx}); (b) Hall resistivity (ρ_{yx}), $J \parallel a$, $B \parallel a$, and $B \perp J$; (c) longitudinal resistivity (ρ_{yy}); (d) Hall resistivity (ρ_{zy}). The black vertical arrows in all the panels indicate variation of the temperature.

ordered spins [37]. The extracted field dependencies of the anomalous Hall resistivity for $B||c$ (ρ_{yx}^A) and $B||a$ (ρ_{zy}^A) are presented in Figs. 3(c) and 3(d). In the FM phase, both ρ_{yx}^A and ρ_{zy}^A are sizeable, but different in sign and magnitude. In the PM phase, the absolute value of ρ_{yx}^A becomes significantly larger than ρ_{zy}^A.

In general, the AHE can be of intrinsic or extrinsic origin and the latter can be due to the skew-scattering or side-jump processes [27]. If there were a contribution from an extrinsic mechanism, one would expect a specific relation between the resulting anomalous Hall conductivity (AHC, σ_{ij}^A) and the longitudinal conductivity (σ_{ii}). Namely, for the skew scattering, the AHC should follow a linear relationship with the longitudinal conductivity, whereas for the side jump (which is expected to be somewhat smaller [38]) $\sigma_{ij}^A \sim \sigma_{ii}^2$ [39]. In our data we observe neither of them (Fig. S2 in the SM [26]). Furthermore, in topological semimetals with the Fermi level in the vicinity of Weyl nodes, the AHE has been predicted to be predominantly intrinsic and determined by the location of the Weyl points [40,41]. Since CeAlSi has been identified as a Weyl semimetal with Weyl nodes close to the Fermi level [21], one can expect a nonzero AHE due to its nontrivial topological properties [21–23,42]. These are expected to manifest themselves also in other transport phenomena.

The magnetic field dependence of thermoelectric power with the thermal gradient $\nabla T||a$ and $B||c$ is presented in Fig. 4(a). $S_{xx}(B)$ can be satisfactorily fitted with the semiclassical phenomenological model proposed by Liang *et al.* [43]:

$$S_{xx}(B) = S_{xx}^0 \frac{1}{1+(\mu B)^2} + S_{xx}^\infty \frac{(\mu B)^2}{1+(\mu B)^2}, \tag{2}$$

where S_{xx}^0 and S_{xx}^∞ are the amplitudes of the thermopower at zero and high field limits respectively, and μ is the mobility of charge carriers. A shift of S_{xx}^0 from negative at low temperatures to positive at high temperatures can be a sign of an increase in the participation of holes, which is consistent with the Hall resistivity data discussed earlier. If these holes have low mobility, then their contribution will be only slightly field dependent and will not disturb the fitting procedure, which in fact works well for all the data [see Fig. 4(a)]. At low temperatures, we restricted again the fitting field range due to the change in $S_{xx}(B)$ slope at $B \sim$ 8–9 T owing to the aforementioned field-induced transition. The temperature dependence of S_{xx} at zero magnetic field is shown in Fig. 1.

Figure 4 presents the field dependencies of the Nernst effect signal measured for a configuration analogous to ρ_{yx}, i.e., $\nabla T \parallel a$ and $B||c$. Results are fitted with the empirical model [44] describing the behavior of the Nernst effect in a

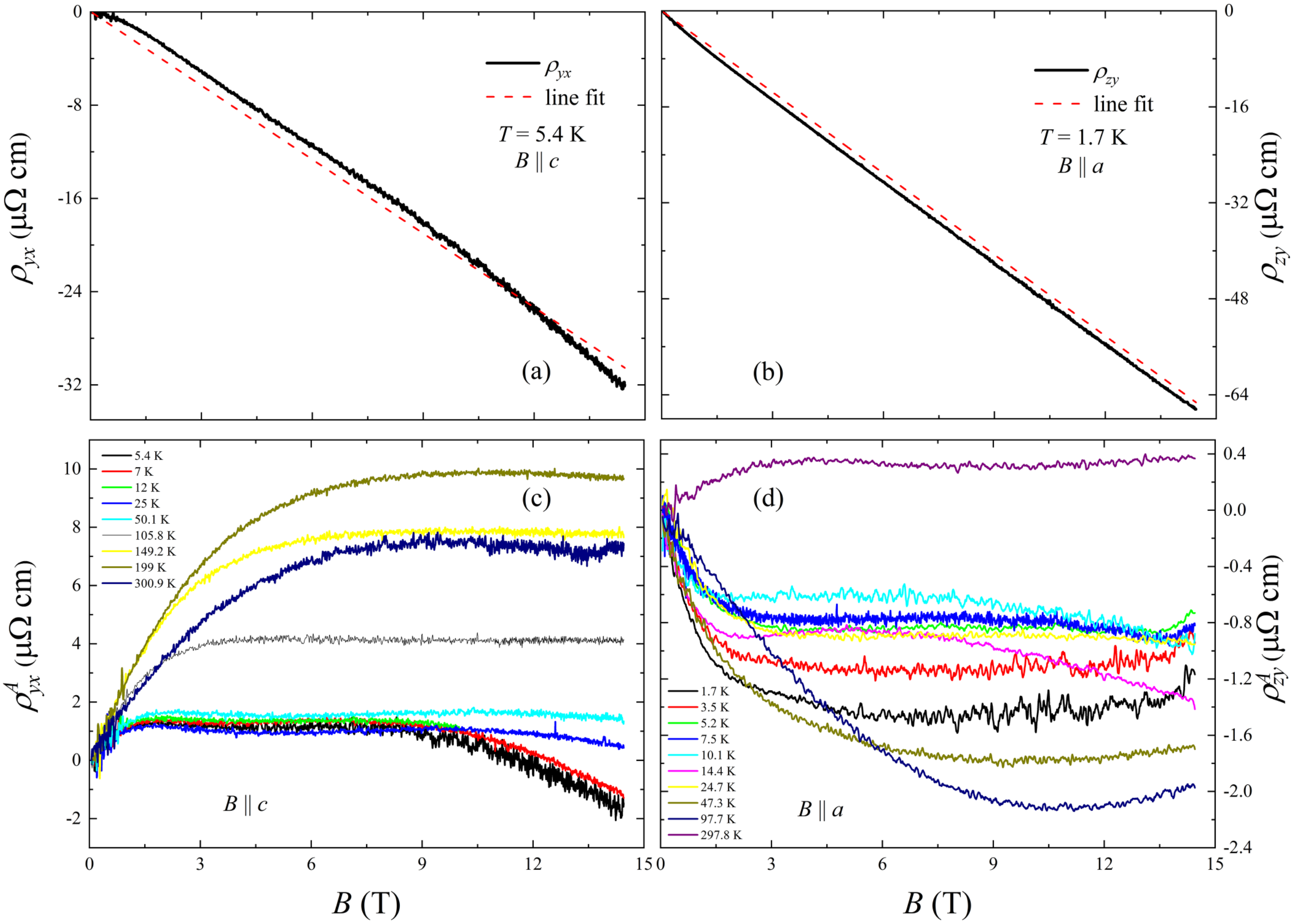

FIG. 3. Magnetic field dependencies of the Hall resistivity in CeAlSi: (a) Hall resistivity (ρ_{yx}) as a function of B at T = 5.4 K (black line); (b) Hall resistivity (ρ_{zy}) as a function of B at T = 1.7 K (black line). Red dashes lines in (a) and (b) represent the high-field ($B > 3$ T) linear fits. (c) Anomalous contribution to the Hall resistivity (ρ^A_{yx}) extracted from $\rho_{yx}(B)$ for several temperatures. (d) Anomalous contribution to the Hall resistivity (ρ^A_{zy}) extracted from $\rho_{zy}(B)$ for several temperatures.

topologically nontrivial material. Here, the total Nernst signal is similar to the Hall resistivity and is divided into a normal (S^N_{yx}) and an anomalous (S^A_{yx}) part:

$$S_{yx} = S^N_{yx} + S^A_{yx}, \tag{3}$$

where their field dependencies are expressed as

$$S^N_{yx} = S^N_0 \frac{\mu}{1 + (\mu B)^2}, \tag{4}$$

$$S^A_{yx} = S^A_{yx} \tanh{(B/B_s)}, \tag{5}$$

μ is the mobility, and B_s is the saturation field at which the plateau of the anomalous signal is reached. Apparently, the field dependencies of S_{yx} cannot be described only by the conventional Nernst contributions [Eq. (4)] (see Fig. S1 in the SM [26]), but they are very well approximated when the anomalous component [Eq. (5)] is taken into consideration [see Fig. 4(b)]. The temperature dependence of the normalized (divided by temperature) S^A_{yx} is displayed in the inset of Fig. 5(b). In the FM phase S^A_{yx}/T steeply increases with decreasing the temperature (reaching $S^A_{yx} \approx -0.1$ μVK^{-2} at 2.5 K), but also in the PM phase there is a nonvanishing anomalous contribution (in the order of $S^A_{yx} \approx -0.02$ μVK^{-2}) slowly decreasing with temperature.

IV. DISCUSSION

The anomalous Hall (σ^A_{ij}) and transverse thermoelectric (α^A_{ij}) conductivities can be calculated as [45–47]

$$\sigma^A_{ij} = \frac{\rho^A_{ji}}{\rho^2_{ii}}, \tag{6}$$

$$\alpha^A_{ij} = S^A_{ji}\sigma_{ii} - S_{ii}\sigma^A_{ij}, \tag{7}$$

if $\rho_{ii} \gg \rho^A_{ji}$. The resulting temperature dependences of $\sigma^A_{xy}(T)$ and $\alpha^A_{xy}/T(T)$ are presented in Fig. 5. Two temperature regions can be distinguished: (i) $T < T_C$ (FM phase) and (ii) $T > T_C$ (PM phase).

(i) In the ferromagnetic phase σ^A_{xy} gradually increases with decreasing temperature reaching ~550 Ω^{-1} cm^{-1} at T = 5.4 K [Fig. 5(a)]. The loop Hall effect (LHE) was reported to occur in CeAlSi in the FM phase with $B||c$ field orientation [21], but the appearance of this phenomenon changes from sample to sample depending on a slight off-stoichiometry

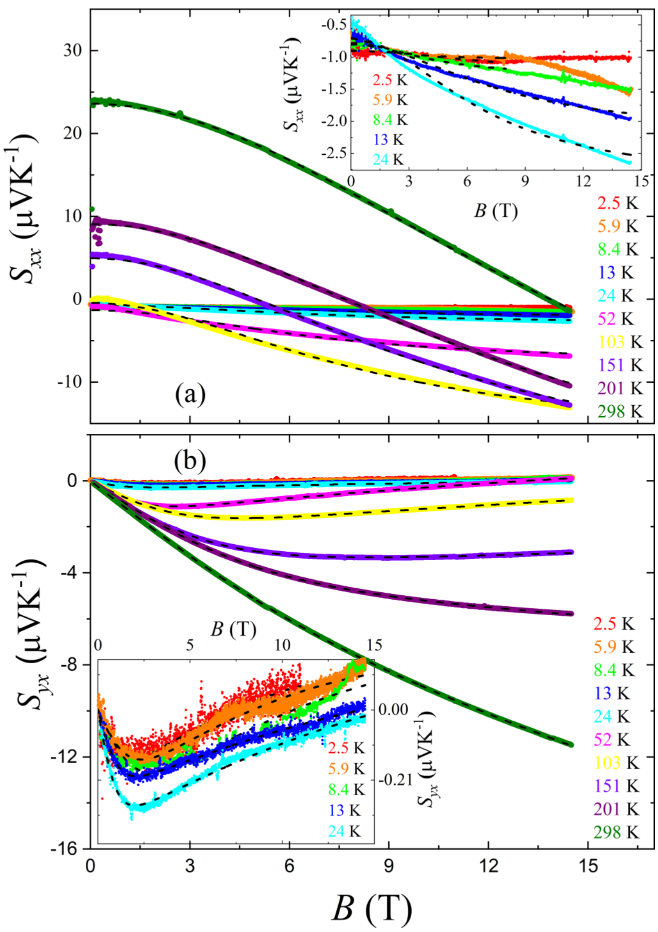

FIG. 4. Magnetic field dependence of the Seebeck (a) and Nernst (b) signal in CeAlSi for various temperatures. Insets show low-temperature field dependencies of the respective coefficients. The black dashed lines in (a) and (b) show fits prepared using Eqs. (2) and (4).

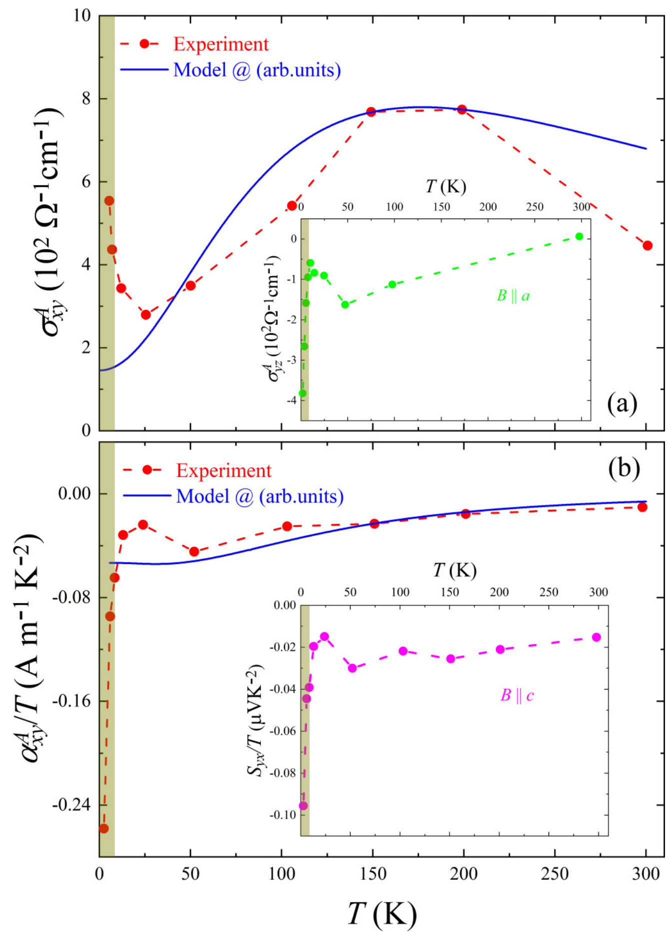

FIG. 5. The temperature dependencies of the anomalous Hall conductivity (σ^A_{xy}) (a) and the anomalous Nernst conductivity (b) for $B||c$ in CeAlSi. Inset in the upper panel shows temperature dependent anomalous conductivity (σ^A_{yz}) for $B||a$; inset in the lower panel presents the temperature dependence of normalized anomalous Nernst effect for $B||c$. Blue solid lines in both panels present the σ^A_{xy} and α^A_{xy}/T T emperature dependencies calculated in arbitrary units using Eqs. (8) and (9). Vertical dark yellow areas in all panels represent the FM regime.

of Si and Al [21]. In this material class, the Weyl nodes are generated due to the lack of inversion symmetry in the noncollinear phase [21,22], while for the ferromagnetic phase Weyl points can be generated also by the breaking of time-reversal symmetry [42]. A recent study on CeAlSi suggested a nontrivial π Berry phase that has been experimentally reported in the FM regime for the magnetic field oriented along the c axis [23].

Similarly to σ^A_{xy}, we also determined the T dependence of σ^A_{yz} for the magnetic field oriented along the easy axis. $\sigma^A_{yz}(T)$ is presented in the inset of Fig. 5(a). We found $\sigma^A_{yz} \approx -380\ \Omega^{-1}\ \mathrm{cm}^{-1}$ at $T = 1.7$ K, a magnitude that is consistent with the previous reports [21]. Differences in values of σ^A_{xy} and σ^A_{yz} can be attributed to the anisotropic electronic structure of CeAlSi, while the observed sign change may be relevant for the detection of topological features in the AHE. Its occurrence, for example, was recently associated with the presence of humplike features in $\rho_{yx}(B)$ [19,48]. A physical origin of this anomaly is under strong debate, but it could derive from topological effects in the k space and/or in the real space. In CeAlSi the appearance of the analogous loop Hall effect appears to be dependent on the position of the Fermi level [21].

We study the magnetic configurations with spins along the a and the c axis (x and z, respectively) in addition to the noncollinear magnetic configuration that is the ground state. Using density functional theory (DFT) and Wannierization techniques, we perform the self-consistent and band structure calculations for different magnetic configurations to investigate the sign change of the AHE in the magnetic phase below $T_C = 8.5$ K.

From the self-consistent calculation, we note that the magnetization is mostly coming from the $4f$ electrons of Ce. The local magnetic moment per Ce atom is approximatively constant in all magnetic configurations. The magnetic moment for the $4f$ orbitals is 0.85–0.89μ_B where the lowest value is for the noncollinear magnetic configuration and the highest is for both collinear configurations. We have an intrinsic magnetic moment from $4f$ orbitals and an induced magnetic moment on the $5d$ orbitals of Ce that is $0.03\mu_B$ within DFT. The f electrons induce a ferromagnetic moment on

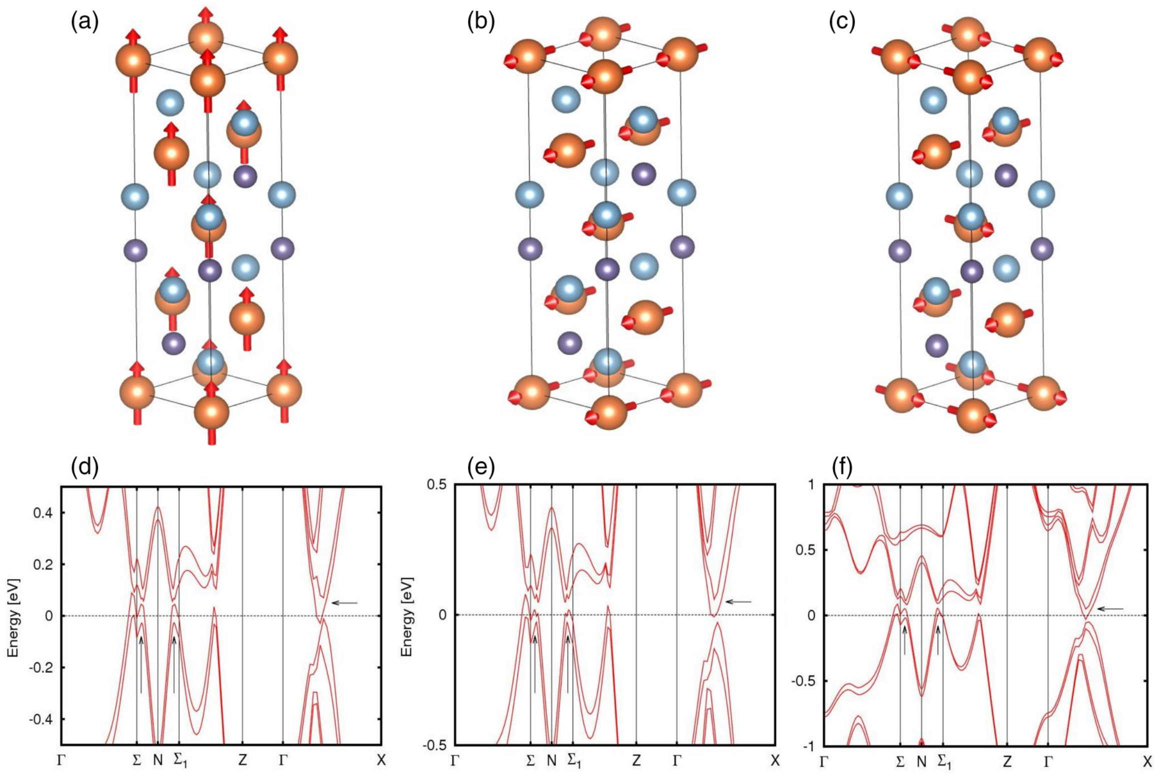

FIG. 6. Magnetic configurations and associated band structures of the CeAlSi Weyl semimetal. (a) Collinear FM order with spins aligned along the *a* axis. (b) Collinear FM order with spins aligned along the *c* axis. (c) Noncollinear FM order. (d)–(f) represent the band structure of CeAlSi along the high symmetry paths including spin-orbit coupling in the three mentioned configurations respectively. The vertical arrows represent the band crossings at the Fermi surfaces between **Σ**-**N** and N-$\mathbf{\Sigma_i}$, while the horizontal arrows point at the minimum of the conduction band between **Γ** and **X**.

the *d* electrons of Ce in the same fashion as happens in the $EuTiO_3/SrTiO_3$ system [49]. The presence of magnetic *f* electrons far from the Fermi level and *d* electrons at the Fermi level makes it difficult to produce a simplified tight-binding model containing both *d* and *f* orbitals. The bands associated with the Weyl points mainly come from the *d* electrons of Ce and the *sp* electrons of Al and Si as clearly visible in the local density of states (see part E in the SM [26]).

We report in Figs. 6(a)–6(c) the magnetic configurations with the Ce spins along the *a* axis, the *c* axis, and with the noncollinear configuration, respectively, where *a* and *c* are the lattice constants of the conventional unit cell shown in the figure. The band structures associated with these magnetic configurations are in the respective bottom panels in Figs. 6(d)–6(f). The main features of the three band structures are the same, but the different magnetic configurations slightly move the details of the low energy features and switch the position of the Weyl points [50]. One relevant change for the AHE appears along the high-symmetry path **Σ**-**N** and N-$\mathbf{\Sigma_i}$ where we can see at the position of the vertical arrows that the bands close to the Fermi level are slightly lower in energy in the case of the magnetic configuration with spin along the *c* axis shown in Fig. 6(e); as a consequence the minimum of the conduction band along **ΓX** goes higher in energy in Fig. 6(e). Therefore, the AHE will be modified by an energy shift approximatively equal to the difference between the Weyl points for the case with spin along the *c* axis ($E^{z}_{\rm WP}$) and the *a* axis ($E^{x}_{\rm WP}$). Defined as $\Delta E_{\rm WP} = E^{z}_{\rm WP} - E^{x}_{\rm WP} > 0$, this shift will be reflected in the AHE calculations. Basically, the different magnetic orderings influence the position of the Fermi level and the energy position of the Weyl points, and the anticrossing points close to the Fermi level.

It is known that close to the high-symmetry line **ΓX** T here are several Weyl points [42]. In CeAlSi, there are Weyl points from the breaking of the inversion symmetry and Weyl points from the breaking of the time-reversal symmetry. The Weyl points from the breaking of the time reversal present along **ΓX** are expected to be more sensitive to the orientation of the magnetic order, therefore strong changes in the AHE are expected.

Given the three band structures in Figs. 6(d)–6(f), we extracted the Wannier tight-binding model (see the SM for details [26]) and calculated the anomalous Hall effect for the three magnetic configurations shown in Fig. 7. We report σ_{xy} for the magnetic configuration with spin along the *c* axis (hard axis), and σ_{yz} for the configurations with spins along the *a* axis (easy axis) and the noncollinear phase. In the calculated energy range between −0.5 and 0.5 eV, the calculated AHC is always positive except for a negative spike present for all configurations. While for in-plane magnetic configuration this spike is at the Fermi level, for the out-of-plane magnetic configuration this negative spike is shifted by the quantity $\Delta E_{\rm WP}$ deriving from the band structure effects. This implies that the change of the magnetization from the *a* to the *c* axis plays a

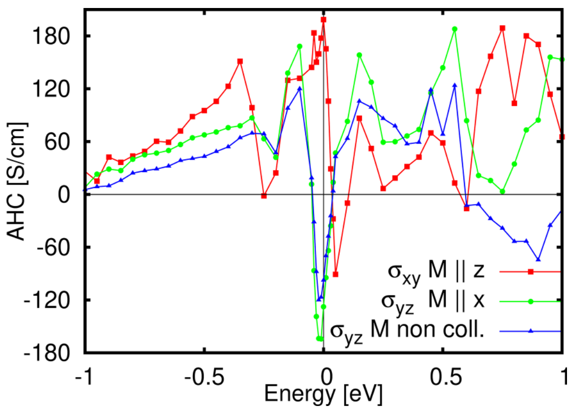

FIG. 7. Calculated intrinsic anomalous Hall conductivity for the collinear ferromagnetic configuration with spins along the a axis (green with circle points), along the c axis (red with square points), and in the noncollinear magnetic configuration (blue with triangle points). The energy range is between -1 and $+1$ eV. The Fermi level is set to zero for all three magnetic configurations.

role in inverting the sign of the anomalous Hall conductivity. The AHC is positive for the out-of-plane magnetic field and negative for the in-plane magnetic field in agreement with the experimental results reported in Fig. 5(a). The presence of consecutive and negative large values of the Berry curvature is a signature of the Weyl points; indeed, in a simplified Weyl points model, the Berry curvature goes from being strongly positive to strongly negative when you go from below to above the Weyl points [51] (see part D of the SM [26]). Hence, the sign change of AHE comes directly from the presence of the **k**-space topology (Weyl points) close to the Fermi level.

Our theoretical results developed at low temperatures could be qualitatively valid also above T_C, where the magnetization rotates from the easy axis towards the axis of the applied strong magnetic field. Since the Weyl points at the Fermi level do not come from $4f$-electron bands, we expect that AHE is weakly dependent if the induced magnetic moment on $5d$ electrons comes from the $4f$-Ce intrinsic magnetic moment or from the external magnetic field. Therefore, the AHE above Curie temperature can be large too and AHE below and above T_C can be of the same order of magnitude. Therefore, the large AHE in the paramagnetic phase emerges due to the presence of the **k**-space topology (Weyl points) close to the Fermi level. Indeed, the Weyl points are close to the Fermi level giving a large contribution even in the presence of the external magnetic field.

(ii) In the paramagnetic phase, the anomalous Hall conductivity for $B||a$ (σ_{yz}^A) decreases with increasing temperature and practically vanishes at room temperature. On the contrary, the anomalous Hall conductivity for $B||c$ (σ_{xy}^A) goes through a maximum at $T \approx 170$ K [see Fig. 5(a)], and reaches higher values than in the FM phase. The corresponding anomalous Nernst conductivity (ANC, α_{xy}^A/T) slowly decreases with increasing temperature [see Fig. 5(b)].

It is worth noting here that a sizeable anomalous response was already reported in other nonmagnetic topological materials [52,53]. The lack of correlation between magnetization and the ANE was even used to indicate that the observed phenomenon is due to nonzero Berry curvature [44]. In topological semimetals the AHE as well as the ANE originate from large Berry curvature generated by Weyl nodes and their presence in the paramagnetic phase of CeAlSi was recently confirmed experimentally [22]. In the presence of a finite Berry curvature, σ_{xy}^A and α_{xy}^A can be calculated as [53,54]

$$\sigma_{xy}^A = \frac{e^2}{\hbar} \sum_n \int \frac{d^3k}{(2\pi)^3} \Omega_{xy}^n f_n, \tag{8}$$

$$\alpha_{xy}^A = -\frac{1}{T}\frac{e}{\hbar} \sum_n \int \frac{d^3k}{(2\pi)^3} \Omega_{xy}^n \bigg[(E_n - E_F) f_n + k_B T \ln\left(1 + \exp\frac{(E_n - E_F)}{-k_B T}\right)\bigg], \tag{9}$$

where f_n is the Fermi-Dirac distribution, E_F represents the Fermi energy, Ω_{xy}^n is the Berry curvature, and E_n are the eigenenergies for eigenstates n. From the above equations, a general form of ANC and AHC can be written as [51]

$$\lambda_{xy} = \frac{e^2}{\hbar} \sum_n \int \frac{d^3k}{(2\pi)^3} \Omega_{xy}^n w_\lambda (E_n - E_F) \text{ with } \lambda = \sigma, \alpha. \tag{10}$$

Hence, both anomalous conductivities are basically the product of Ω_{xy}^n and weighting factor (w), where the latter reads as [51]

$$w_\sigma(E_n - E_F) = f_n^T (E_n - E_F), \tag{11}$$

$$w_\alpha(E_n - E_F) = -\frac{1}{eT} \bigg[(E_n - E_F) f_n^T + k_B T \ln\left(1 + \exp\frac{(E_n - E_F)}{-k_B T}\right)\bigg]. \tag{12}$$

Here f_n^T is the Fermi-Dirac distribution function at a given temperature. To model the temperature dependencies of σ_{xy}^A and α_{xy}^A in the PM phase, we introduce a single-band toy model including a nonzero Berry curvature in the vicinity of the Weyl points. $\Omega_{xy}(E)$ is simplistically assumed to change linearly at the Weyl node from positive to negative (see in Fig. S4 in the SM [26]). To match the experimental results, we restricted the energy range of nonzero Ω_{xy} to F $\pm$ 25 meV, which is similar to the range reported in Ref. [51]. As for the energy distance between the Fermi level and a Weyl node, the electronic structure calculations reported by [21] for CeAlSi indicate two sets W_1 and W_2 present close to E_F, which are expected to dominate the low energy physics of this material [21]. Each set contains different Weyl points defined as $W_1^{1,2,3,4}$ and $W_2^{1,2,3,4}$. In our model, the Weyl node is placed at -20 meV away from the E_F, which is consistent with the position of the W_2 nodes [21]. The calculated energy dependencies of AHC, ANC, and w at room temperature are shown in Fig. S4 of the SM [26]. The temperature dependencies of σ_{xy}^A and α_{xy}^A/T calculated using Eqs. (8) and (9) are presented in Fig. 5 as solid lines along with the experimental data. They appear to be governed by a broadening of the Fermi function with temperature, which allows states further away from the E_F to be included in the integration [44,52,53].

Apparently, this crude approach reproduces the characteristics of the experimental data quite well, reflecting differences between energy dependencies of weighting factors for the anomalous Hall and Nernst effects. Namely, the calculated σ_{xy}^A increases up to $T \approx 170$ K, reaches a maximum, and then decreases, while α_{xy}^A/T slowly decreases with the increasing temperature at a rate similar to the one observed in the experiment. Moreover, the signs of both σ_{xy}^A and α_{xy}^A/T also match the experimental data.

V. CONCLUSION

We studied the anomalous Hall and Nernst effects in the noncollinear Weyl semimetal CeAlSi from room to low temperature. In the ferromagnetic phase, the anomalous Hall conductivity turns out to be positive for the magnetic field applied along the magnetically hard axis ($\sigma_{xy}^A > 0$) and negative for B parallel to the easy axis ($\sigma_{yz}^A < 0$). Density functional theory calculations attributed the different signs of the AHE to a shift of Weyl points along the Γ-X direction and this shift is induced by the reconstructions in the band structure driven by the magnetic configuration. In the paramagnetic phase, σ_{yz}^A significantly decreases, whereas σ_{xy}^A reaches values even higher than at the low-temperature limit. The temperature dependence of σ_{xy}^A as well as the respective Nernst conductivity (α_{xy}^A) can be well approximated using a simple model assuming the presence of a Weyl point in the vicinity of the Fermi level. Properties of the anomalous Hall and Nernst effects appear to be dominated by **k**-space topology at both low and high temperatures.

Note added. After submission of this paper, we became aware of a very recent work that also reports on the anomalous Hall and Nernst effect in CeAlSi [55].

ACKNOWLEDGMENTS

We acknowledge W. Brzezicki, R. Citro, and K. Das for the useful discussions. This work was supported by the Foundation for Polish Science through the International Research Agendas program cofinanced by the European Union within the Smart Growth Operational Programme. A.F. was supported by the Polish National Science Centre under Project No. 2020/37/B/ST5/02299. We also acknowledge the access to the computing facilities of the Interdisciplinary Center of Modeling at the University of Warsaw, Grants No. G84-0, No. GB84-1, and No. GB84-7. We acknowledge the CINECA award under the ISCRA initiative IsC93 “RATIO” and IsC99 “SILENTS” grants for the availability of high-performance computing resources and support. The work at Boston College was funded by the National Science Foundation under Award No. DMR-2203512.

[1] N. P. Armitage, E. J. Mele, and A. Vishwanath, Weyl and Dirac semimetals in three-dimensional solids, Rev. Mod. Phys. **90**, 015001 (2018).

[2] B. Yan and C. Felser, Topological materials: Weyl semimetals, Annu. Rev. Condens. Matter Phys. **8**, 337 (2017).

[3] R. Islam, B. Ghosh, G. Cuono, A. Lau, W. Brzezicki, A. Bansil, A. Agarwal, B. Singh, T. Dietl, and C. Autieri, Topological states in superlattices of HgTe class of materials for engineering three-dimensional flat bands, Phys. Rev. Research **4**, 023114 (2022).

[4] A. S. Wadge, B. J. Kowalski, C. Autieri, P. Iwanowski, A. Hruban, N. Olszowska, M. Rosmus, J. Kołodziej, and A. Wiśniewski, Topological Lifshitz transition in Weyl semimetal NbP decorated with heavy elements, Phys. Rev. B **105**, 235304 (2022).

[5] X. Wan, A. M. Turner, A. Vishwanath, and S. Y. Savrasov, Topological semimetal and Fermi-arc surface states in the electronic structure of pyrochlore iridates, Phys. Rev. B **83**, 205101 (2011).

[6] X. Huang, L. Zhao, Y. Long, P. Wang, D. Chen, Z. Yang, H. Liang, M. Xue, H. Weng, Z. Fang, X. Dai, and G. Chen, Observation of the Chiral-Anomaly-Induced Negative Magnetoresistance: In 3D Weyl Semimetal TaAs, Phys. Rev. X **5**, 031023 (2015).

[7] J. Xiang, S. Hu, Z. Song, M. Lv, J. Zhang, L. Zhao, W. Li, Z. Chen, S. Zhang, J. T. Wang, Y. F. Yang, X. Dai, F. Steglich, G. Chen, and P. Sun, Giant Magnetic Quantum Oscillations in the Thermal Conductivity of TaAs: Indications of Chiral Zero Sound, Phys. Rev. X **9**, 031036 (2019).

[8] P. K. Tanwar, M. S. Alam, M. Ahmad, D. Kaczorowski, and M. Matusiak, Severe violation of the Wiedemann-Franz law in quantum oscillations of NbP, Phys. Rev. B **106**, L041106 (2022).

[9] I. Belopolski, K. Manna, D. S. Sanchez, G. Chang, B. Ernst, J. Yin, S. S. Zhang, T. Cochran, N. Shumiya, H. Zheng, B. Singh, G. Bian, D. Multer, M. Litskevich, X. Zhou, S. M. Huang, B. Wang, T. R. Chang, S. Y. Xu, A. Bansil *et al.*, Discovery of topological Weyl fermion lines and drumhead surface states in a room temperature magnet, Science **365**, 1278 (2019).

[10] K. Kim, J. Seo, E. Lee, K. T. Ko, B. S. Kim, B. G. Jang, J. M. Ok, J. Lee, Y. J. Jo, W. Kang, J. H. Shim, C. Kim, H. W. Yeom, B. Il Min, B. J. Yang, and J. S. Kim, Large anomalous Hall current induced by topological nodal lines in a ferromagnetic van der Waals semimetal, Nat. Mater. **17**, 794 (2018).

[11] H. B. Noam Morali, R. Batabyal, P. K. Nag, E. Liu, Q. Xu, Y. Sun, B. Yan, C. Felser, and N. Avraham, Fermi-arc diversity on surface terminations of the magnetic Weyl semimetal $Co_3Sn_2S_2$, Science **365**, 1286 (2019).

[12] E. Liu, Y. Sun, N. Kumar, L. Muechler, A. Sun, L. Jiao, S. Y. Yang, D. Liu, A. Liang, Q. Xu, J. Kroder, V. Süß, H. Borrmann, C. Shekhar, Z. Wang, C. Xi, W. Wang, W. Schnelle, S. Wirth, Y. Chen, S. T. B. Goennenwein, and C. Felser, Giant anomalous Hall effect in a ferromagnetic kagome-lattice semimetal, Nat. Phys. **14**, 1125 (2018).

[13] Y. Yao, L. Kleinman, A. H. MacDonald, J. Sinova, T. Jungwirth, D. sheng Wang, E. Wang, and Q. Niu, First Principles Calculation of Anomalous Hall Conductivity in Ferromagnetic bcc Fe, Phys. Rev. Lett. **92**, 037204 (2004).

[14] J. Gaudet, H. Y. Yang, S. Baidya, B. Lu, G. Xu, Y. Zhao, J. A. Rodriguez-Rivera, C. M. Hoffmann, D. E. Graf, D. H. Torchinsky, P. Nikolić, D. Vanderbilt, F. Tafti, and

C. L. Broholm, Weyl-mediated helical magnetism in NdAlSi, Nat. Mater. **20**, 1650 (2021).

[15] R. Yang and M. Corasaniti, Charge dynamics of a noncentrosymmetric magnetic Weyl semimetal, npj Quantum Mater. **7**, 101 (2022).

[16] P. Li, J. Koo, W. Ning, J. Li, L. Miao, L. Min, Y. Zhu, Y. Wang, N. Alem, C. X. Liu, Z. Mao, and B. Yan, Giant room temperature anomalous Hall effect and tunable topology in a ferromagnetic topological semimetal Co_2MnAl, Nat. Commun. **11**, 3476 (2020).

[17] K. Geishendorf, P. Vir, C. Shekhar, C. Felser, J. I. Facio, J. Van Den Brink, K. Nielsch, A. Thomas, and S. T. B. Goennenwein, Signatures of the magnetic entropy in the thermopower signals in nanoribbons of the magnetic Weyl semimetal $Co_3Sn_2S_2$, Nano Lett. **20**, 300 (2020).

[18] S. Itoh, Y. Endoh, T. Yokoo, S. Ibuka, J. G. Park, Y. Kaneko, K. S. Takahashi, Y. Tokura, and N. Nagaosa, Weyl fermions and spin dynamics of metallic ferromagnet $SrRuO_3$, Nat. Commun. **7**, 11788 (2016).

[19] D. J. Groenendijk, C. Autieri, T. C. Van Thiel, W. Brzezicki, J. R. Hortensius, D. Afanasiev, N. Gauquelin, P. Barone, K. H. W. Van Den Bos, S. Van Aert, J. Verbeeck, A. Filippetti, S. Picozzi, M. Cuoco, and A. D. Caviglia, Berry phase engineering at oxide interfaces, Phys. Rev. Res. **2**, 023404 (2020).

[20] T. C. Van Thiel, W. Brzezicki, C. Autieri, J. R. Hortensius, D. Afanasiev, N. Gauquelin, D. Jannis, N. Janssen, D. J. Groenendijk, J. Fatermans, S. Van Aert, J. Verbeeck, M. Cuoco, and A. D. Caviglia, Coupling Charge and Topological Reconstructions at Polar Oxide Interfaces, Phys. Rev. Lett. **127**, 127202 (2021).

[21] H. Y. Yang, B. Singh, J. Gaudet, B. Lu, C. Y. Huang, W. C. Chiu, S. M. Huang, B. Wang, F. Bahrami, B. Xu, J. Franklin, I. Sochnikov, D. E. Graf, G. Xu, Y. Zhao, C. M. Hoffman, H. Lin, D. H. Torchinsky, C. L. Broholm, A. Bansil, and F. Tafti, Noncollinear ferromagnetic Weyl semimetal with anisotropic anomalous Hall effect, Phys. Rev. B **103**, 115143 (2021).

[22] A. P. Sakhya, C. Huang, G. Dhakal, X. Gao, S. Regmi, X. Yao, R. Smith, M. Sprague, and B. Singh, Observation of Fermi arcs and Weyl nodes in a non-centrosymmetric magnetic Weyl semimetal, arXiv:2203.05440.

[23] M. M. Piva, J. C. Souza, V. Brousseau-Couture, K. R. Pakuszewski, J. K. John, C. Adriano, M. Côté, P. G. Pagliuso, and M. Nicklas, Tuning the nontrivial topological properties of the Weyl semimetal CeAlSi, arXiv:2111.05742.

[24] C. M. Hurd, *The Hall Effect in Metals and Alloys*, International Cryogenics Monograph Series (Springer, Berlin, 1972).

[25] M. S. Alam, P. K. Tanwar, K. Dybko, A. S. Wadge, P. Iwanowski, A. Wiśniewski, and M. Matusiak, Temperature-driven spin-zero effect in $TaAs_2$, J. Phys. Chem. Solids **170**, 110939 (2022).

[26] See Supplemental Material at http://link.aps.org/supplemental/10.1103/PhysRevB.107.085102 for additional experimental data, modeled anomalous Hall and Nernst conductivities in the presence of nonzero Berry curvature, and a detailed discussion of band structure calculations.

[27] G. Kresse and J. Hafner, *Ab initio* molecular dynamics for liquid metals, Phys. Rev. B **47**, 558 (1993).

[28] G. Kresse and J. Furthmüller, Efficient iterative schemes for ab initio total-energy calculations using a plane-wave basis set, Phys. Rev. B **54**, 11169 (1996).

[29] W. E. Pickett, Implementation of the LDA + U method using the full-potential linearized augmented plane-wave basis, Phys. Rev. B **60**, 10763 (1999).

[30] A. A. Mostofi, J. R. Yates, G. Pizzi, Y. S. Lee, I. Souza, D. Vanderbilt, and N. Marzari, An updated version of WANNIER90: A tool for obtaining maximally-localised wannier functions, Comput. Phys. Commun. **185**, 2309 (2014).

[31] M. Zeer, D. Go, J. P. Carbone, T. G. Saunderson, M. Redies, M. Kläui, J. Ghabboun, W. Wulfhekel, S. Blügel, and Y. Mokrousov, Spin and orbital transport in rare-earth dichalcogenides: The case of EuS_2, Phys. Rev. Mater. **6**, 074004 (2022).

[32] W. Cao, Y. Su, Q. Wang, C. Pei, L. Gao, Y. Zhao, C. Li, N. Yu, J. Wang, Z. Liu, Y. Chen, G. Li, J. Li, and Y. Qi, Quantum oscillations in noncentrosymmetric Weyl semimetal SmAlSi, Chin. Phys. Lett. **39**, 047501 (2022).

[33] N. Nagaosa, J. Sinova, S. Onoda, A. H. MacDonald, and N. P. Ong, Anomalous Hall effect, Rev. Mod. Phys. **82**, 1539 (2010).

[34] K. S. Takahashi, H. Ishizuka, T. Murata, Q. Y. Wang, Y. Tokura, N. Nagaosa, and M. Kawasaki, Anomalous Hall effect derived from multiple Weyl nodes in high-mobility $EuTiO_3$ films, Sci. Adv. **4**, eaar7880 (2018).

[35] M. Tanaka, Y. Fujishiro, M. Mogi, Y. Kaneko, T. Yokosawa, N. Kanazawa, S. Minami, T. Koretsune, R. Arita, S. Tarucha, M. Yamamoto, and Y. Tokura, Topological kagome magnet $Co_3Sn_2S_2$ thin flakes with high electron mobility and large anomalous Hall effect, Nano Lett. **20**, 7476 (2020).

[36] B. Meng, H. Wu, Y. Qiu, C. Wang, Y. Liu, Z. Xia, S. Yuan, H. Chang, and Z. Tian, Large anomalous Hall effect in ferromagnetic Weyl semimetal candidate PrAlGe, APL Mater. **7**, 051110 (2019).

[37] J. F. Wang, Q. X. Dong, Z. P. Guo, M. Lv, Y. F. Huang, J. Sen Xiang, Z. A. Ren, Z. J. Wang, P. J. Sun, G. Li, and G. F. Chen, NdAlSi: A magnetic Weyl semimetal candidate with rich magnetic phases and atypical transport properties, Phys. Rev. B **105**, 144435 (2022).

[38] S. Onoda, N. Sugimoto, and N. Nagaosa, Intrinsic versus Extrinsic Anomalous Hall Effect in Ferromagnets, Phys. Rev. Lett. **97**, 126602 (2006).

[39] L. Berger, Side-jump mechanism for the Hall effect of ferromagnets, Phys. Rev. B **2**, 4559 (1970).

[40] A. A. Burkov, Anomalous Hall Effect in Weyl Metals, Phys. Rev. Lett. **113**, 187202 (2014).

[41] A. Sekine, D. Culcer, and A. H. MacDonald, Quantum kinetic theory of the chiral anomaly, Phys. Rev. B **96**, 235134 (2017).

[42] G. Chang, B. Singh, S. Y. Xu, G. Bian, S. M. Huang, C. H. Hsu, I. Belopolski, N. Alidoust, D. S. Sanchez, H. Zheng, H. Lu, X. Zhang, Y. Bian, T. R. Chang, H. T. Jeng, A. Bansil, H. Hsu, S. Jia, T. Neupert, H. Lin, and M. Z. Hasan, Magnetic and noncentrosymmetric Weyl fermion semimetals in the RAlGe family of compounds (R = Rare Earth), Phys. Rev. B **97**, 041104(R) (2018).

[43] T. Liang, Q. Gibson, J. Xiong, M. Hirschberger, S. P. Koduvayur, R. J. Cava, and N. P. Ong, Evidence for massive bulk Dirac fermions in $Pb_{1-x}Sn_xSe$ from Nernst and thermopower experiments, Nat. Commun. **4**, 2696 (2013).

[44] T. Liang, J. Lin, Q. Gibson, T. Gao, M. Hirschberger, M. Liu, R. J. Cava, and N. P. Ong, Anomalous Nernst Effect in the Dirac Semimetal Cd_3As_2, Phys. Rev. Lett. **118**, 136601 (2017).

[45] J. Hu, B. Ernst, S. Tu, M. KuveŽdić, A. Hamzić, E. Tafra, M. Basletić, Y. Zhang, A. Markou, C. Felser, A. Fert, W. Zhao,

J. P. Ansermet, and H. Yu, Anomalous Hall and Nernst Effects in Co_2TiSn and $Co_2Ti_{0.6}V_{0.4}Sn$ Heusler Thin Films, Phys. Rev. Appl. **10**, 044037 (2018).

[46] Y. Pu, D. Chiba, F. Matsukura, H. Ohno, and J. Shi, Mott Relation for Anomalous Hall and Nernst Effects in $Ga_{1-x}Mn_xAs$ Ferromagnetic Semiconductors, Phys. Rev. Lett. **101**, 117208 (2008).

[47] D. Xiao, Y. Yao, Z. Fang, and Q. Niu, Berry-Phase Effect in Anomalous Thermoelectric Transport, Phys. Rev. Lett. **97**, 026603 (2006).

[48] A. K. Nayak, J. E. Fischer, Y. Sun, B. Yan, J. Karel, A. C. Komarek, C. Shekhar, N. Kumar, W. Schnelle, J. Kübler, C. Felser, and S. S. P. Parkin, Large anomalous Hall effect driven by a nonvanishing berry curvature in the noncolinear antiferromagnet Mn_3Ge, Sci. Adv. **2**, e1501870 (2016).

[49] R. Di Capua, M. Verma, M. Radovic, V. N. Strocov, C. Piamonteze, E. B. Guedes, N. C. Plumb, Y. Chen, M. D'Antuono, G. M. De Luca, E. Di Gennaro, D. Stornaiuolo, D. Preziosi, B. Jouault, F. Miletto Granozio, A. Sambri, R. Pentcheva, G. Ghiringhelli, and M. Salluzzo, Orbital selective switching of ferromagnetism in an oxide quasi two-dimensional electron gas, npj Quantum Mater. **7**, 41 (2022).

[50] M. Yao, H. Lee, N. Xu, Y. Wang, J. Ma, O. V. Yazyev, Y. Xiong, M. Shi, G. Aeppli, and Y. Soh, Switchable Weyl nodes in topological kagome ferromagnet Fe_3Sn_2, arXiv:1810.01514.

[51] J. Noky, J. Gooth, C. Felser, and Y. Sun, Characterization of topological band structures away from the Fermi level by the anomalous Nernst effect, Phys. Rev. B **98**, 241106(R) (2018).

[52] T. Liang, J. Lin, Q. Gibson, S. Kushwaha, M. Liu, W. Wang, H. Xiong, J. A. Sobota, M. Hashimoto, P. S. Kirchmann, Z. X. Shen, R. J. Cava, and N. P. Ong, Anomalous Hall effect in $ZrTe_5$, Nat. Phys. **14**, 451 (2018).

[53] F. Caglieris, C. Wuttke, S. Sykora, V. Süss, C. Shekhar, C. Felser, B. Büchner, and C. Hess, Anomalous Nernst effect and field-induced Lifshitz transition in the Weyl semimetals TaP and TaAs, Phys. Rev. B **98**, 201107(R) (2018).

[54] D. Xiao, M. C. Chang, and Q. Niu, Berry phase effects on electronic properties, Rev. Mod. Phys. **82**, 1959 (2010).

[55] E. Cheng, L. Yan, X. Shi, M. Behnami, J. Yuan, Y. Xu, Y. Xu, Y. Wan, W. Xia, N. Pavlovskii, D. C. Peets, W. Zhao, Y. Guo, S. Li, W. Yang, and B. Büchner, Anomalous transverse transport and phase transitions in Weyl semimetals RAlSi (R = La, Ce), arXiv:2301.03800.

Correction: The units shown on the y axis of the previously published Figure 5(b) were incorrect. The figure has been replaced.

Supplemental material:

Sign change of the anomalous Hall effect and the anomalous Nernst effect in Weyl semimetal CeAlSi

Md Shahin Alam [1,*], Amar Fakhredine [2], Mujeeb Ahmed [1], P.K. Tanwar [1], Hung-Yu Yang [3], Fazel Tafti [3], Giuseppe Cuono [1], Rajibul Islam [1], Bahadur Singh [4], Artem Lynnyk [2], Carmine Autieri [1,†], Marcin Matusiak [1,5,‡]

1. *International Research Centre MagTop, Institute of Physics, Polish Academy of Sciences, Aleja Lotników 32/46, PL-02668 Warsaw, Poland*
2. *Institute of Physics, Polish Academy of Sciences, Aleja Lotników 32/46, PL-02668 Warsaw, Poland*
3. *Department of Physics, Boston College, Chestnut Hill, Massachusetts 02467, USA*
4. *Department of Condensed Matter Physics and Materials Science, Tata Institute of Fundamental Research, Mumbai 400005, India*
5. *Institute of Low Temperature and Structure Research, Polish Academy of Sciences, ul. Okólna 2, 50-422 Wrocław, Poland*

A: Non-anomalous fits of the magnetic field dependences

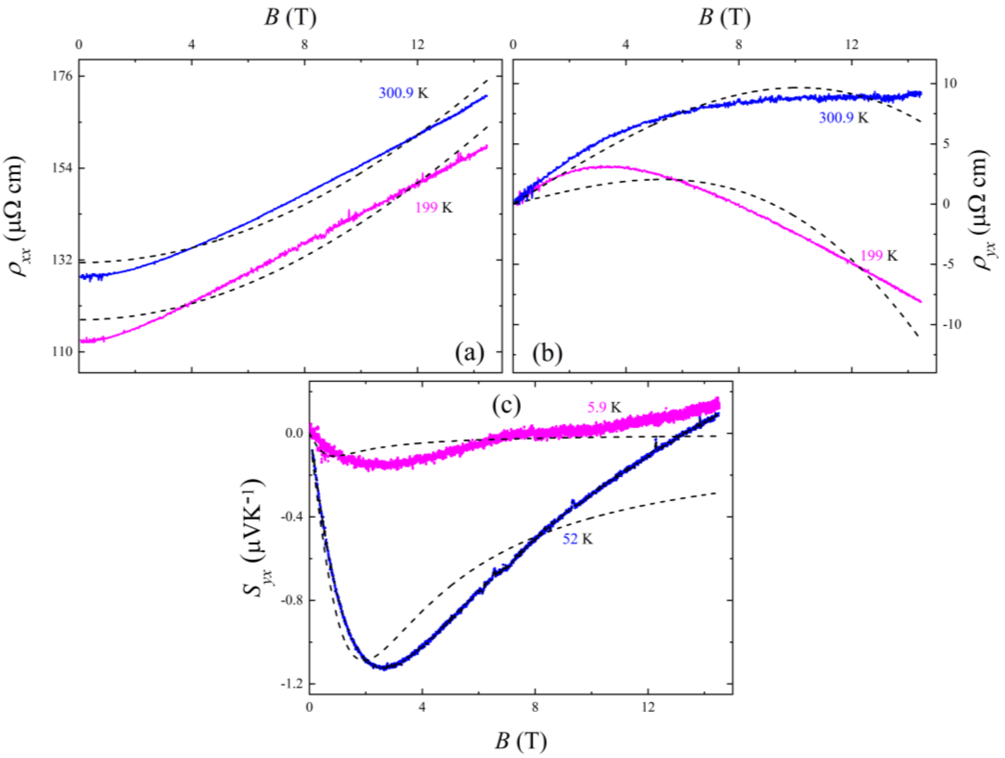

Figure S1. (a & b) Magnetic field dependences of the longitudinal resistivity (ρ_{xx}) and Hall resistivity (ρ_{yx}) for T = 199 K (magenta) and 300.9 K (blue) for CeAlSi. The black dashed lines indicate the best simultaneous fits using the semi-classical two band approximation [1]. There is an apparent discrepancy between the experimental data and the model. (c) Nernst signal (S_{yx}) as a function of B. Black dashed lines represent fits to: $S_{yx}^N = S_0^N \frac{\mu}{1+(\mu B)^2}$ (see main text), which poorly matches the experimental data.

B: Scaling of anomalous Hall resistivity

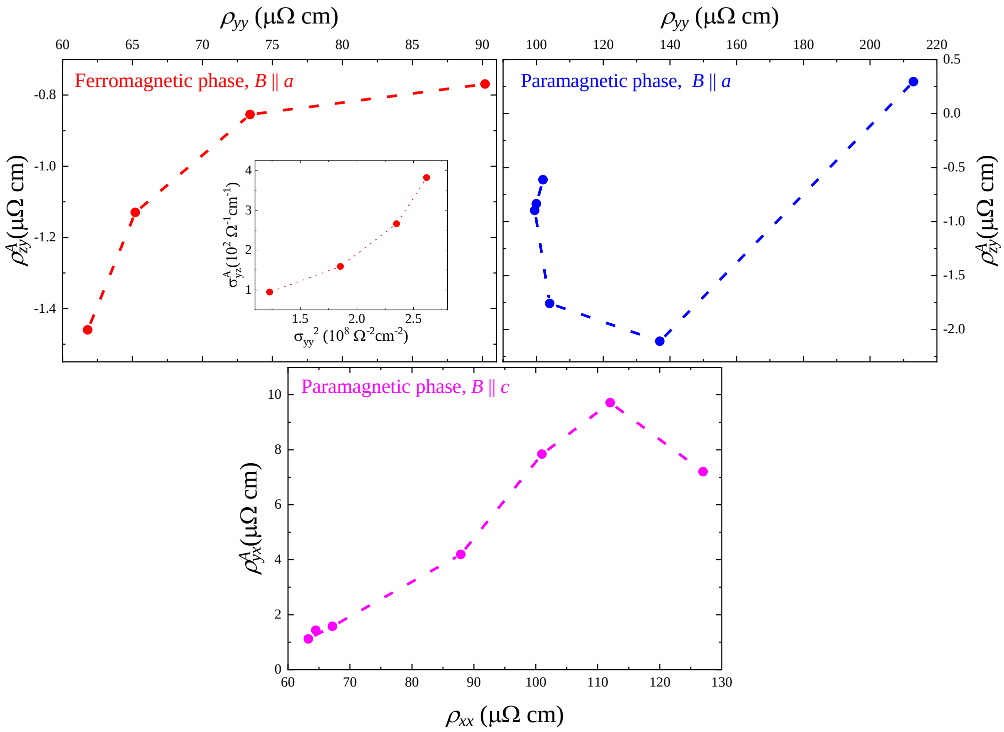

Figure S2. (a) The anomalous Hall resistivity (ρ_{zy}^{A}) in ferromagnetic phase of CeAlSi plotted versus longitudinal resistivity (ρ_{yy}) for $B \parallel a$. Inset shows the anomalous Hall conductivity (σ_{yz}^{A}) as a function of the square of the longitudinal conductivity (σ_{yy}^{2}) (b) ρ_{zy}^{A} vs ρ_{yy} for $B \parallel a$ in paramagnetic phase. (c) The anomalous Hall resistivity (ρ_{yx}^{A}) versus the longitudinal resistivity (ρ_{xx}) for $B \parallel c$, in paramagnetic phase.

C: Magnetic measurements

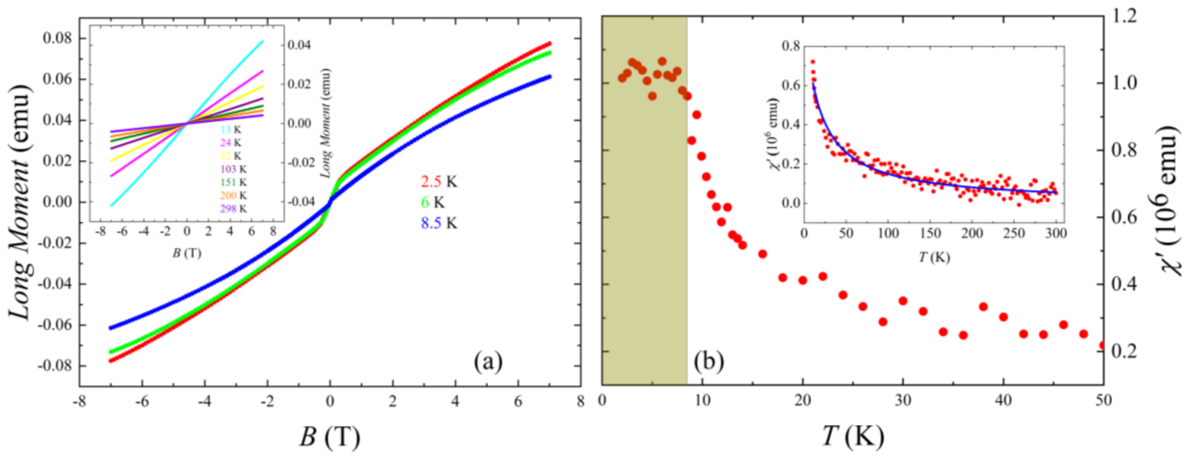

Figure S3. (a) Magnetic field dependences of the longitudinal magnetic moments in ferromagnetic phase of CeAlSi. Inset shows long magnetic moment as a function of B in the paramagnetic phase. (b) Temperature dependence of the magnetic susceptibility (χ') with the ferromagnetic region marked in dark yellow. Inset shows χ' vs T (red points) in the paramagnetic phase fitted to the Curie-Weiss law (solid blue line).

D: Anomalous Hall and Nernst conductivities in presence of non-zero Berry curvature

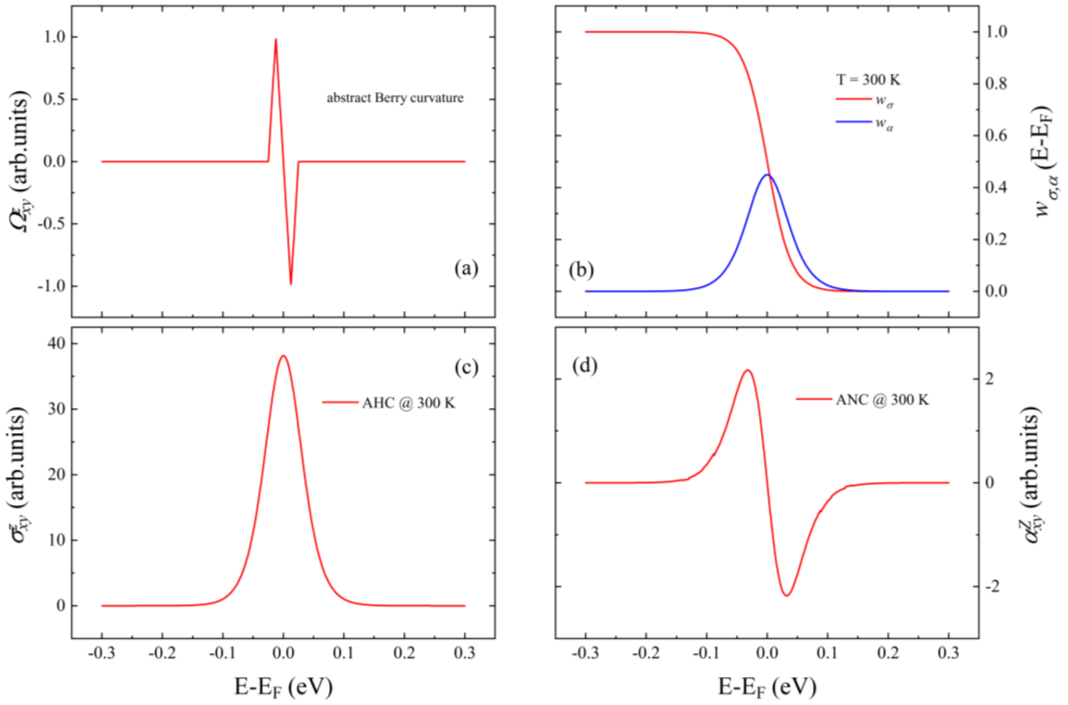

Figure S4. (a) Imaginary Berry curvature (Ω_{xy}^{z}) in arbitrary units plotted versus energy near the Fermi level. (b) Weighting function (ω) for the anomalous Hall conductivity (red) and the transverse thermoelectrical conductivity (blue) as a function of energy at T = 300 K. (c) Energy dependences of the anomalous Hall conductivity at T = 300 K, calculated as a product of Ω_{xy}^{z} and weighting function w_σ. (d) Anomalous Nernst conductivity as a function of energy T = 300 K calculated as a product of Ω_{xy}^{z} and weighting function w_α.

E: Computational details for Density functional theory

First-principles calculations were conducted and the projector-augmented-wave (PAW) method was applied. The generalized gradient approximation of the Perdew-Burke-Ernzerhof(PBE) form was used to treat the exchange-correlation energy (GGA), as implemented in the Vienna ab-initio simulation package (VASP) in the frame of the density functional theory [2,3]. The cut-off energies for the plane-wave basis set that were used to expand the Kohn-Sham orbitals were chosen to be 450 eV. All calculations include the spin-orbit coupling. The Monkhorst-Pack scheme was used for the Γ-centered10×10×10 k-point sampling. The calculations are performed using the experimental lattice parameters of CeAlsi (a = 4.252 Å; c = 14.5801 Å) [4]. In order to conduct the effect of strongly correlated electrons in the 4f-shell of Ce, we applied the GGA+U method within the self-consistent DFT cycle [5]. The on-site Coulomb interaction strength U applied to the Ce 4f states is 7 eV and the intra-atomic exchange interaction strength J_H was taken as zero. Our ab-initio results were utilized to obtain the Wannier tight-binding Hamiltonian using the VASP2WANNIER90 interface [6]. The Anomalous Hall Effect was calculated subsequently after applying the technique of Wannier interpolation [7] using a k-grid of 100 x 100 x 100 with an adaptive grid of 5 x 5 x 5. The AHE calculations were verified with a k-grid of 300 x 300 x 300 that reproduce the same results with negligible differences. The calculations were performed on three different spin configurations of the CeAlSi unit cell; a collinear FM phase with the spins aligned along the x-axis direction, a collinear FM phase with the spins aligned along the z-axis direction, and a non-collinear FM ordering. All the AHE calculations reproduce a minimum and a maximum close to the Fermi level, therefore the AHE results are robust respect to the wannierization of the three different magnetic configurations.

For better analysis of the electronic structure of CeAlSi, the atom-resolved local density of states (LDOS) was also calculated for the non-collinear ferromagnetic configuration with spin-orbit coupling (SOC) and presented in Figure 8. DOS for other magnetic configurations are qualitatively similar. The sp-bands of Al and Si are present both below and above the Fermi level. One band of the Ce 4f-states is present at -3 eV from the Fermi level, while the other Ce 4f-states are above 2 eV from the Fermi level. The sp-orbitals of Ce are less relevant, while close to the Fermi level, the only relevant contribution from the Ce atoms comes from the 5d-states.

The oxidation states of atoms is zero in this compound. The electronic configuration for Ce reported in textbooks is $[Xe]4f^1 5d^1 6s^2$ in the ionic approximation, this electronic configuration can change depending on the structural phases and crystal fields. In CeAlsi, the electronic configuration changes to be something more similar to $4f^1 5d^3 6s^0$ in the ionic approximation according to our local DOS. Indeed, due to the crystal field effect of the surrounding atoms that act differently on d-electrons and on s-electrons, the s-electrons of Ce are pushed to higher energies. Since we are only interested in the electronic properties at the Fermi level, we have approximated the Ce atom as $[Xe]4f^1 5d^3 6s^0$ considering that only the 5d electrons are relevant for the wannierization and excluding the 4f electrons from our tight-binding model. For this reason, the wannierization was performed taking into consideration the sp-electrons of Al , sp-electrons of Si and the d-electrons of Ce as tight-binding basis. Within its simplicity, this approximation brings us to a quite good result of the wannierization. We have chosen the frozen window around the Fermi level excluding the 4f states in both conduction and valence band. Our wannierization is in agreement with that reported in the literature [8].

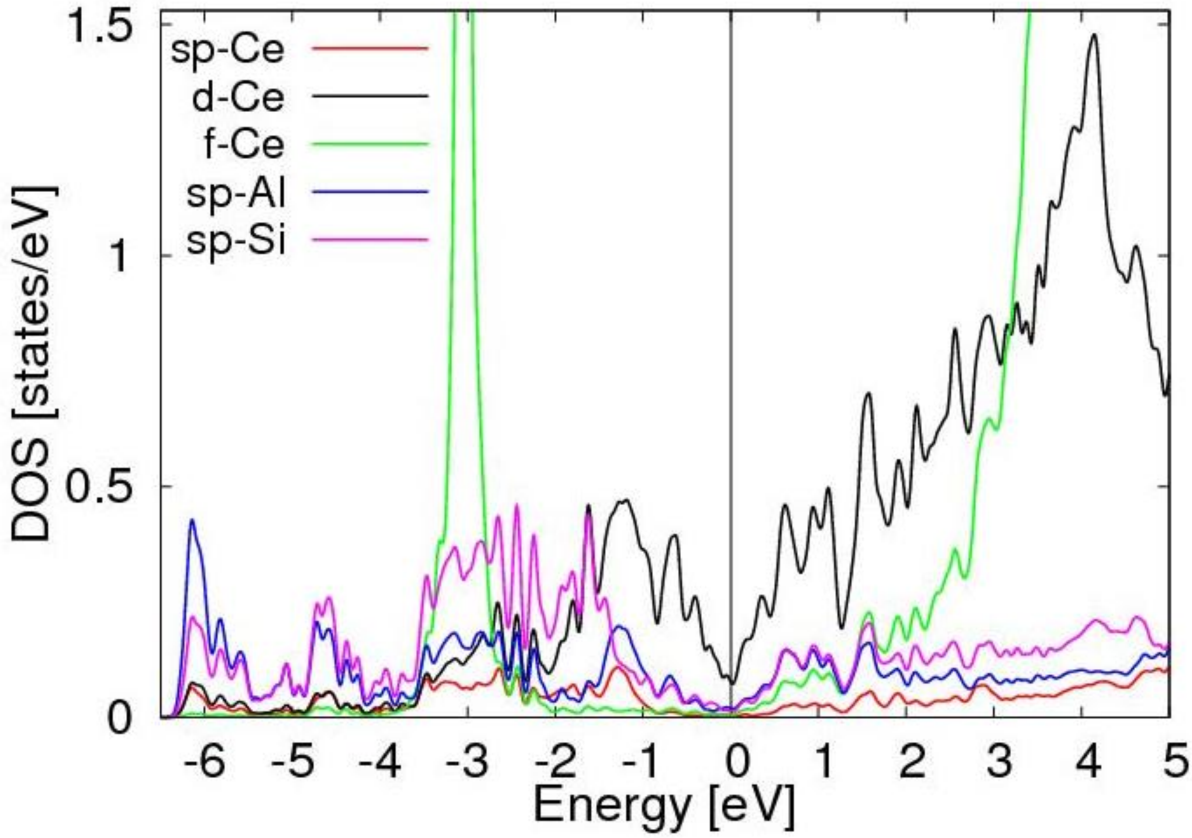

Figure S5. Local density of states for the non-collinear magnetic configuration of CeAlSi. The 4f-levels of Ce are extremely localized and their DOS goes beyond the maximum of the y-range. The Fermi level is set to zero.

References

[1] C. M. Hurd, *The Hall Effect in Metals and Alloys, The International Cryogenics Monograph Series, Springer, Berlin* (1972). DOI: https://doi.org/10.1007/978-1-4757-0465-5_8

[2] G. Kresse and J. Hafner, *Ab Initio Molecular Dynamics for Liquid Metals*, Phys. Rev. B **47**, 558 (1993). DOI: https://doi.org/10.1103/PhysRevB.47.558

[3] G. Kresse and J. Furthmüller, *Efficient Iterative Schemes for Ab Initio Total-Energy Calculations Using a Plane-Wave Basis Set*, Phys. Rev. B - Condens. Matter Mater. Phys. **54**, 11169 (1996). DOI: https://doi.org/10.1103/PhysRevB.54.11169

[4] H. Y. Yang, B. Singh, J. Gaudet, B. Lu, C. Y. Huang, W. C. Chiu, S. M. Huang, B. Wang, F. Bahrami, B. Xu, J. Franklin, I. Sochnikov, D. E. Graf, G. Xu, Y. Zhao, C. M. Hoffman, H. Lin, D. H. Torchinsky, C. L. Broholm, A. Bansil, and F. Tafti, *Noncollinear Ferromagnetic Weyl Semimetal with Anisotropic Anomalous Hall Effect*, Phys. Rev. B **103**, 115143 (2021). DOI: https://doi.org/10.1103/PhysRevB.103.115143

[5] W. E. Pickett, *Implementation of the Lda+u Method Using the Full-Potential Linearized Augmented Plane-Wave Basis*, Phys. Rev. B - Condens. Matter Mater. Phys. **60**, 10763 (1999). DOI: https://doi.org/10.1103/PhysRevB.60.10763

[6] A. A. Mostofi, J. R. Yates, G. Pizzi, Y. S. Lee, I. Souza, D. Vanderbilt, and N. Marzari, *An Updated Version of Wannier90: A Tool for Obtaining Maximally-Localised Wannier Functions*, Comput. Phys. Commun. **185**, 2309 (2014). DOI: https://doi.org/10.1016/j.cpc.2007.11.016

[7] M. Zeer, D. Go, J. P. Carbone, T. G. Saunderson, M. Redies, M. Kläui, J. Ghabboun, W. Wulfhekel, S. Blügel, and Y. Mokrousov, *Spin and Orbital Transport in Rare-Earth Dichalcogenides: The Case of EuS2*, Phys. Rev. Mater. **6**, 074004 (2022). DOI: https://doi.org/10.1103/PhysRevMaterials.6.074004

[8] M. M. Piva, J. C. Souza, V. Brousseau-Couture, K. R. Pakuszewski, J. K. John, C. Adriano, M. Côté, P. G. Pagliuso, and M. Nicklas, *Tuning the Nontrivial Topological Properties of the Weyl Semimetal CeAlSi*, ArXiv:2111.05742 1 (2021). DOI: https://doi.org/10.48550/arXiv.2111.05742

3.1.3 ARTICLE III: Chiral anomaly

The electronic structure of topological Dirac semimetals contains fourfold degenerate Dirac cones, which can be split into a pair of Weyl cones by breaking either the SI or the TRS. An exotic phenomenon known as chiral anomaly can occur in these materials when a parallel electric field or thermal gradient is applied along with the magnetic field [32,53]. This should manifest macroscopically as an additional electrical current but its detection by electrical measurements has been a cause for concern. This is due to possible contributions from extrinsic phenomena such as the current jetting effect [77]. On the contrary, thermoelectric measurements offer the possibility to study the aforementioned phenomena free from artefacts [53]. In this study, we have chosen a topological Dirac semimetal α-Sn in a form of a strained thin film, whose electronic structure contains a pair of Dirac cones that are protected by fourfold rotational and time-reversal symmetries [28]. The latter can be broken by the application of a magnetic field, making α-Sn a Weyl semimetal that is a suitable candidate for the observation of the aforementioned quantum anomaly. The expected consequences of its appearance include a negative magnetoresistance or a negative slope of the magneto-thermopower in the presence of a magnetic field parallel to the electric current or thermal gradient. Indeed, we have observed both characteristics in α-Sn at low temperatures. The anomalous behavior is expected to disappear rapidly when the magnetic field is tilted away from the applied current or thermal gradient, and we have again confirmed this by angle dependent measurements. The calculated ratio of the intervalley relaxation time to the Drude scattering time indicates that α-Sn at low temperature is in fact in the chiral regime.

Quantum transport properties of the topological Dirac Semimetal α-Sn

Md Shahin Alam [1,*], Alexandr Kazakov [1], Mujeeb Ahmad [1] , Rajibul Islam [2], Fei Xue [2] , and Marcin Matusiak [1,3,†]

1. International Research Centre MagTop, Institute of Physics, Polish Academy of Sciences, Aleja Lotników 32/46, PL-02668 Warsaw, Poland
2. Department of Physics, University of Alabama at Birmingham, Birmingham, Alabama 35294, USA
3. Institute of Low Temperature and Structure Research, Polish Academy of Sciences, ulica Okólna 2, 50-422 Wrocław, Poland

We report measurements of the electrical resistivity (ρ) and thermoelectric power (S) in a thin film of strained single-crystalline α-Sn grown by molecular beam epitaxy on an insulating substrate. The temperature (T) dependence of the resistivity of α-Sn can be divided into two regions: below $T^* \approx 135$ K $\rho(T)$ shows a metallic-like behaviour, while above this temperature an increasing contribution from thermally excited holes to electrical transport is observed. However, it is still dominated by highly mobile electrons, resulting in a negative sign of the Seebeck coefficient above $T = 47$ K. In the presence of the magnetic field (B) applied along an electric field or thermal gradient, we note a negative magnetoresistance or a negative slope of $S(B)$, respectively. The theoretical prediction for the former (calculated using density functional theory) agrees well with the experiment. However, these characteristics quickly disappear when the magnetic field is deviated from an orientation parallel to the electrical field or the thermal gradient. We indicate that the behaviour of the electrical resistivity and thermoelectric power can be explained in terms of the chiral current arising from the topologically non-trivial electronic structure of α-Sn. Its decay at high temperature is a consequence of the decreasing ratio between the intervalley Weyl relaxation time to the Drude scattering time.

[*] shahin@magtop.ifpan.edu.pl, [†] m.matusiak@intibs.pl

1. Introduction

Over the past two decades, topological quantum materials have gained significant attention due to their nontrivial momentum-space topology [1–4]. For example, the Dirac semimetals, which could be considered three-dimensional analogues to the graphene, host four-fold-degenerate Dirac points protected by topological constraints [5–7]. Dirac nodes split into two chirally distinct Weyl nodes when at least one of the symmetries protecting the Dirac cone gets broken [8–10]. Dirac semimetals exhibit unique and exciting features such as ultra-high mobility [11], large magnetoresistance [11,12], chiral magnetic effect [13,14], etc. These exotic phenomena have been experimentally reported in a number of topological Dirac semimetals, namely Na_3Bi [15,16], Cd_2As_3 [11,17,18], $ZrTe_5$ [19,20], $Bi_{1-x}Sb_x$ [21], $YbMnBi_2$ [22], TIBiSSe [12].

Recently, grey tin, or α-Sn, a zero-gap semiconductor emerges as an exciting material due to its nontrivial band topology [23–25]. It is the elemental candidate showing many topological phases, that can be tailored by various conditions, such as changing the thickness, imposing the strain, and applying the electric and magnetic fields [26,27]. The application of the in-plane tensile strain transforms α-Sn into a robust three-dimensional topological insulator with a large topological gap [24] and a high Fermi velocity [28] , whereas in-plane compressive strain makes it a topological Dirac semimetal protected by four-fold rotational symmetry [26,27]. The in-plane compressive strain, which modifies the electronic structure of α-Sn, can be obtained experimentally by epitaxially growing a thin film on a substrate with lattice constants that do not exactly match those of grey tin. To obtain the Dirac semimetal phase, the desired mismatch is achieved by selecting the appropriate substrates, such as InSb(111) [29], InSb(001) [30], CdTe(111) [31], GaAs(001) [32]. The degeneracy of the Dirac cones is lifted in the presence of an external magnetic field, turning α-Sn into a Weyl semimetal. The presence of a pair of Weyl points in momentum space can lead to appearance of a peculiar phenomenon when the electric and magnetic fields are applied parallel to each other. It is known as a chiral anomaly and, can be observed as a positive magneto-conductivity in real crystalline materials suggested by Nielsen-Ninomiya in 1983 [33]. Its origin is the charge pumping between Weyl points (WPs) of opposite chirality that occurs in a Weyl semimetal (WSM) subjected to the electric and magnetic fields applied in parallel along the direction of the WPs separation [13]. Such negative magnetoresistance has been reported by various groups in topological Dirac and Weyl semimetals [14,15,20,34,35], but there exist other mechanisms that could underlie this effect without involving charge pumping between the Weyl nodes [36–38]. In this regard, measurements of the thermoelectric effects offer an opportunity to complement to electrical measurements and gain valuable insight into electronic transport properties [39–42].

In this work, we investigate the electrical and thermoelectrical properties of the α-Sn thin film, which is a topological Dirac semimetal when deposited on a CdTe/GaAs (001) substrate. To ensure the best-quality, the sample was grown using molecular beam epitaxy (MBE). We report on the quadratic variation in the field dependencies of the electrical conductivity and thermopower, which can be explained as a consequence of the chiral anomaly. We also calculated the ratio of intervalley scattering time to mean free time, which indicates the role of chiral Weyl fermions in the emergence of the negative longitudinal magnetoresistance and the negative slope of thermopower at the high magnetic field.

2. Materials and methods

Epitaxial film of 200 nm thickness α-Sn was grown by the molecular beam epitaxy (MBE) on (001) GaAs substrate with a 4 μm CdTe buffer layer. CdTe buffer provides the necessary ~0.1 % compressive in-plane strain to induce the Dirac semimetal phase in grey tin. Extensive structural characterization confirmed the high quality of the obtained film without any inclusions of the metallic β-Sn phase, as well as the value of the strains. More details about the growth procedure, as well as the structural characterization of the studied film can be found in Reference [32].

To perform the electric transport measurements, we cut the sample with a length (*a*-axis) of 2.2 mm and a width (*b*-axis) of 0.6 mm. This reasonable aspect ratio of the sample was chosen to minimize the geometric effects on our experimental data. We measured the resistivity using the standard four probe method. The electrical contacts were made with 25 μm thick gold wires and DuPont 4929 silver paint. The current contacts were made along the entire width of a sample to minimize the possibility of the current jetting effect occurrence [43]. The dc electrical current was applied using a Keithley 6221 current source and voltages along the sample were measured with a Keithley 2182A nanovoltmeter.

To measure the thermoelectric properties, the sample was mounted between the two phosphor bronze clamps with two Cernox thermometers attached. These were used to determine the thermal gradient along the sample generated by a Micro-Measurements strain gage heater (10 kΩ resistance), which was connected to Keithley 6221 current source. Thermoelectric voltage data were collected by an EM Electronics A20a DC sub-nanovolt amplifier working in conjunction with a Keithley 2182A nanovoltmeter. The temperature dependence of thermoelectric power was measured with the heater off and on method, while for the magnetic field (± 14.5 T) sweeps the heater was continuously turned on.

The electronic structure calculations were carried out with the projector augmented wave approach within the density functional theory framework, utilizing the VASP package [44]. A plane-wave energy cut-off of 650 eV was employed in the study. We have performed the calculation using a meta-GGA approach, which is based on the modified Becke-Johnson (MBJ) exchange potential together with local density approximation for the correlation potential scheme with the parameter CMBJ = 1.215 in order to get the experimental band ordering [45]. The calculations of electronic structures were performed with a 12 ×12 ×10 Monkhorst-Pack k-mesh [46], incorporating the spin-orbit coupling self-consistently. The VASPWANNIER90 interface was employed in our study and we utilized s and p orbitals of Sn atoms to generate ab initio tight-binding Hamiltonian without performing the procedure for maximizing localization [47,48]. The calculation of the surface state was performed using the semi-infinite Green's function approach incorporated in the Wanniertools [49,50].

3. Results and Discussions

The thermoelectric power (S) and electrical resistivity (ρ) were measured respectively with the thermal gradient (∇T) or electrical current (j) applied along a-axis of the α-Sn thin film. Figure 1 presents the temperature dependence of resistivity in zero magnetic field (B) measured in the temperature range 2 - 300 K. The entire $\rho(T)$ dependence can be divided into two temperature regions, namely, for $T \gtrsim 135$ K we observe a semiconducting behaviour that can be attributed to the increasing with temperature contribution to electrical transport from thermally excited holes [51]. Those holes originate from the thermally driven transitions between valence and conduction parts of the Γ_{8vc}^{+} band as well as from the indirect transition $L_{6c}^{+} - \Gamma_{8vc}^{+}$ found in the calculated electronic structure of α-Sn [52]. In the latter, the magnitude of the band gap in the epitaxially stretched α-Sn thin film is temperature dependent and becomes larger as the temperature decreases [53]. In consequence, thermal hole excitation is prevented for $T \lesssim 135$ K and $\rho(T)$ behaves in a metallic-like manner. This is due to the electrons in the vicinity of Γ- bands dominating the transport features of α-Sn at low temperatures [51]. Interestingly, even at a very low temperature, some contribution to the electronic transport from hole-like charge carriers is still present [32].

It appears that the temperature dependence of the thermopower is also affected by the presence of two types of charge carriers. In almost the entire temperature range the thermopower is negative reflecting a dominating role of highly mobile electrons. The absolute value of S reaches its maximum of 22.5 μV/K at $T \approx 150$ K. The upturn in $S(T)$ above this temperature likely reflects the discussed above increasing contribution from the thermally excited holes. For a multiband conductor, the total thermoelectric power is a sum of individual band contributions weighted by the respective conductivities. Within the two-band model this can be expressed as $S = (S_e \sigma_e + S_h \sigma_h)/\sigma$, where $\sigma = \sigma_e + \sigma_h$, where subscripts e and h denote contributions from electrons and holes, respectively. Therefore, at high temperatures the increasing positive participation from thermally excited holes will result in a decreasing absolute value of negative S dominated by electrons. Below $T \approx 50$ K the Seebeck coefficient gets smaller than 1 μV/K and attains a positive value in the low temperature limit (see inset of the Fig. 1.), which can be also seen in the $S(B)$ dependences presented in Fig. 2b. This may be due to phonon-drag, but also due to contribution from the low-mobility holes, which were recently reported to be present at low temperatures in α-Sn thin films [32]. For the former $S(T)$ should exhibit a maximum at the temperature of about $\Theta_D/5$ [54], where Θ_D is the Debye temperature. In grey tin $\Theta_D \approx 260$ K [55], but the maximum we observe is at the temperature somewhat lower than the expected $T \approx 50$ K. However, this is only an estimated position, which may be also effectively shifted by contribution from diffusive thermopower. Nevertheless, this positive contribution appears to be weakly dependent on the magnetic field, so does not affect our analysis.

The magnetoresistance of α-Sn was measured at different temperatures in the parallel configuration of the electrical current and magnetic field ($j \parallel B$), the results are presented in Fig. 2a. Below $T \approx 100$ K, a Landau quantization occurs, leading to the appearance of pronounced Shubnikov de Haas (SdH) effect in high magnetic field. The resulting strong oscillations in $\rho(B)$ are shown in Fig. S1(a) in Supplemental Material (SM) after subtraction of slowly varying background (3rd order polynomial). The fast Fourier transform (FFT) spectrum (see Fig. S1(b)) reveals a single slow frequency $F \sim 12$ T, that can be assigned to a bulk Dirac point near the fermi level of α-Sn, in agreement with the previous study [1]. The SdH oscillations can be described by the Lifshitz - Kosevich theory [56]:

$$\Delta\rho \propto R_T R_D R_S \cos\left[2\pi\left(\frac{F}{B} - \frac{1}{2} + \beta \pm \delta\right)\right], \tag{1}$$

The three damping factors are: the thermal reduction factor $R_T = \frac{\chi}{\sinh(\chi)}$, the Dingle damping factor $R_D = exp\left(-\chi\frac{T_D}{T}\right)$ (T_D is the Dingle temperature) and the spin splitting term $R_S = \cos\left(\frac{p\pi}{2}\frac{gm^*}{m_e}\right)$. The parameter $\chi = \frac{2\pi^2 k_B T m^*/m_e}{e\hbar B}$, where $k_B = 1.381 \times 10^{-23}$ JK^{-1} is the Boltzman constant, $e = 1.602 \times 10^{-19}$ C, $m_e = 9.108 \times 10^{-31}$ kg are the electron charge and mass, $\hbar = 1.054 \times 10^{-34}$ Js is reduced Planck's constant, and m^* is the cyclotron mass of the charge carrier. Within the R_S term, g is the Landé factor, p is the harmonic order. Under cosine function in Eqn. 1, F is the frequency of quantum oscillations (QO), $2\pi\beta$ is the

Berry phase, $\delta = \pm\frac{1}{8}$ is the phase shift related to the dimensionality of the electronic structure of a 3D system.

The effective mass can be calculated from the temperature dependence of the amplitude of the oscillations described by the thermal reduction factor R_T (see Fig. S1(c) in the SM) and the resulting small effective mass $m^* \approx 0.01\ m_e$ is close to that previously reported [32]. The frequency of the quantum oscillations is directly related to the Fermi surface cross section area via the Onsager relation: $F = \left(\frac{\hbar}{2\pi e}\right) A_F$, where A_F is the Fermi surface cross section area. Since the Fermi momentum $k_F = \sqrt{\frac{A_F}{\pi}}$, we have deduced the Fermi velocity $v_F = \frac{\hbar k_F}{m^*}$ and the Fermi energy $E_F = m^* v_F^2$ under the assumption that charge carriers have linear energy dispersion [57]. The estimated v_F and E_F are about 2.2×10^6 m/s and 277 meV respectively. Fig. S1(d) in SM shows that the experimental data can be well modelled with Eqn. 1 from which another parameter that can be obtained from the analysis of QO is the Dingle temperature, which was estimated to be T_D = 11 K at 9.9 K temperature, again in good agreement with results reported in Ref. [32]. From the Dingle temperature, we can calculate the quantum life time $\tau_q = \frac{\hbar}{2\pi k_B T_D}$ and quantum mobility $\mu_q = \frac{e\tau_q}{m^*}$ [58], which are $\tau_q \approx 1\times10^{-13}$ s and $\mu_q \approx 5900$ cm^{2}V^{-1}s^{-1}, respectively. Such a high value of μ_q confirms the excellent transport properties of α-Sn.

Next, we will focus on a non-oscillatory component in $\rho(B)$ of α-Sn, which, for $j\ ||\ B$, exhibits a large negative longitudinal magnetoresistance (NLMR) at the high field and low temperature. With increasing temperature, NLMR decreases and vanishes above $T \approx 200$ K. Intriguingly, the presence of NLMR for $j\ ||\ B$ was also reported in early studies of quantum oscillations in the bulk single crystals of α-Sn [59]. Furthermore, the authors observed an additional 1/8 phase shift of the SdH oscillation, which is the expected result for the extra Berry phase of carriers from 3D band with linear dispersion [60]. These experimental facts initially remained uninterpreted, but have recently been linked to the presence of Dirac cones [26]. This is interesting because α-Sn in its pristine form should be, as mentioned above, a semiconductor with conduction and valence bands touching each other at the vertices. Perhaps even a small perturbation, such a presence of an internal strain, or a strain applied unwillingly during the experiment, can slightly shift the electronic bands, creating a non-trivial electron structure in the bulk sample [61].

The appearance of NLMR was reported for a large number of Dirac and Weyl semimetals [15,20,34,35,62] and it has been ascribed to pumping of the chiral charge between the Weyl nodes. On the other hand, questions were also raised as to whether the effect could be due to extrinsic mechanisms [36,38]. In particular, the current jetting contribution in highly mobile Weyl semimetals caused concerns about the detection of the chiral current in electrical measurements [43]. Therefore, the complementary measurements of other phenomena, such as the thermoelectric power, can provide a unique opportunity to investigate the effects of the chiral anomaly without current jetting artefact [41,43].

Figure 2b presents the magnetic field dependences of the thermopower (with $B \parallel \nabla T$) for selected temperatures. As mentioned above, in addition to the negative thermopower attributable to electrons, we also observe a roughly field independent positive contribution to the Seebeck coefficient. This appears in $S(B)$ data in Fig. 2b as a temperature dependent vertical shift that does not affect the field dependent part. At a low magnetic field, S initially increases with B – such a dependence was also observed in other topological Dirac semimetals and it was attributed to the process of Weyl nodes creation [43,63]. Below

$T \approx 50$ K we see a small peak in $S(B)$ at $B \approx 5.2$ T, which can be attributed to the quantum oscillations. For the frequency obtained from the SdH effect ($F = 12$ T), the next peak in $S(B)$ is expected at $B \approx 8.8$ T, which coincides with the maximum that occurs at $B \approx 9$ T. The contribution from QO to the total value of S at the maximum can be calculated using the Lifshitz – Kosevich formula and is presented in Fig. S2 in the SM. At $T \approx 30$ K, the peak value of the QO from the baseline is $\approx 0.026\ \mu\mathrm{VK}^{-2}$, which is ≈ 33 % of the total weight of S at $B \approx 9$ T. However, the calculated contribution from QO significantly decreases with increasing temperature. For example, this becomes approximately 8 % at $T \approx 50$ K and vanishes completely above $T \gtrsim 55$ K, while the peak of $S(B)$ linked to formations of Weyl points is still present in the data. The maximum in $S(B)$ shifts to higher magnetic fields and at $B \approx 12$ T is clearly visible even at $T \approx 150$ K (see Fig. 2b). Thus, it is unlikely that the negative slope of $S(B)$ observed at high magnetic field originates from quantum oscillations and, alternatively, this type of anomalous field dependence was indicated as a manifestation of the chiral anomaly in several Dirac and Weyl semimetals [43].

To support our experimental observation, we have performed first-principles calculations using VASP [44] and Wannier90 [47]. Fig. 3(a) shows electronic band structure in the presence of spin orbit coupling (SOC), where the most of electronic bands are contributed by s and p orbital of Sn atoms. We observe a four-fold degenerate band crossing along $\Gamma \rightarrow Z$ direction with a camel back features [64,65](see Fig. 3(b)). The Dirac points are located 9 meV above the Fermi level $E_{Dirac} = E_f - 0.009$ eV at $(0, 0, \pm k_z)$, where $k_z = 0.398$ Å^{-1}, although it should be mentioned that density functional theory calculations can over- or underestimate the Fermi energy.

The pair of Dirac point can be shown in the electronic band structure in the 2D plane shown in Fig. 3(d). The application of magnetic field gives rise to a negative magnetoresistance demonstrated in the calculations when $\theta = 0^\circ$ as shown in Fig. 3(e), which is consistent with experimental observation. Furthermore, we demonstrate the Dirac semimetal phase by investigating the band structure projected in Fig. S3 of the SM, (a) along the (100) direction and (b) along the (001) direction. The presence of topological surface state is evident with a bulk band crossing points. In addition, we calculate the Fermi surface projected on (100) and (001) surface in the bottom panel of Fig. S3. The Fermi surface along (100) shows the presence of close topological Fermi arc k_y-k_z plane. These are C_{4z} rotational symmetry-protected Dirac nodes that are against gap formation. In the presence of a finite Zeeman field that breaks time-reversal symmetry, each Dirac node separates into two Weyl nodes with the opposite chirality. Notably, these paired Weyl nodes are still aligned with the high symmetry direction protected by the crystal symmetry C_{4z}. The development of the chiral anomaly is facilitated by the combination of this property and the chiral nature of their lowest Landau [27,43].

If the negative slopes of $\rho(B)$ and $S(B)$ in the high field are in fact signs of the chiral anomaly, they should disappear when the magnetic field is tilted away from being parallel to j or ∇T, respectively. The angular dependences of longitudinal transport coefficients at T = 60 K are presented in Fig. 4. In the measurement of the magnetoresistance (Fig. 4a) we observed the maximal NLMR when $\theta_\rho = 0^\circ$ (θ_ρ is the angle between B and j), whereas rotation of the magnetic field from in-plane to out-of-plane (from *a*- toward *c*-axis) quickly causes the dip in $\rho(B)$ to vanish. Similar behaviour has been previously observed in topological semimetals, owing to the presence of a chiral current in the system [15,62,66]. The positive magnetoresistance for $\theta_\rho \gtrsim 2.5^\circ$ is due to the vanishing of the chiral anomaly influence and restoration of the orbital effect induced by the Lorentz force. Remarkably, the chiral anomaly appears to affect the magneto-thermopower (Fig. 4b) in a similar manner. Namely, the negative slope of $S(B)$ that occurs at a high magnetic field when θ_S = 0° (θ_S is the angle between B and ∇T) becomes positive when B is away from ∇T. The threshold for θ_S, which is about 10°, is larger than that of θ_p, possibly because the relative contribution from out-of-plane positive magneto-thermopower is not as large as that from orbital magnetoresistance.

The magnetic field breaks the time reversal symmetry, leading to the formation of Weyl nodes in α-Sn through the degeneracy of the Dirac nodes. In the presence of parallel electric and magnetic fields, the imbalance in the number of Weyl fermions of different chirality leads to the generation of an additional current that contributes to the total electrical conductivity. In the semi-classical regime, this can be expressed as [67,68]:

$$\sigma(B) = \sigma(0) + \sigma(0) * \frac{1}{3}\frac{\tau_i}{\tau}\frac{B^2}{B_q^2}, \quad (2)$$

where $\sigma(0)$ is the Drude conductivity, $B_q = \frac{2E_F^2}{3e\hbar v_F^2}$ is the quantum magnetic field, and $\frac{\tau_i}{\tau}$ is the ratio of intervalley scattering time to the mean free time of charge carriers. The corresponding influence of the chiral anomaly on the thermoelectric power can be calculated using the Mott relation, which should obeyed if the chemical potential is larger than $k_B T$ and the scattering is dominated by elastic processes [41]. If the mean free time is assumed to be independent of energy, the equation reads [67,68]:

$$S(B) = S(0) - S(0) * 2\frac{\tau_i B^2}{3\tau B_q^2}, \quad (3)$$

where $S(0)$ is the background thermopower unrelated to the chiral anomaly. Since the magnetic field can change the distance in k-space between Weyl cones, e.g. [69], the intervalley scattering time can in principle be expected to be field dependent. On the other hand, the model we used to describe the experimental data assumes τ_i to be field independent, which appears to be a sufficient approximation in the high field limit.

Moreover, this is in agreement with optical studies of the Dirac semimetal Cd_3As_2, which concluded that chiral relaxation shows little field dependence [70]. Equations 2 and 3 describe the behaviour of the non-oscillatory part of the respective signal, but this has appeared to be difficult to extract from field dependences of conductivity at low temperatures. This was done by simulating the SdH oscillations using Lifshitz - Kosevich formula (see Fig. S4 in SM) up to B = 8 T and then extrapolating the oscillatory signal to higher fields. Finally, we subtract the oscillations in order to obtain the non-oscillatory part of $\sigma(B)$, However, the results of extrapolation were not perfect below T = 100 K, hence we have chosen to restrict the upper limit of the fit to 10 T. As shown in Fig. 5a, $\sigma(B)$ at this intermediate field follows a quadratic dependence on B expected for the chiral anomaly [41,67,68] and can be approximated with Eqn. 2. Remarkably, the thermopower at a high magnetic field also appears to be well described by the model involving the chiral anomaly. Equation 3 predicts that the negative slope of the magneto-thermopower to be B^2 dependent component, which in fact appears in $S(B)$ dependences – see Fig. 5b. From the fitting of the magnetoresistance and magneto-thermopower with Eqns. 2 and 3, we can estimate the ratio of the intervalley lifetime to the transport lifetime $\frac{\tau_i}{\tau}$, which is the parameter that defines whether an electronic system is in fact in the chiral limit [71]. The essential condition that must be met to observe the pumping of Weyl fermions from one node to another is $\tau_i > \tau$. Figure 6 presents the temperature dependences of $\frac{\tau_i}{\tau}$ calculated from $\sigma(B)$ and $S(B)$, the latter multiplied by a prefactor 3/2, the reason for that will be discussed later. The agreement between these two independent experimental results is good i.e. the ratio $\frac{\tau_i}{\tau}$ decays with temperature, but both $\frac{\tau_i}{\tau}(T)$ do not coincide exactly. Similar behaviour was also reported for the topological Dirac semimetal $ZrTe_5$ [67]. For α-Sn, the relaxation time ratio from thermoelectric data is calculated with Eqn. 3 is smaller than one calculated from the electrical measurements. A likely reason for this discrepancy may be the approximations made to derive Eqn. 3. The first assumption is the energy (E) independent of carrier lifetime [67,68], which is usually not the case for real materials. The term in the Mott relations $\frac{d \ln \tau(E)}{dE}$ has significant contributions to the diffusion thermoelectric power [54]. For example, for metals at high temperature, the relation is expected to be $\tau(E) \propto E^{\frac{3}{2}}$ [72]. We include 3/2 factor in the relaxation time ratio calculated from thermoelectric data but our experimental results suggest even stronger energy dependence. This in fact was suggested to be significantly enhanced in the Dirac material SnTe [73]. Another important assumption in Eqn.3 was the strict validity of the Mott relation [67]. Since, the thermopower is measured under the condition of an imbalanced number, but possibly also energy, of chiral Weyl fermions [74] some deviations from the Mott relation can be expected. An actual reason will be an interesting subject of further investigation.

4. Conclusions

We studied the transport properties of the Dirac semimetal α-Sn in the configuration where the magnetic field is non-orthogonal to the electric field or thermal gradient. At the high field, we observed the negative longitudinal magnetoresistance and magneto-thermopower, which also shows a negative slope. Both features, which vary with field like B^2, can be attributed to the chiral anomaly and disappear in high temperatures. Further, a hint that we see manifestations of the chiral anomaly in α-Sn is a strong angular variation of the thermopower and resistivity. The calculated ratio of the intervalley scattering time to the mean free time satisfies the conditions for the chiral limit. We conclude that both the electrical and thermoelectric data indicate the presence of a Weyl system, which forms the chiral anomaly in the magnetic field.

Acknowledgments

We would like to thank V. Volobuiev for growing the sample and to K. Dybko for the discussion. This work was supported by the Foundation for Polish Science through the IRA Programme co-financed by EU within SG (Grant No. MAB/2017/1). R.I and F.X acknowledges the support by the National Science Foundation under Grant No. OIA-2229498. R.I. and F.X. acknowledge the access to the computing facility Cheaha at University of Alabama at Birmingham

Competing financial interests:

The authors declare no competing financial interests.

Data availability

All of the relevant data that support the findings of this study are available from the corresponding author upon reasonable request.

M. S. Alam ORCID iD : 0000-0001-9320-9150

M. Matusiak ORCID iD: 0000-0003-4480-9373

Figures

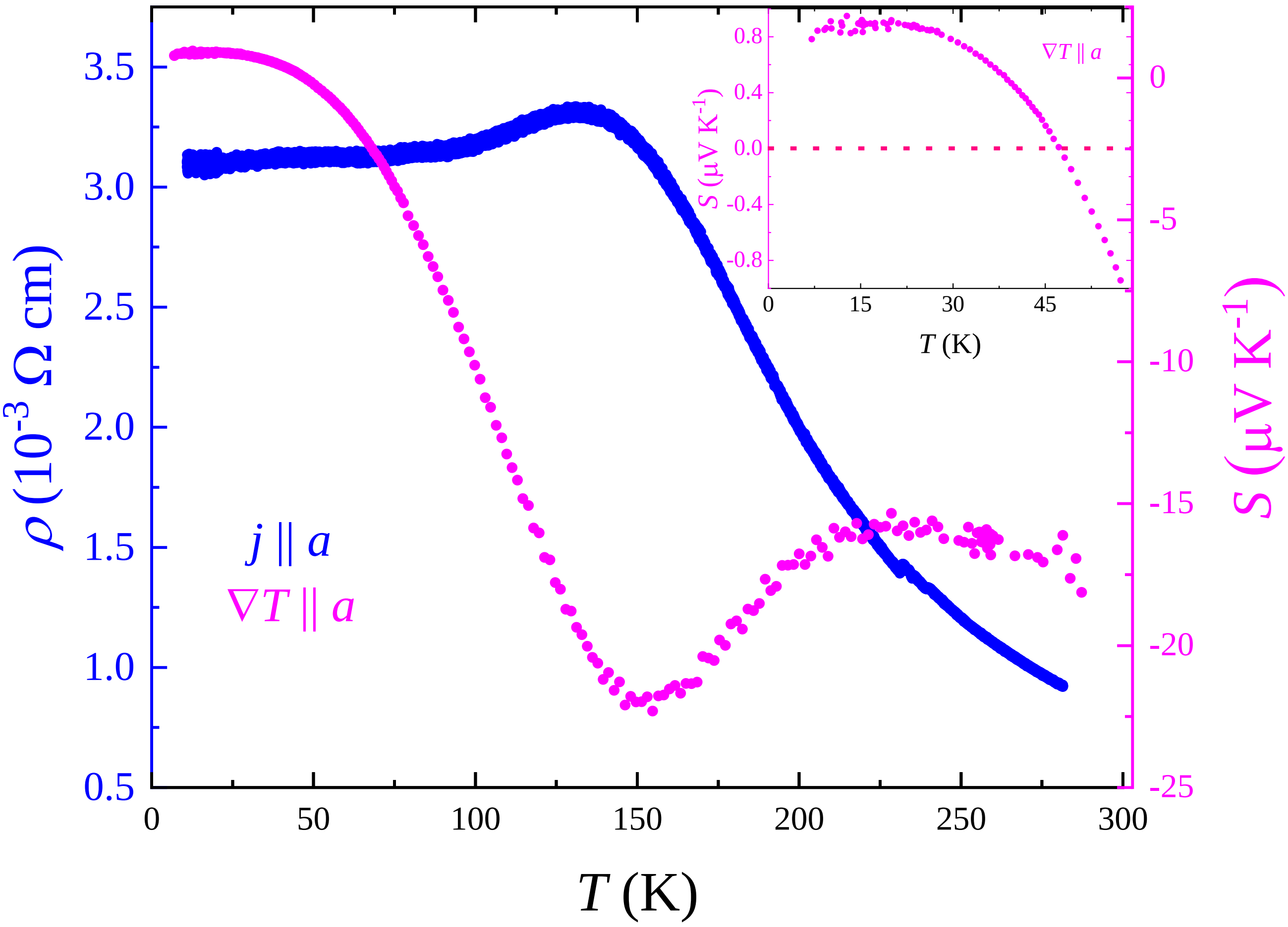

Figure 1. (Color online) Temperature dependences of the resistivity (ρ) and the thermoelectric power (S) of 200 nm thick α-Sn thin film where the current (J) or thermal gradient (∇T) is applied parallel to a – axis. Inset shows low temperature thermoelectric power data.

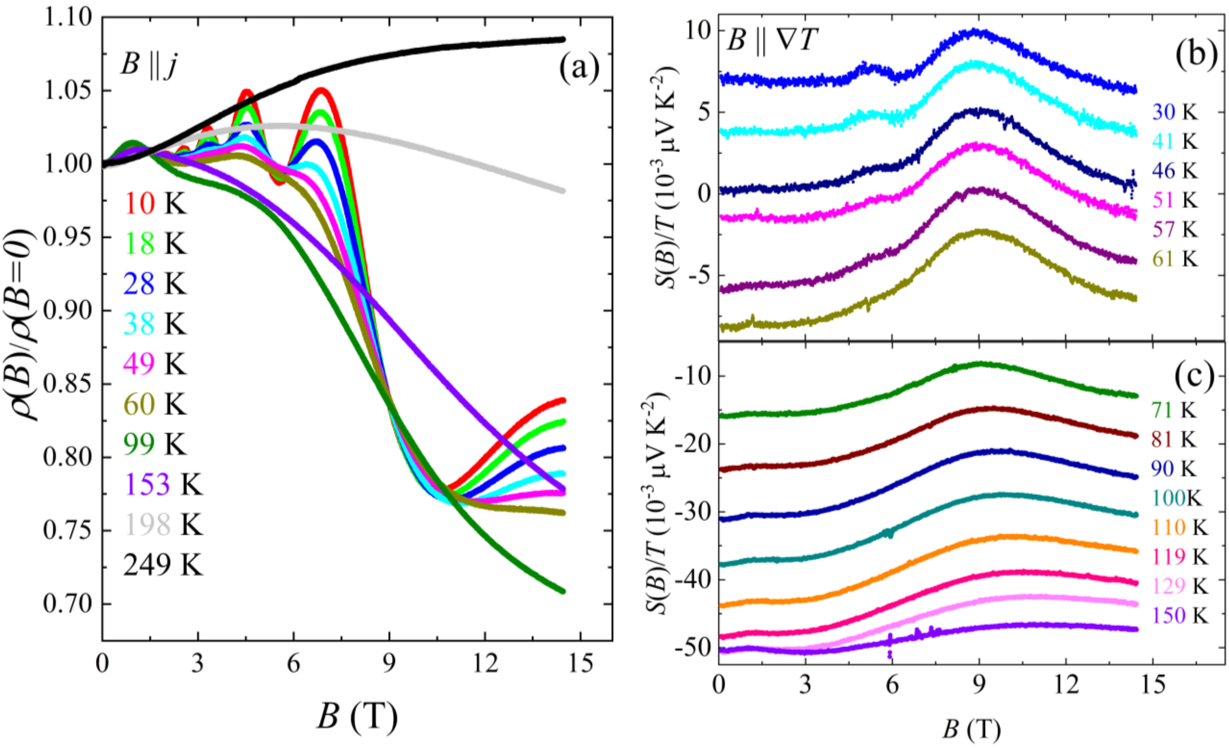

Figure 2. (Color online) Panel a: Normalized magnetoresistance versus magnetic field of α-Sn for selected temperatures when both magnetic field and current are applied parallel to *a*-axis (*B* || *j*). Magnetothermopower of α-Sn measured with the configuration of applied thermal gradient and magnetic field parallel to the *a*- axis (∇*T* || *B),* panel b: at low temperatures; panel c: at high temperatures.

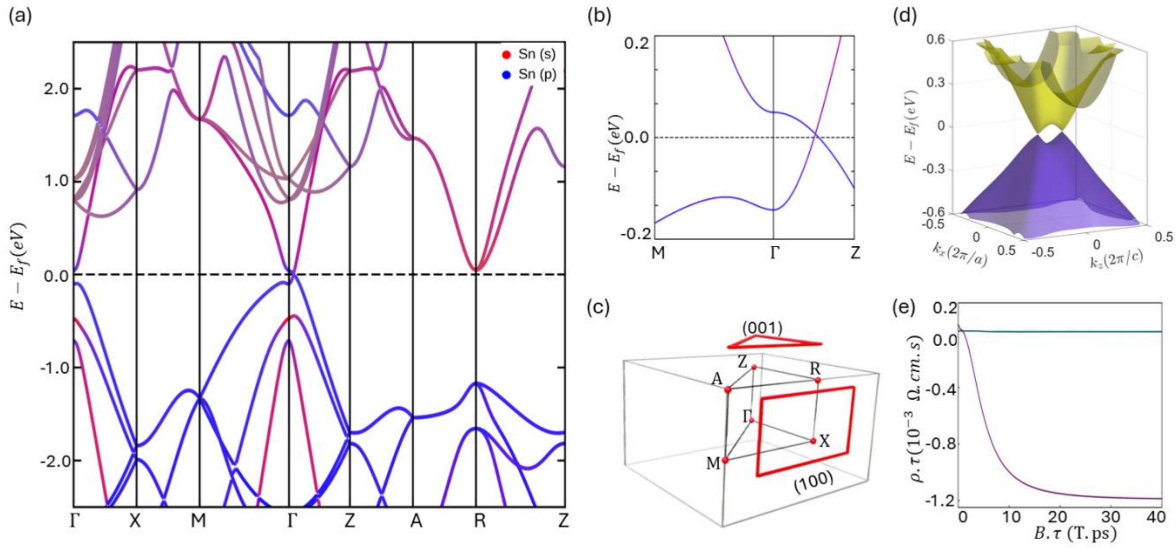

Figure 3. (Color online) a) The electronic band structure of α-Sn in the presence of spin-orbit coupling using density functional theory (DFT) over the full Brillouin zone (BZ); the BZ is shown in (c); the closer look of the along M→Γ→Z is shown in (b) . (d) The 2D band structure in the (k_x-k_z) plane illustrates the position of two Dirac points at (0,0,±k_Z). (e) Magnetoresistance at θ = 0° magnetic field orientations, influenced by Fermi surface topology.

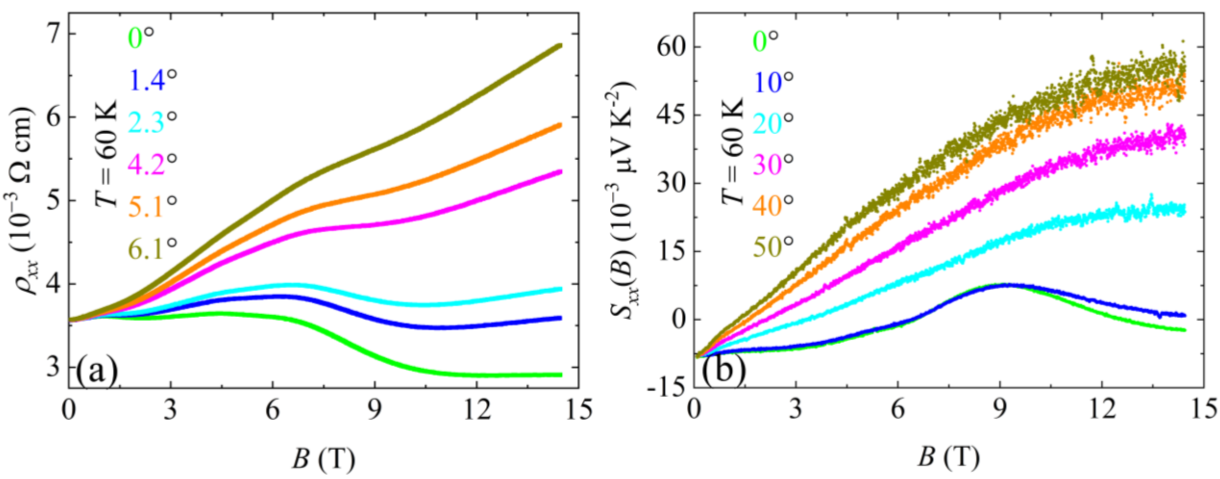

Figure 4. (Color online) Panel a: Resistivity (ρ_{xx}) in function of magnetic field (B) of Dirac semimetal α-Sn for selected angles (Θ, where Θ is the angle between j and B) at a constant temperature 60 K. Panel b: Magnetothermopower ($S_{xx}(B)$) of α-Sn for selected angles (Θ, where Θ is the angle between ∇T and B) at a constant temperature 60 K.

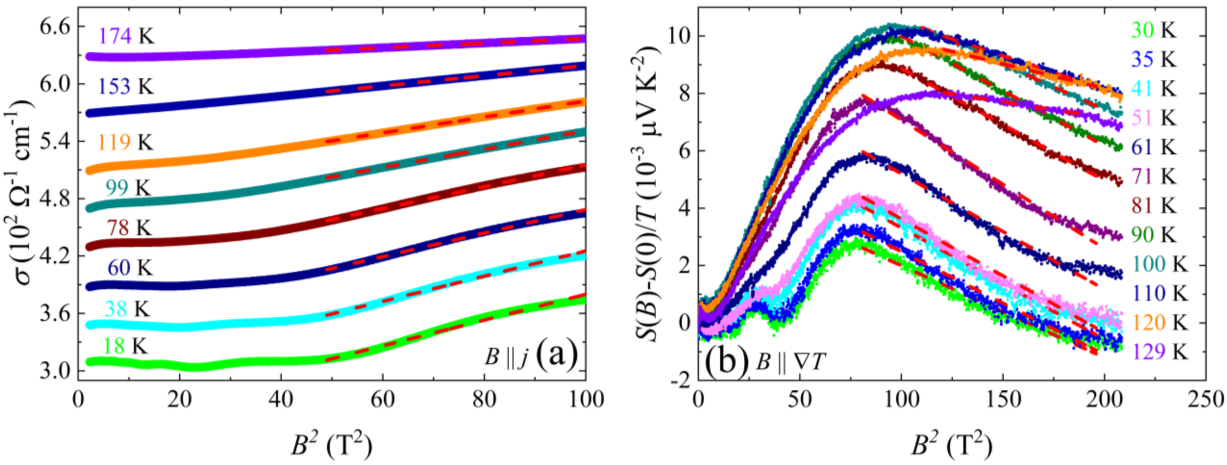

Figure 5 . (Color online) Panel a: Conductivity (σ) in function of square of magnetic field (B) of α-Sn for several temperatures. For the sake of clarity, starting from $\sigma(B^2)$ for T = 38 K, the curves are successively shifted vertically by $10^2\ \Omega^{-1}cm^{-1}$ each for sake of clarity. Panel b: Normalized thermopower $S(B)$ of α-Sn for selected temperatures. The dashed line in both panels shows the fit as calculated from equations 2 and 3.

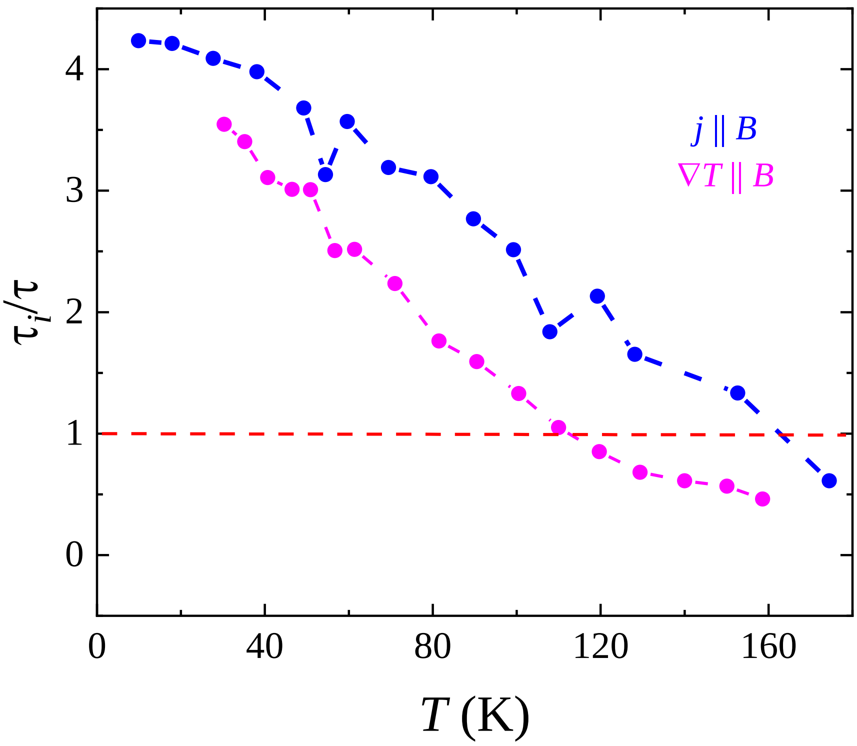

Figure 6 . (Color online) The ratio of intervalley Weyl scattering time to Drude relaxation time (τ_i/τ) of α-Sn sample in function of temperatures with the current (j) or thermal gradient (∇T) along with the magnetic field applied parallel to a – axis.

References

[1] C. L. Kane and E. J. Mele, *Quantum Spin Hall Effect in Graphene*, Phys. Rev. Lett. **95**, 226801 (2005).

[2] M. Z. Hasan and C. L. Kane, *Colloquium: Topological Insulators*, Rev. Mod. Phys. **82**, 3045 (2010).

[3] N. P. Armitage, E. J. Mele, and A. Vishwanath, *Weyl and Dirac Semimetals in Three-Dimensional Solids*, Rev. Mod. Phys. **90**, 015001 (2018).

[4] M. S. Alam, A. Fakhredine, M. Ahmad, P. K. Tanwar, H. Y. Yang, F. Tafti, G. Cuono, R. Islam, B. Singh, A. Lynnyk, C. Autieri, and M. Matusiak, *Sign Change of Anomalous Hall Effect and Anomalous Nernst Effect in the Weyl Semimetal CeAlSi*, Phys. Rev. B **107**, 85102 (2023).

[5] S. M. Young, S. Zaheer, J. C. Y. Teo, C. L. Kane, E. J. Mele, and A. M. Rappe, *Dirac Semimetal in Three Dimensions*, Phys. Rev. Lett. **108**, 140405 (2012).

[6] Z. K. Liu, B. Zhou, Y. Zhang, Z. J. Wang, H. M. Weng, D. Prabhakaran, S. Mo, Z. X. Shen, Z. Fang, X. Dai, Z. Hussain, and Y. L. Chen, *Topological Dirac Semimetal , Na_3Bi*, Science. **343**, 864 (2014).

[7] S. Borisenko, Q. Gibson, D. Evtushinsky, V. Zabolotnyy, B. Büchner, and R. J. Cava, *Experimental Realization of a Three-Dimensional Dirac Semimetal*, Phys. Rev. Lett. **113**, 027603 (2014).

[8] S. Y. Xu, I. Belopolski, N. Alidoust, M. Neupane, G. Bian, C. Zhang, R. Sankar, G. Chang, Z. Yuan, C. C. Lee, S. M. Huang, H. Zheng, J. Ma, D. S. Sanchez, B. K. Wang, A. Bansil, F. Chou, P. P. Shibayev, H. Lin, S. Jia, and M. Z. Hasan, *Discovery of a Weyl Fermion Semimetal and Topological Fermi Arcs*, Science. **349**, 613 (2015).

[9] S. Jia, S. Y. Xu, and M. Z. Hasan, *Weyl Semimetals, Fermi Arcs and Chiral Anomalies*, Nat. Mater. **15**, 1140 (2016).

[10] B. Yan and C. Felser, *Topological Materials: Weyl Semimetals*, Annu. Rev. Condens. Matter Phys. **8**, 337 (2017).

[11] T. Liang, Q. Gibson, M. N. Ali, M. Liu, R. J. Cava, and N. P. Ong, *Ultrahigh Mobility and Giant Magnetoresistance in the Dirac Semimetal Cd_3As_2*, Nat. Mater. **14**, 280 (2015).

[12] M. Novak, S. Sasaki, K. Segawa, and Y. Ando, *Large Linear Magnetoresistance in the Dirac Semimetal TlBiSSe*, Phys. Rev. B. Phys. **91**, 041203(R) (2015).

[13] A. A. Zyuzin and A. A. Burkov, *Topological Response in Weyl Semimetals and the Chiral Anomaly*, Phys. Rev. B. Phys. **86**, 115133 (2012).

[14] D. T. Son and B. Z. Spivak, *Chiral Anomaly and Classical Negative Magnetoresistance of Weyl Metals*, Phys. Rev. B. Phys. **88**, 104412 (2013).

[15] J. Xiong, S. K. Kushwaha, T. Liang, J. W. Krizan, M. Hirschberger, W. Wang, R. J. Cava, and N. P. Ong, *Evidence for the Chiral Anomaly in the Dirac Semimetal Na_3Bi*, Science. **350**, 413 (2015).

[16] S. Liang, J. Lin, S. Kushwaha, J. Xing, N. Ni, R. J. Cava, and N. P. Ong, *Experimental Tests of the Chiral Anomaly Magnetoresistance in the Dirac-Weyl Semimetals Na_3Bi and GdPtBi*, Phys. Rev. X **8**, 031002 (2018).

[17] L. P. He, X. C. Hong, J. K. Dong, J. Pan, Z. Zhang, J. Zhang, and S. Y. Li, *Quantum Transport Evidence for the Three-Dimensional Dirac Semimetal Phase in Cd_3As_2*, Phys. Rev. Lett. **113**, 246402 (2014).

[18] M. Neupane, S. Y. Xu, R. Sankar, N. Alidoust, G. Bian, C. Liu, I. Belopolski, T. R. Chang, H. T. Jeng, H. Lin, A. Bansil, F. Chou, and M. Z. Hasan, *Observation of a Three-Dimensional Topological Dirac Semimetal Phase in High-Mobility Cd_3As_2*, Nat. Commun. **5**, 3786 (2014).

[19] G. Zheng, J. Lu, X. Zhu, W. Ning, Y. Han, H. Zhang, J. Zhang, C. Xi, J. Yang, H. Du, K. Yang, Y. Zhang, and M. Tian, *Transport Evidence for the Three-Dimensional Dirac Semimetal Phase in $ZrTe_5$*, Phys. Rev. B **93**, 115414 (2016).

[20] Q. Li, D. E. Kharzeev, C. Zhang, Y. Huang, I. Pletikosić, A. V. Fedorov, R. D. Zhong, J. A. Schneeloch, G. D. Gu, and T. Valla, *Chiral Magnetic Effect in $ZrTe_5$*, Nat. Phys. **12**, 550 (2016).

[21] H. J. Kim, K. S. Kim, J. F. Wang, M. Sasaki, N. Satoh, A. Ohnishi, M. Kitaura, M. Yang, and L. Li, *Dirac versus Weyl Fermions in Topological Insulators: Adler-Bell-Jackiw Anomaly in Transport Phenomena*, Phys. Rev. Lett. **111**, 246603 (2013).

[22] J. Y. Liu, J. Hu, Q. Zhang, D. Graf, H. B. Cao, S. M. A. Radmanesh, D. J. Adams, Y. L. Zhu, G. F. Cheng, X. Liu, W. A. Phelan, J. Wei, M. Jaime, F. Balakirev, D. A. Tennant, J. F. DItusa, I. Chiorescu, L. Spinu, and Z. Q. Mao, *A Magnetic Topological Semimetal $Sr_{1-y}Mn_{1-z}Sb_2$ ($y, z < 0.1$)*, Nat. Mater. **16**, 905 (2017).

[23] J. C. Rojas-Sánchez, S. Oyarzún, Y. Fu, A. Marty, C. Vergnaud, S. Gambarelli, L. Vila, M. Jamet, Y. Ohtsubo, A. Taleb-Ibrahimi, P. Le Fèvre, F. Bertran, N. Reyren, J. M. George, and A. Fert, *Spin to Charge Conversion at Room Temperature by Spin Pumping into a New Type of Topological Insulator: α -Sn Films*, Phys. Rev. Lett. **116**, 096602 (2016).

[24] Y. Ohtsubo, P. Le Fèvre, F. Bertran, and A. Taleb-Ibrahimi, *Dirac Cone with Helical Spin Polarization in Ultrathin α-Sn(001) Films*, Phys. Rev. Lett. **111**, 216401 (2013).

[25] M. T. Le Duc Anh, Kengo Takase, Takahiro Chiba, Yohei Kota, Kosuke Takiguchi, *Elemental Topological Dirac Semimetal α-Sn with High Quantum Mobility*, Adv. Mater **33**, 2104645 (2021).

[26] H. Huang and F. Liu, *Tensile Strained Gray Tin: Dirac Semimetal for Observing Negative Magnetoresistance with Shubnikov-de Haas Oscillations*, Phys. Rev. B **95**, 201101(R) (2017).

[27] D. Zhang, H. Wang, J. Ruan, G. Yao, and H. Zhang, *Engineering Topological Phases in the Luttinger Semimetal α -Sn*, Phys. Rev. B **97**, 195139 (2018).

[28] R. A. Carrasco, C. M. Zamarripa, S. Zollner, J. Menéndez, S. A. Chastang, J. Duan, G. J. Grzybowski, B. B. Claflin, and A. M. Kiefer, *The Direct Bandgap of Gray α -Tin Investigated by Infrared Ellipsometry*, Appl. Phys. Lett. **113**, 232104 (2018).

[29] V. A. Rogalev, F. Reis, F. Adler, M. Bauernfeind, J. Erhardt, A. Kowalewski, M. R. Scholz, L. Dudy, L. B. Duffy, T. Hesjedal, M. Hoesch, G. Bihlmayer, J. Schäfer, and R. Claessen, *Tailoring the Topological Surface State in Ultrathin α -Sn(111) Films*, Phys. Rev. B **100**, 245144 (2019).

[30] A. Barfuss, L. Dudy, M. R. Scholz, H. Roth, P. Höpfner, C. Blumenstein, G. Landolt, J. H. Dil, N. C. Plumb, M. Radovic, A. Bostwick, E. Rotenberg, A. Fleszar, G. Bihlmayer, D. Wortmann, G. Li, W. Hanke, R. Claessen, and J. Schäfer, *Elemental Topological Insulator with Tunable Fermi Level: Strained α-Sn on Insb(001)*, Phys. Rev. Lett. **111**, 157205 (2013).

[31] S. Küfner, L. Matthes, and F. Bechstedt, *Quantum Spin Hall Effect in α- Sn/CdTe(001) Quantum-Well Structures*, Phys. Rev. B **93**, 045304 (2016).

[32] J. Polaczyński, G. Krizman, A. Kazakov, B. Turowski, J. B. Ortiz, R. Rudniewski, T. Wojciechowski, P. Dłużewski, M. Aleszkiewicz, W. Zaleszczyk, B. Kurowska, Z. Muhammad, M. Rosmus, N. Olszowska, L.-A. De Vaulchier, Y. Guldner, T. Wojtowicz, and V. V. Volobuev, *3D Topological Semimetal Phases of Strained α -Sn on Insulating Substrate*, ArXiv:2309.03951 (2023).

[33] H. B. Nielsen and M. Ninomiya, *The Adler-Bell-Jackiw Anomaly and Weyl Fermions in a Crystal*, Phys. Lett. B **130**, 389 (1983).

[34] C. Z. Li, L. X. Wang, H. Liu, J. Wang, Z. M. Liao, and D. P. Yu, *Giant Negative Magnetoresistance Induced by the Chiral Anomaly in Individual Cd_3As_2 Nanowires*, Nat. Commun. **6**, 1 (2015).

[35] P. K. Tanwar, M. Ahmad, M. S. Alam, X. Yao, F. Tafti, and M. Matusiak, *Gravitational Anomaly in the Ferrimagnetic Topological Weyl Semimetal NdAlSi*, Phys. Rev. B **108**, L161106 (2023).

[36] K. Yoshida, *A Geometrical Transport Model for Inhomogeneous Current Distribution in Semimetals under High Magnetic Fields*, J. Phys. Soc. Jpn **40**, 1027 (1976).

[37] K. Yoshida, *Anomalous Electric Fields in Semimetals under High Magnetic Fields*, J. Phys. Soc. Jpn **39**, 1443 (1975).

[38] F. Arnold, C. Shekhar, S. C. Wu, Y. Sun, R. D. Dos Reis, N. Kumar, M. Naumann, M. O. Ajeesh, M. Schmidt, A. G. Grushin, J. H. Bardarson, M. Baenitz, D. Sokolov, H. Borrmann, M. Nicklas, C. Felser, E. Hassinger, and B. Yan, *Negative Magnetoresistance without Well-Defined Chirality in the Weyl Semimetal TaP*, Nat. Commun. **7**, 11615 (2016).

[39] P. Wei, W. Bao, Y. Pu, C. N. Lau, and J. Shi, *Anomalous Thermoelectric Transport of Dirac Particles in Graphene*, Phys. Rev. Lett. **102**, 166808 (2009).

[40] Y. M. Zuev, W. Chang, and P. Kim, *Thermoelectric and Magnetothermoelectric Transport Measurements of Graphene*, Phys. Rev. Lett. **102**, 096807 (2009).

[41] B. Z. Spivak and A. V. Andreev, *Magnetotransport Phenomena Related to the Chiral Anomaly in Weyl Semimetals*, Phys. Rev. B **93**, 085107 (2016).

[42] M. S. Alam, P. K. Tanwar, K. Dybko, A. S. Wadge, P. Iwanowski, A. Wiśniewski, and M. Matusiak, *Temperature-Driven Spin-Zero Effect in $TaAs_2$*, J. Phys. Chem. Solids **170**, 110939 (2022).

[43] N. P. Ong and S. Liang, *Experimental Signatures of the Chiral Anomaly in Dirac–Weyl Semimetals*, Nat. Rev. Phys. **3**, 394 (2021).

[44] G. Kresse and J. Furthmüller, *Efficient Iterative Schemes for Ab Initio Total-Energy Calculations Using a Plane-Wave Basis Set*, Phys. Rev. B **54**, 11169 (1996).

[45] F. Tran and P. Blaha, *Accurate Band Gaps of Semiconductors and Insulators with a Semilocal Exchange-Correlation Potential*, Phys. Rev. Lett. **102**, 226401 (2009).

[46] J. D. Pack and H. J. Monkhorst, *"special Points for Brillouin-Zone Integrations"*, Phys. Rev. B **13**, 5188 (1976).

[47] A. A. Mostofi, J. R. Yates, Y. S. Lee, I. Souza, D. Vanderbilt, and N. Marzari, *Wannier90: A Tool for Obtaining Maximally-Localised Wannier Functions*, Comput. Phys. Commun. **178**, 685

(2008).

[48] N. Marzari and D. Vanderbilt, *Maximally Localized Generalized Wannier Functions for Composite Energy Bands*, Phys. Rev. B Phys. **56**, 12847 (1997).

[49] Q. S. Wu, S. N. Zhang, H. F. Song, M. Troyer, and A. A. Soluyanov, *WannierTools: An Open-Source Software Package for Novel Topological Materials*, Comput. Phys. Commun. **224**, 405 (2018).

[50] M. P. Lopez Sancho, J. M. Lopez Sancho, and J. Rubio, *Highly Convergent Schemes for the Calculation of Bulk and Surface Green Functions*, J. Phys. F Met. Phys. **15**, 851 (1985).

[51] G. de C. Owen Vail, Patrick Taylor, Patrick Folkes, Barbara Nichols, Brian Haidet,Kunal Mukherjee, *Growth and Magnetotransport in Thin-Film α-Sn on CdTe*, Phys. Status Solidi B **257**, 1800513 (2020).

[52] T. Brudevoll, D. S. Citrin, M. Cardona, and N. E. Christensen, *Electronic Structure of -Sn and Its Dependence on Hydrostatic Strain*, Phys. Rev. B **48**, 8629 (1993).

[53] C. A. Hoffman, J. R. Meyer, R. J. Wagner, F. J. Bartoli, M. A. Engelhardt, and H. Höchst, *Three-Band Transport and Cyclotron Resonance in -Sn and -$Sn_{1-X}Ge_x$ Grown by Molecular-Beam Epitaxy*, Phys. Rev. B **40**, 11693 (1989).

[54] D.K.C. MacDonald, Thermoelectricity: An Introduction to the Principles (Wiley, New York, 1962).

[55] N. Dementev, *Thermodynamical Insight on the Role of Additives in Shifting the Equilibrium between White and Grey Tin*, ArXiv:1011.2275 (2010).

[56] D. Shoenberg, *Magnetic Oscillations in Metals*, Magn. Oscil. Met. Cambridge Univ. Press (1984).

[57] Z. Ren, A. A. Taskin, S. Sasaki, K. Segawa, and Y. Ando, *Large Bulk Resistivity and Surface Quantum Oscillations in the Topological Insulator Bi_2T_2Se*, Phys. Rev. B **82**, 241306 (2010).

[58] A. Narayanan, M. D. Watson, S. F. Blake, N. Bruyant, L. Drigo, Y. L. Chen, D. Prabhakaran, B. Yan, C. Felser, T. Kong, P. C. Canfield, and A. I. Coldea, *Linear Magnetoresistance Caused by Mobility Fluctuations in n -Doped Cd_3As_2*, Phys. Rev. Lett. **114**, 117201 (2015).

[59] E. D. Hinkley and A. W. Ewald, *Oscillatory Magnetoresistance in Gray Tin*, Phys. Rev. **134**, A1261 (1964).

[60] C. M. Wang, H. Z. Lu, and S. Q. Shen, *Anomalous Phase Shift of Quantum Oscillations in 3D Topological Semimetals*, Phys. Rev. Lett. **117**, 077201 (2016).

[61] C. Z. Xu, Y. H. Chan, Y. Chen, P. Chen, X. Wang, C. Dejoie, M. H. Wong, J. A. Hlevyack, H. Ryu, H. Y. Kee, N. Tamura, M. Y. Chou, Z. Hussain, S. K. Mo, and T. C. Chiang, *Elemental Topological Dirac Semimetal: α -Sn on InSb(111)*, Phys. Rev. Lett. **118**, 146402 (2017).

[62] X. Huang, L. Zhao, Y. Long, P. Wang, D. Chen, Z. Yang, H. Liang, M. Xue, H. Weng, Z. Fang, X. Dai, and G. Chen, *Observation of the Chiral-Anomaly-Induced Negative Magnetoresistance: In 3D Weyl Semimetal TaAs*, Phys. Rev. X **5**, 031023 (2015).

[63] M. Hirschberger, S. Kushwaha, Z. Wang, Q. Gibson, S. Liang, C. A. Belvin, B. A. Bernevig, R. J. Cava, and N. P. Ong, *The Chiral Anomaly and Thermopower of Weyl Fermions in the Half-Heusler GdPtBi*, Nat. Mater. **15**, 1161 (2016).

[64] R. Islam, B. Ghosh, G. Cuono, A. Lau, W. Brzezicki, A. Bansil, A. Agarwal, B. Singh, T. Dietl, and C. Autieri, *Topological States in Superlattices of HgTe Class of Materials for Engineering Three-Dimensional Flat Bands*, Phys. Rev. Res. **4**, 023114 (2022).

[65] Z. Wang, H. Weng, Q. Wu, X. Dai, and Z. Fang, *Three-Dimensional Dirac Semimetal and Quantum Transport in Cd_3As_2*, Phys. Rev. B **88**, 125427 (2013).

[66] C. Zhang, E. Zhang, W. Wang, Y. Liu, Z. G. Chen, S. Lu, S. Liang, J. Cao, X. Yuan, L. Tang, Q. Li, C. Zhou, T. Gu, Y. Wu, J. Zou, and F. Xiu, *Room-Temperature Chiral Charge Pumping in Dirac Semimetals*, Nat. Commun. **8**, 13741 (2017).

[67] W. Zhang, P. Wang, G. Gu, X. Wu, and L. Zhang, *Negative Longitudinal Magnetothermopower in the Topological Semimetal $ZrTe_5$*, Phys. Rev. B **102**, 115147 (2020).

[68] Z. Jia, C. Li, X. Li, J. Shi, Z. Liao, D. Yu, and X. Wu, *Thermoelectric Signature of the Chiral Anomaly in Cd_3As_2*, Nat. Commun. **7**, 13013 (2016).

[69] F. Caglieris, C. Wuttke, S. Sykora, V. Süss, C. Shekhar, C. Felser, B. Büchner, and C. Hess, *Anomalous Nernst Effect and Field-Induced Lifshitz Transition in the Weyl Semimetals TaP and TaAs*, Phys. Rev. B **98**, 201107(R) (2018).

[70] B. Cheng, T. Schumann, S. Stemmer, and N. P. Armitage, *Probing Charge Pumping and Relaxation of the Chiral Anomaly in a Dirac Semimetal*, Sci. Adv. **7**, eabg0914 (2021).

[71] C. L. Zhang, S. Y. Xu, I. Belopolski, Z. Yuan, Z. Lin, B. Tong, G. Bian, N. Alidoust, C. C. Lee, S. M. Huang, T. R. Chang, G. Chang, C. H. Hsu, H. T. Jeng, M. Neupane, D. S. Sanchez, H. Zheng, J. Wang, H. Lin, C. Zhang, H. Z. Lu, S. Q. Shen, T. Neupert, M. Z. Hasan, and S. Jia, *Signatures of the Adler-Bell-Jackiw Chiral Anomaly in a Weyl Fermion Semimetal*, Nat. Commun. **7**, 10735 (2016).

[72] A. H. Wilson, *The theory of metals*, I. Proc. R. Soc. Lond. A **138**, 594 (1932).

[73] T. H. Liu, J. Zhou, M. Li, Z. Ding, Q. Song, B. Liao, L. Fu, and G. Chen, *Electron Mean-Free-Path Filtering in Dirac Material for Improved Thermoelectric Performance*, Proc. Natl. Acad. Sci. U. S. A. **115**, 879 (2018).

[74] J. Gooth, A. C. Niemann, T. Meng, A. G. Grushin, K. Landsteiner, B. Gotsmann, F. Menges, M. Schmidt, C. Shekhar, V. Süß, R. Hühne, B. Rellinghaus, C. Felser, B. Yan, and K. Nielsch, *Experimental Signatures of the Mixed Axial-Gravitational Anomaly in the Weyl Semimetal NbP*, Nature **547**, 324 (2017).

Supplemental material:

Quantum transport properties of the topological Dirac Semimetal α-Sn

Md Shahin Alam [1,*] Alexandr Kazakov [1], Mujeeb Ahmad [1] , Rajibul Islam [2], Fei Xue [2], and Marcin Matusiak [1,3,†]

1. *International Research Centre MagTop, Institute of Physics, Polish Academy of Sciences, Aleja Lotników 32/46, PL-02668 Warsaw, Poland*
2. *Department of Physics, University of Alabama at Birmingham, Birmingham, Alabama 35294, USA*
3. *Institute of Low Temperature and Structure Research, Polish Academy of Sciences, ulica Okólna 2, 50-422 Wrocław, Poland*

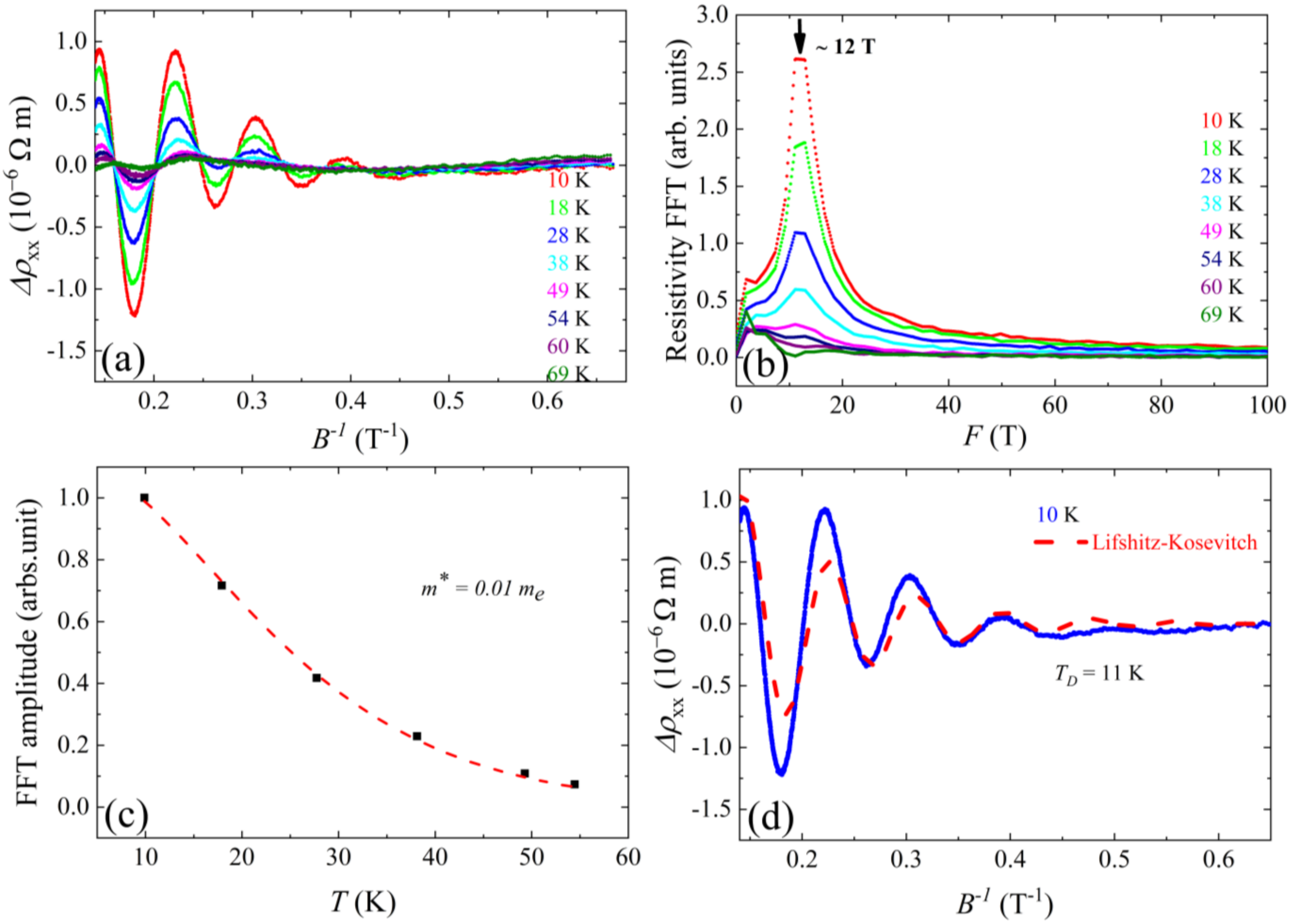

Figure S1 . (Color online) (a) Shubnikov de Hass oscillations after subtracting the smooth 3rd order polynomial background from $\rho_{xx}(B)$ at different temperatures. (b) Fast Fourier transform spectrum of α-Sn showing a single frequency at ~12 T, calculated from SdH oscillations data, the effective field of oscillations taken between 1.5-8 T. (c) Amplitude of the FFT spectrum of the ~ 12 T frequency plotted against temperatures. Red dashes lines represent the fit to the thermal damping factor (R_T) from the Lifshitz-Kosevich formula. (d) Shubnikov de Hass oscillations at 10 *K* temperature. Red dashes line presents the fit to the Lifshitz-Kosevich formula (see equation 1 in the main text).

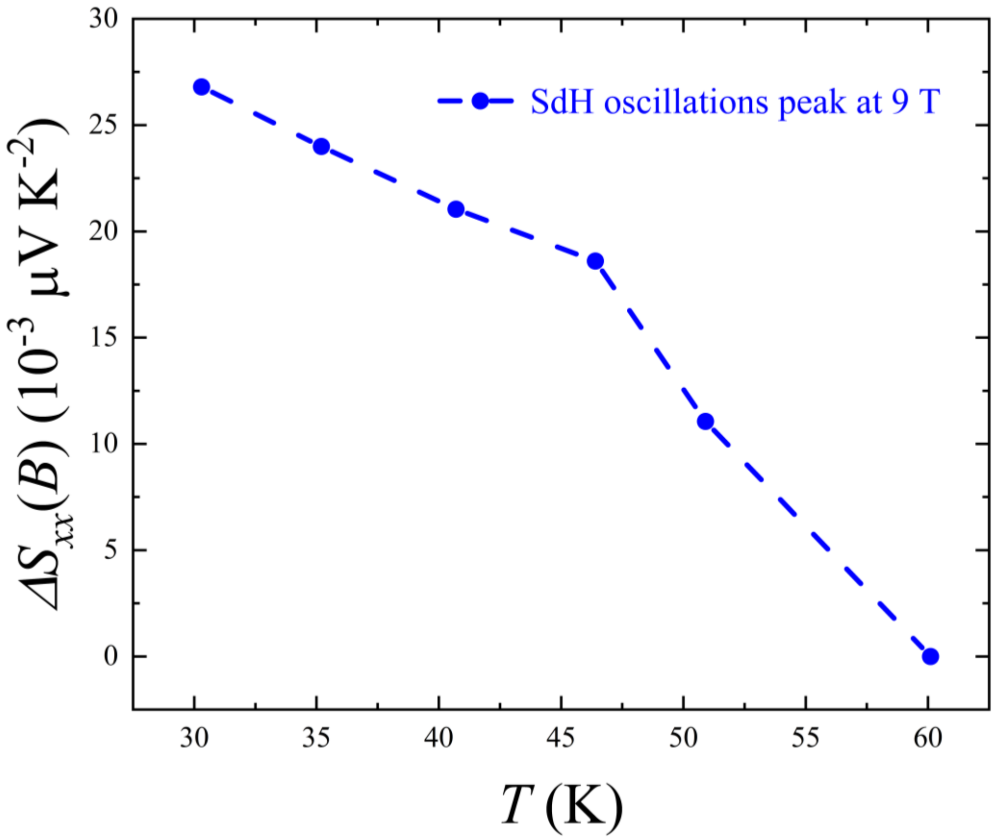

Figure S2 . (Color online) Temperature dependence of the peak height of quantum oscillations of the thermopower ($\Delta S/T$) at 9 T. The peak height at 8.8 T with respect to the peak height at 5.2 T from the baseline was calculated using the Dingle term (R_D) from the Lifshitz-Kosevich formula. The T_D for the higher temperatures was estimated in a similar way as for the 10 K temperature (see main text).

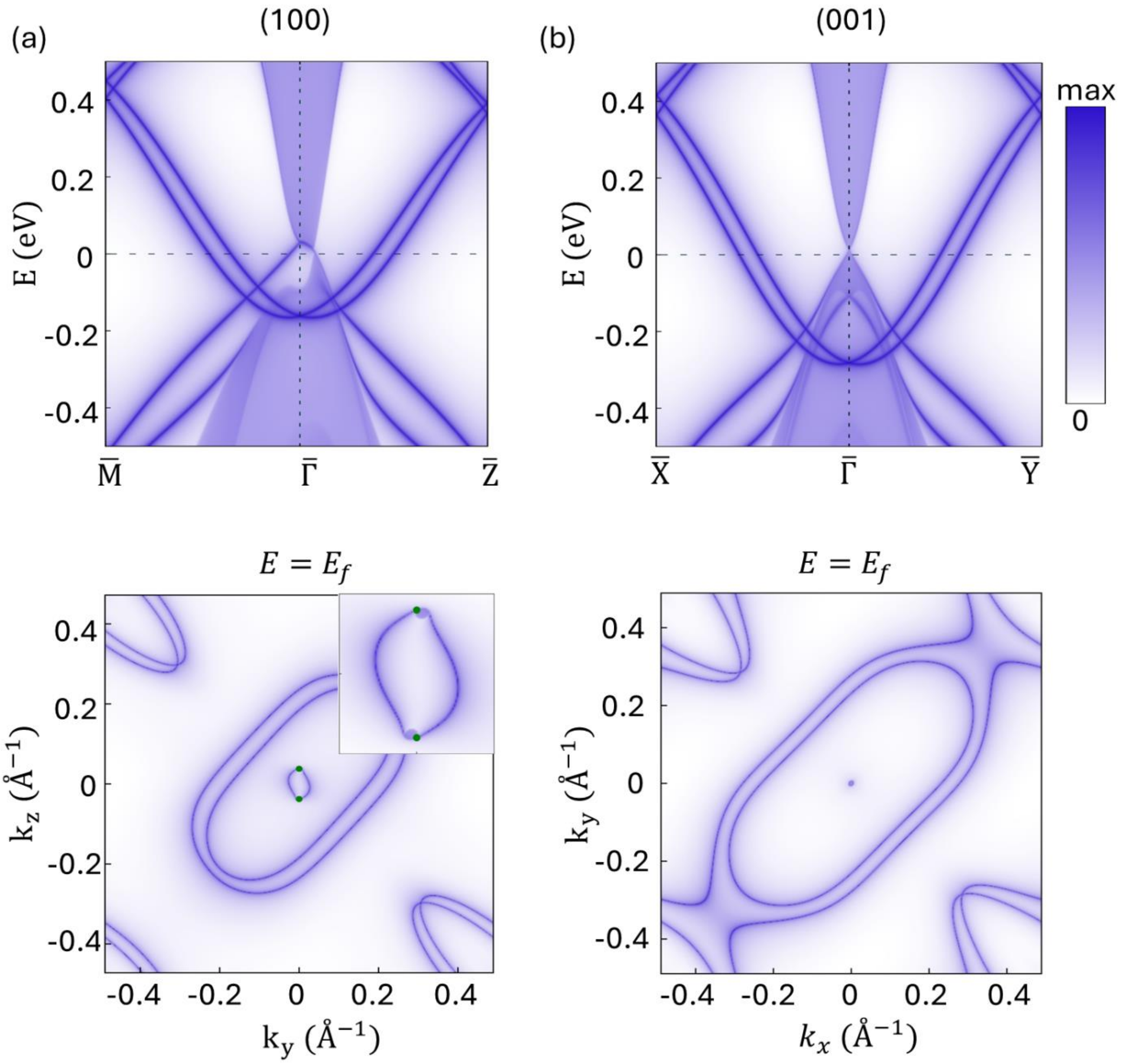

Figure S3. (Color online) The electronic band structure of the surface is projected on (a) (100) along $\overline{\mathrm{M}}\rightarrow\overline{\Gamma}\rightarrow\overline{\mathrm{Z}}$ and (b) (001) along $\overline{\mathrm{X}}\rightarrow\overline{\Gamma}\rightarrow\overline{\mathrm{Y}}$. The isoenergic Fermi-surface contour is displayed in the bottom panel, Dirac points are located with green circle.

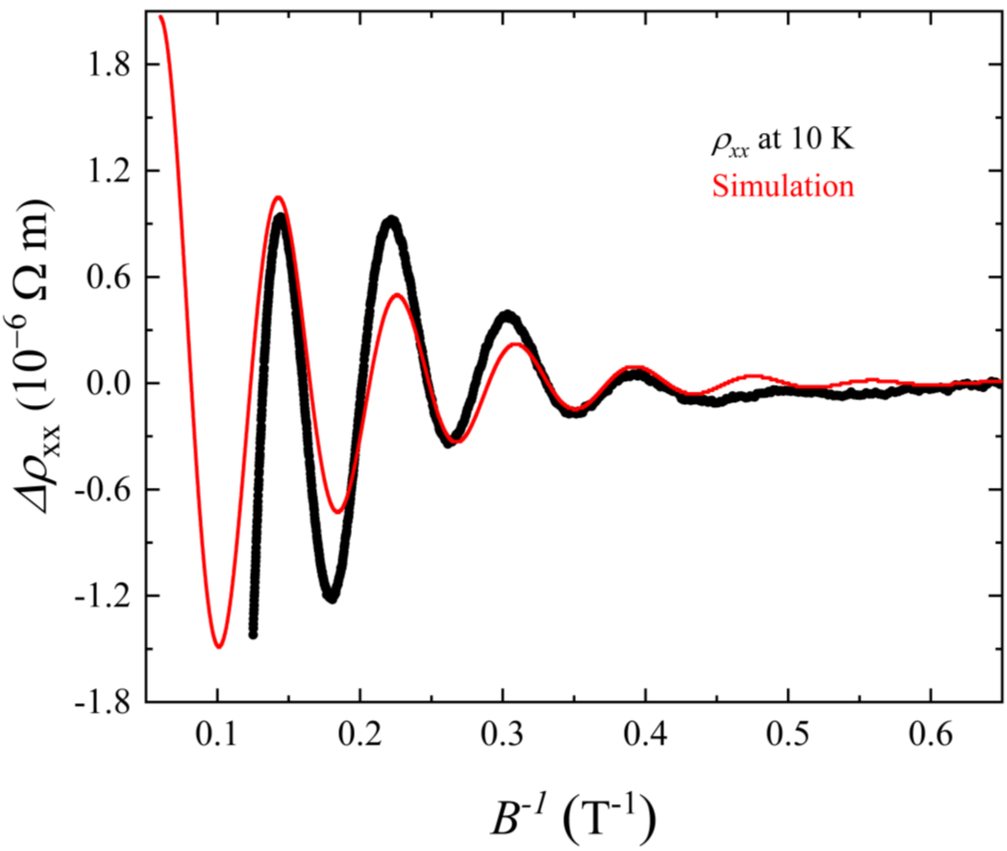

Figure S4 . (Color online) (a) Quantum oscillations after subtracting the smooth 3rd order polynomial background in the field range of 1.5 to 8 T from ρ_{xx}(B) at 10 K temperature. Solid Red line presents the simulation of $\Delta\rho_{xx}$ vs B^{-1} using the Lifshitz-Kosevich formula in the field range of 1.5 to 14.5 T. The parameters were used for the simulation are frequency f_{SdH} ~ 12 T, effective mass $m^* \approx 0.01\ m_e$, Dingle temperature T_D = 11 K, and additional phase shift $\beta \pm \delta = 0.7$. These parameters have been extracted from the fitting procedure described in the main text.

CHAPTER 4

CONCLUSIONS

In summary, I have studied the transport phenomenon of topological semimetals using electrical and thermoelectric transport measurements. Specifically, I explored quantum oscillations in $TaAs_2$, anomalous Hall and Nernst effects in CeAlSi and the chiral anomaly in α-Sn. My studies concerned anomalous thermoelectrical transport phenomena in these semimetals, with objective to discover fundamental aspects of their electronic structures. The reported results, however, can also contribute to the search for new materials, which can be used in advanced technologies.

For $TaAs_2$, we investigated the Nernst and Shubnikov - de Hass oscillations in a magnetic field applied along the [-201] direction. At low temperatures, we detected in the Nernst signal two fundamental frequencies $f_{\nu\alpha}$ ~ 105 T and $f_{\nu\beta}$ ~ 221 T and the second harmonic of β frequency i.e. $2f_{\nu\beta}$ ~ 442 T. The temperature dependences of their amplitudes was found to be unusual. We revealed that around $T \approx 25$ K, the fundamental β oscillation is suppressed, while its second harmonic 2β reaches its peak amplitude. We recognized this behavior as the temperature driven spin-zero effect. The temperature dependent g-factor can be an origin of this phenomenon and we noticed that our estimated Landé g-factor at $T = 25$ K is considerably different from the value found at $T = 5.4$ K. This may be associated with the non-parabolic band energy dispersion or temperature evolution of the spin-orbit coupling. It is worth noting that the possibility of changes in spin-orbit coupling is particularly intriguing in the case of $TaAs_2$, where it may affect the topological attributes of the material. This appears to be an interesting topic for future research.

For CeAlSi. we performed the measurements of the anomalous Hall effect for two orientation of magnetic field, namely $B \parallel c$ (hard axis) and $B \parallel a$ (easy axis), where a and c represent crystallographic axes. We have also measured the complementary Nernst effect for $B \parallel c$ axis and all results indicated the anomalous transport properties of this recently proposed ferromagnetic Weyl semimetal. Below Curie temperature ($T < T_C$), the anomalous Hall conductivity signal showed a positive sign ($\sigma_{xy}^{A} > 0$) for $B \parallel c$ axis and a negative sign ($\sigma_{yz}^{A} < 0$) for $B \parallel a$ axis. The sign change of AHC in the ferromagnetic regime agrees well with the theoretical DFT results and has been ascribed to the reconstruction of nontrivial electronic structure of CeAlSi induced by the spins reorientation. In this temperature range, we also detected a sizeable anomalous Nernst conductivity when magnetic field was applied $B \parallel c$ axis. Noticeably, the anomalous contributions are also evident in the paramagnetic phase, where σ_{xy}^{A} initially increases and peaks at $T \approx 170$ K and then decreases, whereas σ_{yz}^{A} successively decreases with increasing temperature. Additionally, the anomalous Nernst conductivity α_{xy}^{A}/T also significantly decreases above T_C. The temperature evolution of σ_{xy}^{A} and α_{xy}^{A}/T are well described by a single band toy model, in which we assume a finite Berry curvature at the Fermi level with Weyl nodes 20 meV apart. We indicated that the topology of Weyl fermionic excitations near the Fermi level plays a key role to determining the anomalous Hall and anomalous Nernst effect in CeAlSi.

Very recently, we have also studied a strained thin film of topological Dirac semimetal α-Sn, in which we performed the electrical resistivity and thermopower measurements. The results were shown to strongly depend on the directional configuration of magnetic field with respect to the electric field or thermal gradient. For the parallel orientations, we observed negative magnetoresistance and negative slope of the thermopower which can be related to the presence of an anomalous chiral current. The experimental observations are consistent with the theoretical predictions provided by DFT calculations. The observed negative magnetoresistance and negative slope of the thermopower exhibit quadratic field dependences indicating a chiral charge pumping that disappears at high temperatures. The detection of chiral current was further confirmed by angle dependent measurements of resistivity and thermopower. Namely, we observed that the negative magnetoresistance and the negative slope of the thermopower disappeared when the magnetic field was tilted away from the direction of the electric current or the thermal gradient, suggesting the restoration of unbalanced chiral neutrality. The calculated ratio of the inter-Weyl node scattering time to Drude scattering time was shown to be, as expected, greater than one at low temperatures.

BIBLIOGRAPHY

[1] L. D. Landau, *On the Theory of Phase Transitions Part I*, Zh. Eksp. Teor. Fiz. 11:19 (1937).

[2] L. D. Landau, *On the Theory of Phase Transitions Part II*, Eksp. Teor. Fiz. 11:627 (1937).

[3] M. K. D. J. Thouless and and M. den N. M. P. Nightingale, *Quantized Hall Conductance in a Two Dimensional Periodic Potential*, Phys. Rev. Lett. **49**, 405 (1982).

[4] X. G. Wen, *Topological Orders and Edge Excitations in Fractional Quantum Hall States*, Adv. Phys. **44**, 405 (1995).

[5] M. V. Berry, *Quantal Phase Factors Accompanying Adiabatic Changes*, Proc. R. Soc. Lond. A **392**, 45 (1984).

[6] C. L. Kane and E. J. Mele, *Quantum Spin Hall Effect in Graphene*, Phys. Rev. Lett. **95**, 226801 (2005).

[7] D. Hsieh, D. Qian, L. Wray, Y. Xia, Y. S. Hor, R. J. Cava, and M. Z. Hasan, *A Topological Dirac Insulator in a Quantum Spin Hall Phase*, Nature **452**, 970 (2008).

[8] J. E. Moore, *The Birth of Topological Insulators*, Nature **464**, 194 (2010).

[9] S. Y. Xu, C. Liu, N. Alidoust, M. Neupane, D. Qian, I. Belopolski, J. D. Denlinger, Y. J. Wang, H. Lin, L. A. Wray, G. Landolt, B. Slomski, J. H. Dil, A. Marcinkova, E. Morosan, Q. Gibson, R. Sankar, F. C. Chou, R. J. Cava, A. Bansil, and M. Z. Hasan, *Observation of a Topological Crystalline Insulator Phase and Topological Phase Transition in* $Pb_{1-x}Sn_xTe$, Nat. Commun. **3**, 1192 (2012).

[10] X. Wan, A. M. Turner, A. Vishwanath, and S. Y. Savrasov, *Topological Semimetal and Fermi-Arc Surface States in the Electronic Structure of Pyrochlore Iridates*, Phys. Rev. B **83**, 205101 (2011).

[11] A. Burkov, *Topological Semimetals*, Nat. Mater. **15**, 1145 (2016).

[12] N. P. Armitage, E. J. Mele, and A. Vishwanath, *Weyl and Dirac Semimetals in Three-Dimensional Solids*, Rev. Mod. Phys. **90**, 015001 (2018).

[13] C. K. Chiu, J. C. Y. Teo, A. P. Schnyder, and S. Ryu, *Classification of Topological Quantum Matter with Symmetries*, Rev. Mod. Phys. **88**, 035005 (2016).

[14] G. E. VOLOVIK, *The Universe in a Helium Droplet Oxford: Clarendon Press* (2003).

[15] Z. Wang, Y. Sun, X. Q. Chen, C. Franchini, G. Xu, H. Weng, X. Dai, and Z. Fang, *Dirac Semimetal and Topological Phase Transitions in* A_3Bi *(A=Na, K, Rb)*, Phys. Rev. B **85**, 195320 (2012).

[16] F. D. M. Haldane, *Berry Curvature on the Fermi Surface: Anomalous Hall Effect as a Topological Fermi-Liquid Property*, Phys. Rev. Lett. **93**, 206602 (2004).

[17] H. Liu, J. Liang, T. Sun, and L. Wang, *Recent Progress in Topological Semimetal and Its Realization in Heusler Compounds*, Mater. Today Phys. **41**, 101343 (2024).

[18] Q. F. Liang, J. Zhou, R. Yu, Z. Wang, and H. Weng, *Node-Surface and Node-Line Fermions from Nonsymmorphic Lattice Symmetries*, Phys. Rev. B **93**, 085427 (2016).

[19] C. Herring, *Accidental Degeneracy in the Energy Bands of Crystals*, Phys. Rev. **52**, 365 (1937).

[20] S. Y. Xu, Y. Xia, L. A. Wray, S. Jia, F. Meier, J. H. Dil, J. Osterwalder, B. Slomski, A. Bansil, H. Lin, R. J. Cava, and M. Z. Hasan, *Topological Phase Transition and Texture Inversion in a Tunable Topological Insulator*, Science. **332**, 560 (2011).

[21] P. P. Ferreira, A. L. R. Manesco, T. T. Dorini, L. E. Correa, G. Weber, A. J. S. Machado, and L. T. F. Eleno, *Strain Engineering the Topological Type-II Dirac Semimetal* $NiTe_2$, Phys. Rev. B **103**, 125134 (2021).

[22] M. Brahlek, N. Bansal, N. Koirala, S. Y. Xu, M. Neupane, C. Liu, M. Z. Hasan, and S. Oh, *Topological-Metal to Band-Insulator Transition in* $(Bi_{1-x}In_x)_2Se_3$ *Thin Films*, Phys. Rev. Lett. **109**, 186403 (2012).

[23] Q. Li, D. E. Kharzeev, C. Zhang, Y. Huang, I. Pletikosić, A. V. Fedorov, R. D. Zhong, J. A. Schneeloch, G. D. Gu, and T. Valla, *Chiral Magnetic Effect in* $ZrTe_5$, Nat. Phys. **12**, 550 (2016).

[24] S. M. Young, S. Zaheer, J. C. Y. Teo, C. L. Kane, E. J. Mele, and A. M. Rappe, *Dirac Semimetal in Three Dimensions*, Phys. Rev. Lett. **108**, 140405 (2012).

[25] J. A. Steinberg, S. M. Young, S. Zaheer, C. L. Kane, E. J. Mele, and A. M. Rappe, *Bulk Dirac Points in Distorted Spinels*, Phys. Rev. Lett. **112**, 036403 (2014).

[26] M. Neupane, S. Y. Xu, R. Sankar, N. Alidoust, G. Bian, C. Liu, I. Belopolski, T. R. Chang, H. T. Jeng, H. Lin, A. Bansil, F. Chou, and M. Z. Hasan, *Observation of a Three-Dimensional Topological Dirac Semimetal Phase in High-Mobility* Cd_3As_2, Nat. Commun. **5**, 3786 (2014).

[27] Z. K. Liu, B. Zhou, Y. Zhang, Z. J. Wang, H. M. Weng, D. Prabhakaran, S. Mo, Z. X. Shen, Z. Fang, X. Dai, Z. Hussain, and Y. L. Chen, *Topological Dirac Semimetal ,* Na_3Bi, Science. **343**, 864 (2014).

[28] C. Z. Xu, Y. H. Chan, Y. Chen, P. Chen, X. Wang, C. Dejoie, M. H. Wong, J. A. Hlevyack, H. Ryu, H. Y. Kee, N. Tamura, M. Y. Chou, Z. Hussain, S. K. Mo, and T. C. Chiang, *Elemental Topological Dirac Semimetal:* α *-Sn on InSb(111)*, Phys. Rev. Lett. **118**, 146402 (2017).

[29] M. S. Alam, A. Kazakov, M. Ahmad, R. Islam, F. Xue, and M. Matusiak, *Quantum Transport Properties of the Topological Dirac Semimetal* α *-Sn*, ArXiv:2403.00083 (2024).

[30] A. A. Burkov, *Weyl Metals*, Annu. Rev. Condens. Matter Phys. **9**, 359 (2018).

[31] H. Weyl, *Elektron Und Gravitation. I*, Zeitschrift Für Phys. **56**, 330 (1929).

[32] B. Yan and C. Felser, *Topological Materials: Weyl Semimetals*, Annu. Rev. Condens. Matter Phys. **8**, 337 (2017).

[33] A. A. Burkov and L. Balents, *Weyl Semimetal in a Topological Insulator Multilayer*, Phys. Rev. Lett. **107**, 127205 (2011).

[34] T. Guan, C. Lin, C. Yang, Y. Shi, C. Ren, Y. Li, H. Weng, X. Dai, Z. Fang, S. Yan,

and P. Xiong, *Evidence for Half-Metallicity in n -Type $HgCr_2Se_4$*, Phys. Rev. Lett. **115**, 087002 (2015).

[35] Q. Xu, E. Liu, W. Shi, L. Muechler, J. Gayles, C. Felser, and Y. Sun, *Topological Surface Fermi Arcs in the Magnetic Weyl Semimetal $Co_3Sn_2S_2$*, Phys. Rev. B **97**, 235416 (2018).

[36] K. Manna, Y. Sun, L. Muechler, J. Kübler, and C. Felser, *Heusler, Weyl and Berry*, Nat. Rev. Mater. **3**, 244 (2018).

[37] M. Ikhlas, T. Tomita, T. Koretsune, M. T. Suzuki, D. Nishio-Hamane, R. Arita, Y. Otani, and S. Nakatsuji, *Large Anomalous Nernst Effect at Room Temperature in a Chiral Antiferromagnet*, Nat. Phys. **13**, 1085 (2017).

[38] C. Z. Li, L. X. Wang, H. Liu, J. Wang, Z. M. Liao, and D. P. Yu, *Giant Negative Magnetoresistance Induced by the Chiral Anomaly in Individual Cd_3As_2 Nanowires*, Nat. Commun. **6**, 10137 (2015).

[39] J. Xiong, S. K. Kushwaha, T. Liang, J. W. Krizan, M. Hirschberger, W. Wang, R. J. Cava, and N. P. Ong, *Evidence for the Chiral Anomaly in the Dirac Semimetal Na_3Bi*, Science. **350**, 413 (2015).

[40] B. Singh, A. Sharma, H. Lin, M. Z. Hasan, R. Prasad, and A. Bansil, *Topological Electronic Structure and Weyl Semimetal in the $TlBiSe_2$ Class of Semiconductors*, Phys. Rev. B **86**, 115208 (2012).

[41] J. Liu and D. Vanderbilt, *Weyl Semimetals from Noncentrosymmetric Topological Insulators*, Phys. Rev. B **90**, 155316 (2014).

[42] S. Y. Xu, I. Belopolski, N. Alidoust, M. Neupane, G. Bian, C. Zhang, R. Sankar, G. Chang, Z. Yuan, C. C. Lee, S. M. Huang, H. Zheng, J. Ma, D. S. Sanchez, B. K. Wang, A. Bansil, F. Chou, P. P. Shibayev, H. Lin, S. Jia, and M. Z. Hasan, *Discovery of a Weyl Fermion Semimetal and Topological Fermi Arcs*, Science. **349**, 613 (2015).

[43] S. Souma, Z. Wang, H. Kotaka, T. Sato, K. Nakayama, Y. Tanaka, H. Kimizuka, T. Takahashi, K. Yamauchi, T. Oguchi, K. Segawa, and Y. Ando, *Direct Observation of Nonequivalent Fermi-Arc States of Opposite Surfaces in the Noncentrosymmetric Weyl Semimetal NbP*, Phys. Rev. B **93**, 161112(R) (2016).

[44] S. Y. Xu, N. Alidoust, I. Belopolski, Z. Yuan, G. Bian, T. R. Chang, H. Zheng, V. N. Strocov, D. S. Sanchez, G. Chang, C. Zhang, D. Mou, Y. Wu, L. Huang, C. C. Lee, S. M. Huang, B. Wang, A. Bansil, H. T. Jeng, T. Neupert, A. Kaminski, H. Lin, S. Jia, and M. Z. Hasan, *Discovery of a Weyl Fermion State with Fermi Arcs in Niobium Arsenide*, Nat. Phys. **11**, 748 (2015).

[45] S. Y. Xu, I. Belopolski, D. S. Sanchez, C. Zhang, G. Chang, C. Guo, G. Bian, Z. Yuan, H. Lu, T. R. Chang, P. P. Shibayev, M. L. Prokopovych, N. Alidoust, H. Zheng, C. C. Lee, S. M. Huang, R. Sankar, F. Chou, C. H. Hsu, H. T. Jeng, A. Bansil, T. Neupert, V. N. Strocov, H. Lin, S. Jia, and M. Zahid Hasan, *Experimental Discovery of a Topological Weyl Semimetal State in TaP*, Sci. Adv. **1**, e1501092 (2015).

[46] J. Gaudet, H. Y. Yang, S. Baidya, B. Lu, G. Xu, Y. Zhao, J. A. Rodriguez-Rivera, C. M. Hoffmann, D. E. Graf, D. H. Torchinsky, P. Nikolić, D. Vanderbilt, F. Tafti, and C. L. Broholm, *Weyl-Mediated Helical Magnetism in NdAlSi*, Nat. Mater. **20**, 1650 (2021).

[47] B. Skinner and L. Fu, *Large, Nonsaturating Thermopower in a Quantizing Magnetic Field*, Sci. Adv. **4**, eaat2621 (2018).

[48] Y. He, J. Gayles, M. Yao, T. Helm, T. Reimann, V. N. Strocov, W. Schnelle, M. Nicklas, Y. Sun, G. H. Fecher, and C. Felser, *Large Linear Non-Saturating Magnetoresistance and High Mobility in Ferromagnetic MnBi*, Nat. Commun. **12**, 4576 (2021).

[49] D. Shoenberg, *Magnetic Oscillations in Metals, Cambridge Univ. Press* (1984).

[50] G. P. Mikitik and Y. V. Sharlai, *Manifestation of Berry's Phase in Metal Physics*, Phys. Rev. Lett. **82**, 2147 (1999).

[51] N. Nagaosa, J. Sinova, S. Onoda, A. H. MacDonald, and N. P. Ong, *Anomalous Hall Effect*, Rev. Mod. Phys. **82**, 1539 (2010).

[52] Y. Pan, C. Le, B. He, S. J. Watzman, M. Yao, J. Gooth, J. P. Heremans, Y. Sun, and C. Felser, *Giant Anomalous Nernst Signal in the Antiferromagnet $YbMnBi_2$*, Nat. Mater. **21**, 203 (2022).

[53] N. P. Ong and S. Liang, *Experimental Signatures of the Chiral Anomaly in Dirac–Weyl Semimetals,* Nat. Rev. Phys. **3**, 394 (2021).

[54] J. Hu, S. Y. Xu, N. Ni, and Z. Mao, *Transport of Topological Semimetals*, Annu. Rev. Mater. Res. **49**, 207 (2019).

[55] A. Narayanan, M. D. Watson, S. F. Blake, N. Bruyant, L. Drigo, Y. L. Chen, D. Prabhakaran, B. Yan, C. Felser, T. Kong, P. C. Canfield, and A. I. Coldea, *Linear Magnetoresistance Caused by Mobility Fluctuations in n -Doped Cd_3As_2*, Phys. Rev. Lett. **114**, 117201 (2015).

[56] J. Hu, Z. Tang, J. Liu, Y. Zhu, J. Wei, and Z. Mao, *Nearly Massless Dirac Fermions and Strong Zeeman Splitting in the Nodal-Line Semimetal ZrSiS Probed by de Haas-van Alphen Quantum Oscillations*, Phys. Rev. B **96**, 045127 (2017).

[57] M. S. Alam, P. K. Tanwar, K. Dybko, A. S. Wadge, P. Iwanowski, A. Wiśniewski, and M. Matusiak, *Temperature-Driven Spin-Zero Effect in $TaAs_2$*, J. Phys. Chem. Solids **170**, 110939 (2022).

[58] W. Zhao and X. Wang, *Berry Phase in Quantum Oscillations of Topological Materials*, Adv. Phys. X **7**, 2064230 (2022).

[59] E. H. Hall, *On a New Action of the magnet on Electric current*, Am. J. Math. **2**, 287 (1879).

[60] E. H. Hall, *XVIII. On the "Rotational Coefficient" in Nickel and Cobalt* , London, Edinburgh, Dublin Philos. Mag. J. Sci. **12**, 157 (1881).

[61] A. Sakai, S. Minami, T. Koretsune, T. Chen, T. Higo, Y. Wang, T. Nomoto, M. Hirayama, S. Miwa, D. Nishio-Hamane, F. Ishii, R. Arita, and S. Nakatsuji, *Iron-Based Binary Ferromagnets for Transverse Thermoelectric Conversion*, Nature **581**, 53 (2020).

[62] A. A. Burkov, *Anomalous Hall Effect in Weyl Metals*, Phys. Rev. Lett. **113**, 187202 (2014).

[63] S. N. Guin, K. Manna, J. Noky, S. J. Watzman, C. Fu, N. Kumar, W. Schnelle, C.

Shekhar, Y. Sun, J. Gooth, and C. Felser, *Anomalous Nernst Effect beyond the Magnetization Scaling Relation in the Ferromagnetic Heusler Compound Co_2MnGa*, NPG Asia Mater. **11**, 16 (2019).

[64] S. K. Bac, K. Koller, F. Lux, J. Wang, L. Riney, K. Borisiak, W. Powers, M. Zhukovskyi, T. Orlova, M. Dobrowolska, J. K. Furdyna, N. R. Dilley, L. P. Rokhinson, Y. Mokrousov, R. J. McQueeney, O. Heinonen, X. Liu, and B. A. Assaf, *Topological Response of the Anomalous Hall Effect in $MnBi_2Te_4$ Due to Magnetic Canting*, Npj Quantum Mater. **7**, 46 (2022).

[65] R. Karplus and J. M. Luttinger, *Hall Effect in Ferromagnetics*, Phys. Rev. **95**, 1154 (1954).

[66] Q. Wang, Y. Xu, R. Lou, Z. Liu, M. Li, Y. Huang, D. Shen, H. Weng, S. Wang, and H. Lei, *Large Intrinsic Anomalous Hall Effect in Half-Metallic Ferromagnet $Co_3Sn_2S_2$ with Magnetic Weyl Fermions*, Nat. Commun. **9**, 3681 (2018).

[67] K. Kuroda, T. Tomita, M. T. Suzuki, C. Bareille, A. A. Nugroho, P. Goswami, M. Ochi, M. Ikhlas, M. Nakayama, S. Akebi, R. Noguchi, R. Ishii, N. Inami, K. Ono, H. Kumigashira, A. Varykhalov, T. Muro, T. Koretsune, R. Arita, S. Shin, T. Kondo, and S. Nakatsuji, *Evidence for Magnetic Weyl Fermions in a Correlated Metal*, Nat. Mater. **16**, 1090 (2017).

[68] H. Yang, Y. Sun, Y. Zhang, W. J. Shi, S. S. P. Parkin, and B. Yan, *Topological Weyl Semimetals in the Chiral Antiferromagnetic Materials Mn_3Ge and Mn_3Sn*, New J. Phys. **19**, 015008 (2017).

[69] J. Barth, G. H. Fecher, B. Balke, T. Graf, A. Shkabko, A. Weidenkaff, P. Klaer, M. Kallmayer, H. J. Elmers, H. Yoshikawa, S. Ueda, K. Kobayashi, and C. Felser, *Anomalous Transport Properties of the Half-Metallic Ferromagnets Co 2TiSi, Co_2TiGe and Co_2TiSn*, Philos. Trans. R. Soc. A **369**, 3588 (2011).

[70] M. S. Alam, A. Fakhredine, M. Ahmad, P. K. Tanwar, H. Y. Yang, F. Tafti, G. Cuono, R. Islam, B. Singh, A. Lynnyk, C. Autieri, and M. Matusiak, *Sign Change of Anomalous Hall Effect and Anomalous Nernst Effect in the Weyl Semimetal CeAlSi*, Phys. Rev. B **107**, 85102 (2023).

[71] J. Smit, *The Spontaneous Hall Effect in Ferromagnetics I*, Physica **21**, 877 (1955).

[72] L. Berger, *Influence of Spin-Orbit Interaction on the Transport Processes in Ferromagnetic Nickel Alloys, in the Presence of a Degeneracy of the 3d Band*, Physica **30**, 1141 (1964).

[73] R. A. Bertlmann, *Anomalies in Quantum Field Theory: Dispersion Relations and Differential Geometry*, Nucl. Phys. B (Proc. Suppl.) **39**, 482 (1995).

[74] S. L. Adler, *Axial-Vector Vertex in Spinor Electrodynamics*, Phys. Rev. **177**, 2426 (1969).

[75] H. B. Nielsen and M. Ninomiya, *The Adler-Bell-Jackiw Anomaly and Weyl Fermions in a Crystal*, Phys. Lett. B **130**, 389 (1983).

[76] D. T. Son and B. Z. Spivak, *Chiral Anomaly and Classical Negative Magnetoresistance of Weyl Metals*, Phys. Rev. B **88**, 104412 (2013).

[77] K. Yoshida, *A Geometrical Transport Model for Inhomogeneous Current Distribution*

in Semimetals under High Magnetic Fields, J. Phys. Soc. Jpn **40**, 1027 (1976).

[78] M. C. Chang and M. F. Yang, *Chiral Magnetic Effect in the Absence of Weyl Node*, Phys. Rev. B **92**, 205201 (2015).

[79] C. Felser and J. Gooth, *Topology and Chirality*, ArXiv:2205.05809 (2023).

[80] T. J. Seebeck, *"Magnetische Polarisation Der Metalle Und Erze Durch Temperatur-Differenz" (Magnetic Polarization of Metals and Minerals by Temperature Differences), Abhandlungen Der Königlichen Akademie Der Wissenschaften Zu Berlin*, Treatises R. Acad. Sci. Berlin pp. 265 (2003).

[81] H. B. Callen, *The Application of Onsager's Reciprocal Relations to Thermoelectric, Thermomagnetic, and Galvanomagnetic Effects*, Phys. Rev. **73**, 1349 (1948).

[82] Kamran. Behnia, *Fundamentals of Thermoelectricity,* Oxford University Press, Oxford, UK (2015).

[83] T. Liang, Q. Gibson, J. Xiong, M. Hirschberger, S. P. Koduvayur, R. J. Cava, and N. P. Ong, *Evidence for Massive Bulk Dirac Fermions in* $Pb_{1-X}Sn_XSe$ *from Nernst and Thermopower Experiments*, Nat. Commun. **4**, 2696 (2013).

[84] K. Behnia and H. Aubin, *Nernst Effect in Metals and Superconductors: A Review of Concepts and Experiments*, Reports Prog. Phys. **79**, 046502 (2016).

[85] E. H. Sondheimer, *The Theory of the Galvanomagnetic and Thermomagnetic Effects in Metals*, Proc. R. Soc. London. Ser. A. Math. Phys. Sci. **193**, 484 (1948).

[86] N. F. Mott and H. Jones, *The Theory of the Properties of Metals and Alloys,* Oxford University Press, Oxford (1936).

[87] N. W. Ashcroft and N. D. Mermin, *Solid State Physics*, Holt, Rinehart and Winston (1976).

[88] C. L. F. and D. G. Frank J. Blatt, Peter A. Schroeder, *THERMOELECTRIC POWER OF METALS*, Plenum Press, New York (1976).

[89] V. Kozii, B. Skinner, and L. Fu, *Thermoelectric Hall Conductivity and Figure of Merit in Dirac/Weyl Materials*, Phys. Rev. B **99**, 155123 (2019).

[90] X. Xu, Y. Liu, G. Seyfarth, A. Pourret, W. Ma, H. Zhou, G. Wang, Z. Qu, and S. Jia, *Thermoelectric Transport and Phonon Drag in Weyl Semimetal Monochalcogenides*, Phys. Rev. B **104**, 115164 (2021).

[91] M. Matusiak, J. R. Cooper, and D. Kaczorowski, *Thermoelectric Quantum Oscillations in ZrSiS*, Nat. Commun. **8**, 15219 (2017).

[92] Z. Jia, C. Li, X. Li, J. Shi, Z. Liao, D. Yu, and X. Wu, *Thermoelectric Signature of the Chiral Anomaly in* Cd_3As_2, Nat. Commun. **7**, 13013 (2016).

[93] J. Noky, J. Gooth, C. Felser, and Y. Sun, *Characterization of Topological Band Structures Away from the Fermi Level by the Anomalous Nernst Effect*, Phys. Rev. B **98**, 241106(R) (2018).

[94] D. Gresch, Q. Wu, G. W. Winkler, and A. A. Soluyanov, *Hidden Weyl Points in Centrosymmetric Paramagnetic Metals*, New J. Phys. **19**, 035001 (2017).

[95] S. Sun, Z. Song, H. Weng, and X. Dai, *Topological Metals Induced by the Zeeman*

Effect, Phys. Rev. B **101**, 125118 (2020).

[96] H. Y. Yang, B. Singh, J. Gaudet, B. Lu, C. Y. Huang, W. C. Chiu, S. M. Huang, B. Wang, F. Bahrami, B. Xu, J. Franklin, I. Sochnikov, D. E. Graf, G. Xu, Y. Zhao, C. M. Hoffman, H. Lin, D. H. Torchinsky, C. L. Broholm, A. Bansil, and F. Tafti, *Noncollinear Ferromagnetic Weyl Semimetal with Anisotropic Anomalous Hall Effect*, Phys. Rev. B **103**, 115143 (2021).

[97] J. Polaczyński, G. Krizman, A. Kazakov, B. Turowski, J. B. Ortiz, R. Rudniewski, T. Wojciechowski, P. Dłużewski, M. Aleszkiewicz, W. Zaleszczyk, B. Kurowska, Z. Muhammad, M. Rosmus, N. Olszowska, L.-A. De Vaulchier, Y. Guldner, T. Wojtowicz, and V. V. Volobuev, *3D Topological Semimetal Phases of Strained α-Sn on Insulating Substrate*, ArXiv:2309.03951 (2023).

[98] M. S. and P. S. Michael Binnewies , Robert Glaum, *Chemical Vapor Transport Reactions,* De G., Berlin, Boston, (2012).

[99] A. W. Ashutosh S Wadge, Grzegorz Grabecki, Carmine Autieri, Bogdan J Kowalski, Przemysław Iwanowski, Giuseppe Cuono, MF Islam, Carlo M Canali, Krzysztof Dybko, Andrzej Hruban, Andrzej Łusakowski, Tomasz Wojciechowski, Ryszard Diduszko, Artem Lynnyk, Natalia Ols, *Electronic Properties of $TaAs_2$ Topological Semimetal Investigated by Transport and ARPES,* J. Phys. Condens. Matter **34**, 125601 (2022).

[100] G. Lehmpfuhl, A. Ichimiya, and H. Nakahara, *Interpretation of RHEED Oscillations during MBE Growth*, Surf. Sci. Lett. **245**, L159 (1991).

[101] A. Chambers, *Creating a Vacuum* - Pumps, Chapman & Hall (CRC) (2005).

[102] S. M. N. and P. S. R. A. Kubiak, *Molecular Beam Epitaxy*, William Andrew Publishing, *1-113* (1995).

[103] B. Wang, B. Singh, B. Ghosh, W. C. Chiu, M. M. Hosen, Q. Zhang, L. Ying, M. Neupane, A. Agarwal, H. Lin, and A. Bansil, *Topological Crystalline Insulator State with Type-II Dirac Fermions in Transition Metal Dipnictides,* Phys. Rev. B **100**, 205118 (2019).

[104] Y. Luo, R. D. McDonald, P. F. S. Rosa, B. Scott, N. Wakeham, N. J. Ghimire, E. D. Bauer, J. D. Thompson, and F. Ronning, *Anomalous Electronic Structure and Magnetoresistance in $TaAs_2$*, Sci. Rep. **6**, 27294 (2016).

[105] Y. Y. Wang, Q. H. Yu, P. J. Guo, K. Liu, and T. L. Xia, *Resistivity Plateau and Extremely Large Magnetoresistance in NbAs2 and TaAs2*, Phys. Rev. B **94**, 041103(R) (2016).

[106] H. Y. Yang, B. Singh, B. Lu, C. Y. Huang, F. Bahrami, W. C. Chiu, D. Graf, S. M. Huang, B. Wang, H. Lin, D. Torchinsky, A. Bansil, and F. Tafti, *Transition from Intrinsic to Extrinsic Anomalous Hall Effect in the Ferromagnetic Weyl Semimetal $PrAlGe_{1-X}Si_x$*, APL Mater. **8**, 011111 (2020).

[107] G. Chang, B. Singh, S. Y. Xu, G. Bian, S. M. Huang, C. H. Hsu, I. Belopolski, N. Alidoust, D. S. Sanchez, H. Zheng, H. Lu, X. Zhang, Y. Bian, T. R. Chang, H. T. Jeng, A. Bansil, H. Hsu, S. Jia, T. Neupert, H. Lin, and M. Z. Hasan, *Magnetic and Noncentrosymmetric Weyl Fermion Semimetals in the RAlGe Family of Compounds (R= Rare Earth)*, Phys. Rev. B **97**, 041104(R) (2018).